Physical and Biological Controls on Ocean Acidification in the Southampton Island Region, Hudson Bay

by

Yekaterina Yezhova

A thesis submitted to the Faculty of Graduate Studies of
the University of Manitoba
in partial fulfillment of the requirements of the degree of

MASTER OF SCIENCE

Department of Environment and Geography
University of Manitoba
Winnipeg

Abstract

Located in northwestern Hudson Bay, the Southampton Island region was identified as an Ecologically and Biologically Significant Area by Fisheries and Oceans Canada, and most recently distinguished as an Area of Interest in 2019 to become a Marine Protected Area. The region is undergoing climate-related changes; however, its oceanography has received little attention until recently. The main goal of this thesis was to provide a baseline evaluation of the state of ocean acidification of these waters, and to identify key factors driving changes in both pH and calcium carbonate saturation state. Twenty-two stations were sampled around the Island in August of 2019 for salinity, stable oxygen isotope ratio of seawater, total alkalinity, dissolved inorganic carbon (DIC), and stable carbon isotope ratio of DIC ($\delta^{13}C_{DIC}$), providing comprehensive water column coverage. High fractions of sea-ice melt were found in surface waters in Foxe Basin/Channel, which had experienced the most recent loss of sea ice. High fractions of meteoric water were found in near-surface waters in Roes Welcome Sound, likely from Wager Bay outflow, and south of the Island, likely from both rivers local to the Island and from Hudson Bay's northwestern rivers. Regionally high pH, low pCO_2, dissolved oxygen (O_2) oversaturation, and enriched values of $\delta^{13}C_{DIC}$, and thus likely areas of net primary production, were generally observed in the top ~50 m in Foxe Basin/Channel and Roes Welcome Sound, and near surface in Repulse Bay and Frozen Strait. More acidic and aragonite-undersaturated waters, potentially corrosive to marine calcifying organisms, were found below ~60 to 250 m at stations in Foxe Basin/Channel, and in bottom waters of South Bay and Evans Strait. These areas were high in pCO_2 and undersaturated in O_2, signifying net respiration had likely produced the observed values. It was concluded that while primary production and respiration appeared to be the dominant processes controlling the concentration of DIC in the Southampton Island region, the data could not be explained by any single process alone, highlighting the importance of metabolic processes, freshwater inputs, and air-sea gas exchange in governing the DIC pool in the region.

Acknowledgements

Foremost I would like to express my sincere gratitude to my advisor, Dr. Tim Papakyriakou, who opened the world of oceanography to me and without whom I could not have undertaken this journey. I am eternally grateful for the time Tim invested in me and my research, for his mentorship, kind words, continuous support, and opportunities to join exciting research expeditions.

I extend my gratitude to Dr. Kristina Brown and to my committee members, Drs. CJ Mundy, Zou Zou Kuzyk, and Jens Ehn, for offering their invaluable insights, feedback, and support. A special thank you to Tonya Burgers for helping me navigate data analysis and for her encouragement and mentorship.

I would also like to thank Dr. David Capelle and Michelle Kamula for their assistance in fieldwork preparation and for the training they provided me prior to the expedition; Ashley Soloway, Emmelia Stainton, and Heather Stark for their logistical support; Dr. Kumiko Azetsu-Scott, Dr. Marcos Lemes, Dr. Stephen Punshon, and Darlene Childs for sample analysis training; and my fellow graduate students, colleagues, and friends for their support.

Lastly, many thanks to the Arctic Research Foundation, Captain David McIsaac and crew of the RV *William Kennedy* who worked tirelessly to make the SIMEP expedition a success.

Dedication

To my parents, Yelena and Vassiliy, for their love and support, and to my dearest, Amie, for her companionship.

Table of Contents

List of Tables

List of Figures

List of Copyrighted Material

Chapter 1: Introduction

1.1 Context and Rationale

In the process known as ocean acidification, ocean pH is lowered over decades through the uptake of carbon dioxide (CO_2) from the atmosphere, and to a lesser extent through other chemical additions or subtractions from seawater (IPCC, 2011). Anthropogenic ocean acidification refers to the lowering of pH values over decades as a result of uptake of carbon dioxide produced by human activity (IPCC, 2011). As seawater pH lowers, so does the carbonate ion (CO_3^{2-}) concentration, in turn lowering the saturation state (Ω) for biologically important calcium carbonate ($CaCO_3$) minerals, such as calcite (*ca*) and aragonite (*ar*) (AMAP, 2013). The decrease in $\Omega_{ca,ar}$ can adversely impact the marine ecosystem through hindrance of the calcification process and magnification of the dissolution process of calcifying organisms (AMAP, 2013). Lowered seawater pH can also impact marine organisms by altering their metabolism, condition, growth rate, reproductive success and/or behavior (Gattuso and Hansson, 2011). This could lead to changes in the food web, further affecting marine organisms.

Ocean acidification is tied to the seawater carbonate system through relationships between the concentration of dissolved CO_2, pH, and Ω, discussed further in Section 2. In addition to natural and anthropogenic CO_2, carbonate chemistry and calcium concentration in seawater are affected by the presence of sea ice cover and addition of its meltwater to the water column, precipitation, biological processes of respiration and production, and river runoff in coastal areas (Azetsu-Scott et al., 2014). Modelling has predicted $CaCO_3$ undersaturation in the surface water layer will first occur in Arctic seas (Orr et al., 2005; Steinacher et al., 2009). These predictions are supported by observations suggesting that surface waters of Arctic seas are already experiencing seasonal undersaturation in Ω (Azetsu-Scott et al., 2010; Azetsu-Scott et al., 2014). A recent study found that the western Arctic basins experienced annual acidification rates of a much greater magnitude than predicted by either regional or global models and also much faster than acidification rates in other ocean basins (Qi et al., 2022). Relatively little is known about the susceptibility of Arctic seas to ocean acidification; however, it is believed that recent climate-related changes in the Arctic, such as increasing precipitation, greater river runoff, melting glaciers, and loss of summer sea ice, among others, will tend to increase the rates of acidification (AMAP, 2013; CliC/AMAP/IASC, 2016; AMAP, 2017).

This thesis work is the first assessment of the complete seawater carbon system in waters surrounding Southampton Island, Nunavut. Extending 4.1×10^4 km^2 in area, Southampton Island is the largest island in the Hudson Bay Complex (Bird, 1953). The Hudson Bay Complex, which includes Hudson Bay, James Bay, Foxe Basin, Ungava Bay, and Hudson Strait, is a continental shelf sea in the sub-Arctic/Arctic with an approximate area of 1.3×10^6 km^2 (Kuzyk and Candlish, 2019). Circulation of seawater within the Complex is dominated by seasonal ice-cover and high fluvial input along the Complex's southern coasts (Azetsu-Scott et al., 2010). Hudson Bay is large and shallow with an approximate area of 0.8×10^6 km^2 and an average depth of 125 m (maximum depth = 250 m) (Prinsenberg, 1986b; Saucier et al., 2004). Notably, Hudson and James Bays receive approximately one-third of Canada's river discharge (Déry et al., 2011). Previous studies in Hudson Bay show that regional susceptibility to ocean acidification is connected to carbon chemistry of the major rivers entering the Bay, which differs depending on the watershed's geology (Azetsu-Scott et al., 2014). Aragonite undersaturation has been reported in surface waters of southeastern Hudson Bay and in two-thirds of the Bay's bottom waters (Azetsu-Scott et al., 2014; Burt et al., 2016). Hudson Bay is also heavily affected by the seasonal sea ice growth-melt cycle, as it experiences near-complete ice cover in winter and open water in summer. As a result of this freshwater input from ice melt and river runoff, the Bay experiences strong upper surface layer stratification (Ahmed et al., 2020). Seawater enters Hudson Bay through Foxe Strait (Arctic outflow primarily of Pacific origin that passes through Fury and Hecla Strait north of Foxe Basin) and the northern portion of Hudson Strait (Arctic outflow that has passed through Baffin Bay and Davis Strait and influenced by modified Atlantic water), and exits through the southern portion of Hudson Strait, with the general circulation within Hudson Bay being cyclonic (Prinsenberg, 1986b; Ingram and Prinsenberg, 1998).

Southampton Island is located in the northwest of the Hudson Bay Complex (Figure 1) at the junction of inflowing and outflowing water masses. Controls on ocean acidification in the region are expected to be complicated due to the region receiving seawater from the Canadian Arctic Archipelago, in addition to water mass modification through rivers, sea ice cycles and mixing. To the west of the Island, there is the recurring coastal Roes Welcome Sound polynya, associated with the large Kivalliq Polynya, opened and maintained mostly by wind forcing (Barber and Massom, 2007; Bruneau et al., 2021; Babb et al., 2022), with strong currents aiding in keeping the polynya open in wintertime (Loewen et al., 2020). Sea ice formation within the polynya

rejects brine, which in turn could lead to deep-water formation to the west of the Island. Through vertical mixing and convection, polynyas can have an effect on the air-sea fluxes of gases, including CO_2.

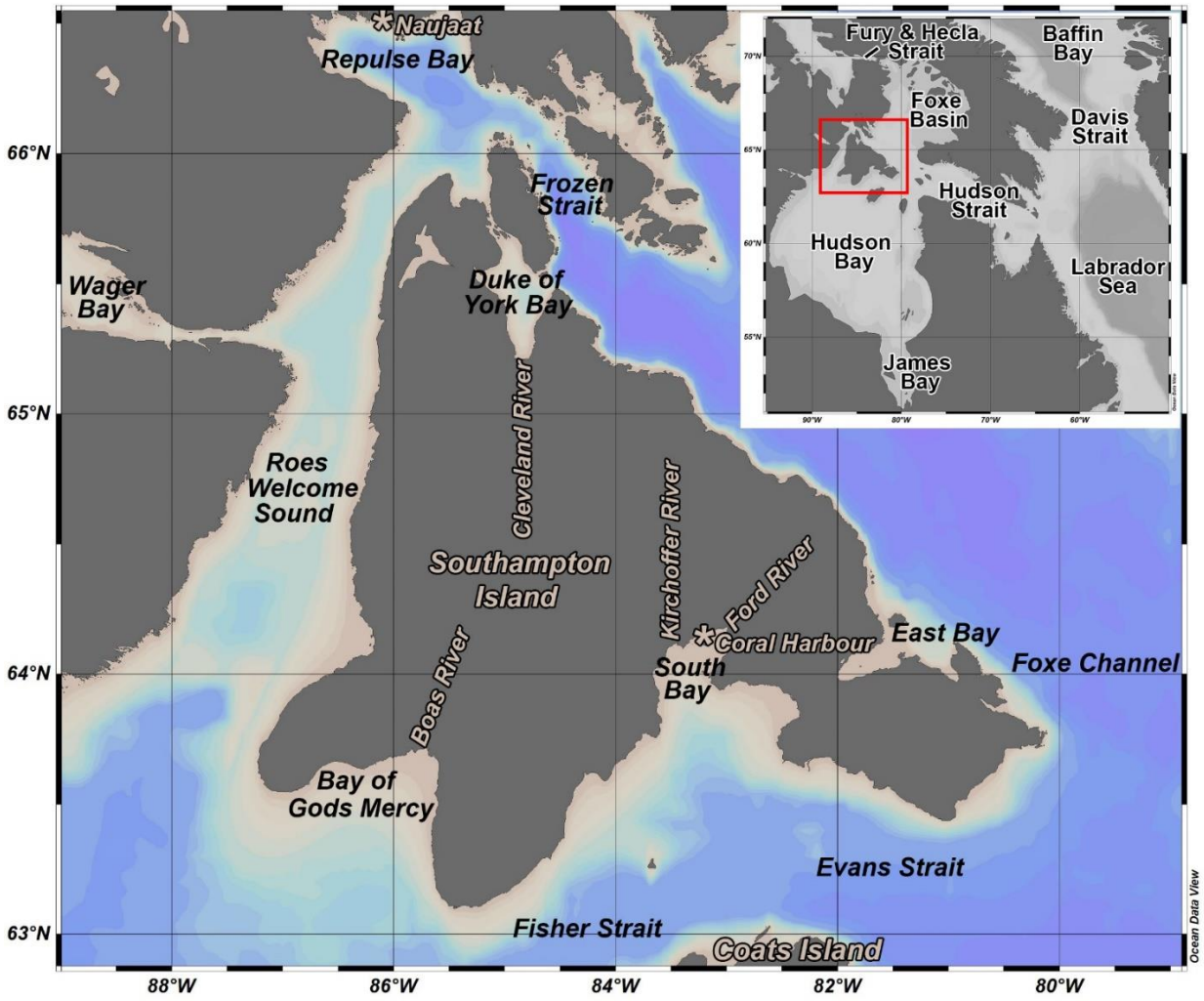

Figure 1. Map of Southampton Island, Nunavut. Communities of Coral Harbour (also known as Salliq) and Naujaat are marked with asterisks. Boas River discharging into Bay of Gods Mercy, Kirchoffer and Ford Rivers discharging into South Bay, and Cleveland River discharging into Duke of York Bay are also marked.

The area around Southampton Island is ecologically diverse with large marine mammal and seabird populations (Yurkowski et al., 2018), and the region's oceanography has received little attention until recently. In 2019, Fisheries and Oceans Canada identified most waters around the Island as an Area of Interest, with the objective to eventually make the region a Marine Protected

Area under Canada's Oceans Act (Loewen et al., 2020). The overarching objective of this thesis project was to provide a reference evaluation of the state of ocean acidification of these waters, and to identify key factors driving changes in both pH and Ω. Currently, there is no published data on the region's CO_2 system and therefore, the state and susceptibility to ocean acidification is unknown. Thus, this thesis work will constitute an important contribution toward the development of a management plan for Southampton Island.

1.2 Objectives

The main objective of this thesis is to:

- Characterize the inorganic carbon system in the Southampton Island region, Hudson Bay, to understand the state of ocean acidification and to identify main forcing variables and processes.

To achieve this objective, the following subobjectives have been formed:

- Quantify and describe the distribution of freshwater (meteoric water and sea-ice melt) within the water column and describe source seawater for the Southampton Island region.
- Perform a fine scale assessment of spatial distribution of dissolved carbon dioxide (pCO_2), and variables associated with ocean acidification, i.e., pH and Ω.
- Examine variables and processes that contribute to the observed distribution of pCO_2, pH, and Ω.
- Examine the role of biological processes on the carbonate system using information on dissolved oxygen, pCO_2, and stable carbon isotopic composition of dissolved inorganic carbon.

1.3 Thesis Structure

This thesis is comprised of six chapters. Context, rationale, and objectives of the research are provided in the first chapter. The second chapter dives deeper into the context underlying this work and gives a comprehensive literature review. Description of data collection, sample analyses, and calculations can be found in the third chapter. Chapter four outlines the results, and these results are interpreted in the fifth chapter. Lastly, conclusions of this research and recommendations for future work can be found in chapter six.

Chapter 2: Background Information

2.1 Climate and Geology of the Southampton Island Region

Located in the Arctic climate zone, the Southampton Island region experiences sub-zero temperatures majority of the time, with a range in mean daily air temperatures from -30°C in January and February to 10°C in July (Loewen et al., 2020). Similarly, precipitation typically goes through a minimum in February and a maximum in August (≥ 59 mm) (Loewen et al., 2020). From 1950-2007, Coral Harbour (Figure 1) underwent increases in mean annual air temperature and precipitation of 1.5-3°C and 10-40%, respectively (Zhang et al., 2011). The winds on the island are generally prevailing northwesterlies (Loewen et al., 2020). Geologically, Southampton Island can be divided into two regions, with Precambrian basement rock in the northeast (LaFlamme et al., 2014; Sanborn-Barrie et al., 2014) and Paleozoic carbonate rocks in the south and west of the island (Lavoie et al., 2013; Sanborn-Barrie et al., 2014). There are several sills of interest in the region: one found at 180 m depth between Southampton Island and Nottingham Island (southeast of Southampton Island), another at 70 m depth on the entry to Repulse Bay, and yet another at 50 m depth in northern Roes Welcome Sound (Defossez et al., 2008, 2010). The sill between Southampton and Nottingham Islands largely prevents deep waters of Foxe Basin and Hudson Bay from mixing.

2.2 General Circulation, Sea Ice, and Freshwater of the Southampton Island Region

As previously mentioned, Fury and Hecla Strait and northern Hudson Strait supply Arctic seawater to the Hudson Bay system, and water exits the system through southern Hudson Strait, as visualised in Figure 2 (Sadler, 1982; Jones and Anderson, 1994; Straneo and Saucier, 2008; Stewart and Howland, 2009). It is important to note that Figure 2 was made based on a high-level summary of oceanographic data available as of 2009, and updated circulation patterns for Hudson Bay have since been proposed (e.g., Figure 3). Hudson Strait experiences a net volume flux of 0.17 Sv (1 Sv = 10^6 m^3 s^{-1}) in the direction of Labrador Sea; however, when looking only at the sea ice transport and fresher Arctic waters, there is a 10.25 Sv net freshwater flux in the direction of the north Atlantic (McGeehan and Maslowski, 2012).

The current flowing from the Canadian Arctic Archipelago towards Southampton Island through Fury and Hecla Strait and western Foxe Basin has been found to stay within 50 km from the Melville Peninsula's eastern coast and reach a maximum flow of 0.6 m s^{-1} (Prinsenberg 1986a; Saucier et al. 2004). This current splits at the northern coast of Southampton Island into two: a

larger, southeastward flowing current and a smaller current that travels northwest through Frozen Strait then southwards towards Roes Welcome Sound and eventually enters northwestern Hudson Bay (Prinsenberg, 1986a; Tan and Strain, 1996; Saucier et al., 2004; Stewart and Lockhart, 2005). The smaller current flows at up to 0.35 m s^{-1} and a portion of it curves around the island at the south side, as seen in Figure 2 (Prinsenberg, 1986a; Saucier et al., 2004; Stewart and Howland, 2009; Stewart and Barber, 2010). The larger current flowing through Foxe Channel, close to Southampton Island's northeast coast, is strong, deep, and broad, and it splits at the ridge between Southampton and Nottingham Islands with the deep portion heading to southern shore of Hudson Strait (Campbell, 1959).

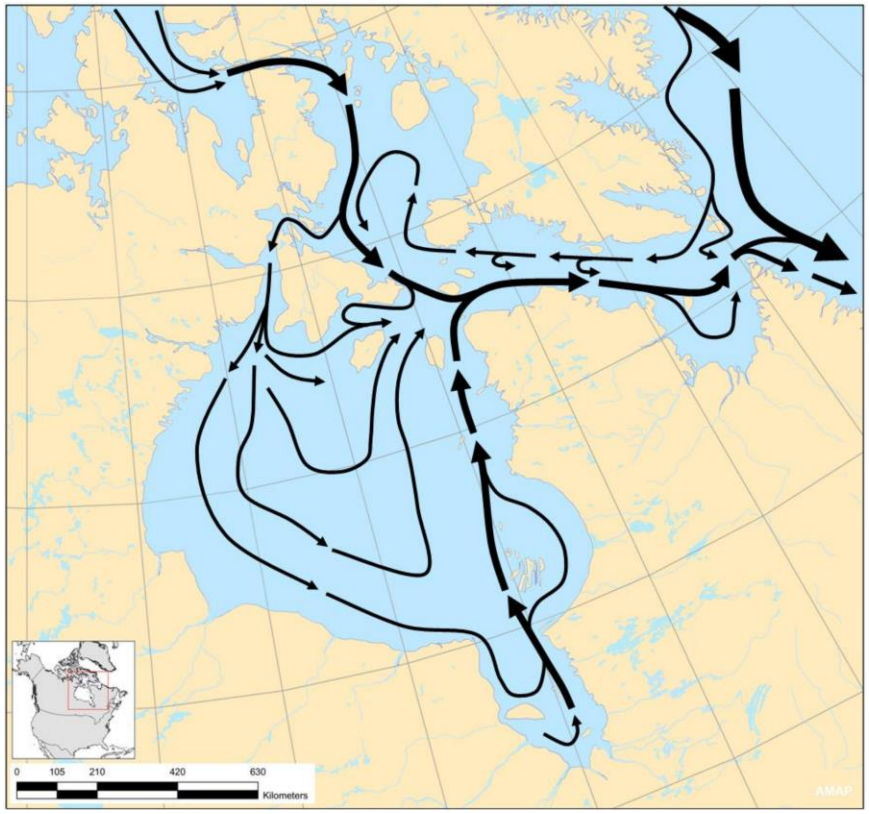

Figure 2. Summer seawater circulation within the Hudson Bay Complex. Figure from Stewart and Howland (2009). © 2009 Her Majesty the Queen in Right of Canada.

An updated circulation pattern was proposed from satellite altimetry data and modelling by Ridenour et al. (2019), with surface currents moving cyclonically from Roes Welcome Sound down to Churchill River estuary before returning to northwest Hudson Bay to pass between

Southampton and Coats Islands, as seen in the spring and summer panel in Figure 3. A portion of the southward moving current proceeds further south from Churchill River estuary to Nelson and Hayes Rivers estuary before circling back to join the flow from Churchill River estuary to Fisher Strait, as seen in the spring and summer panel in Figure 3. Current speeds in the Hudson Bay complex are shown in Figure 4.

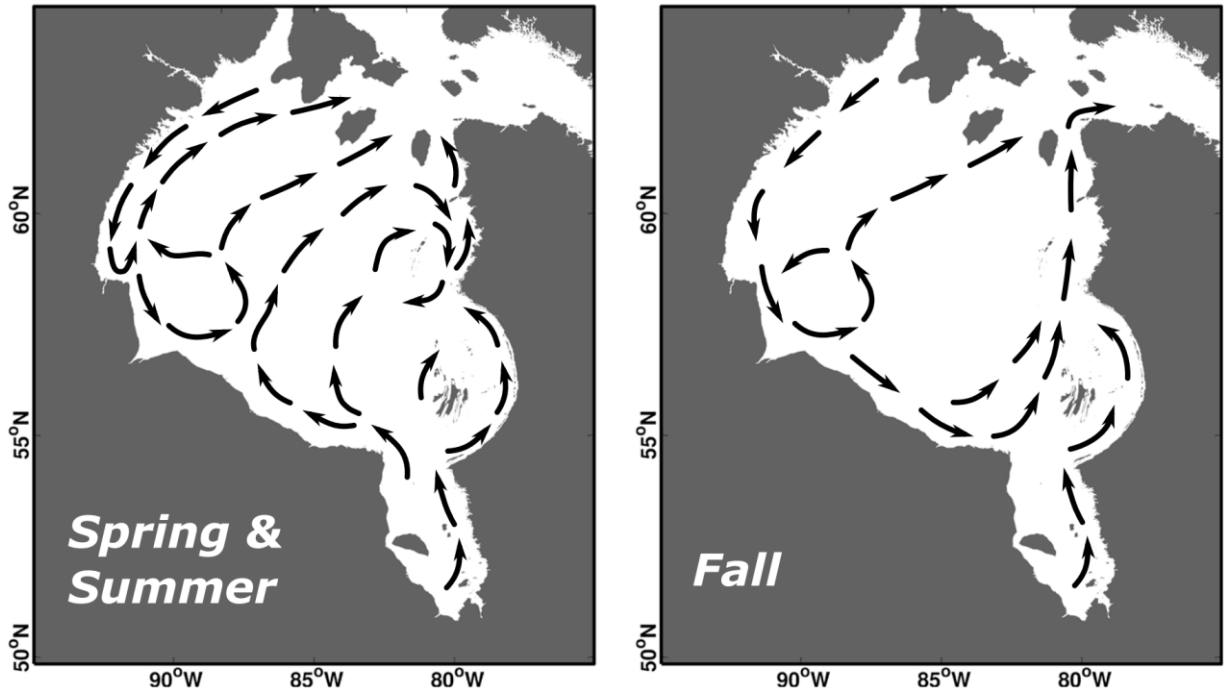

Figure 3. Average surface circulation patters in Hudson Bay. Figure from Ridenour et al. (2019). © 2019 American Geophysical Union.

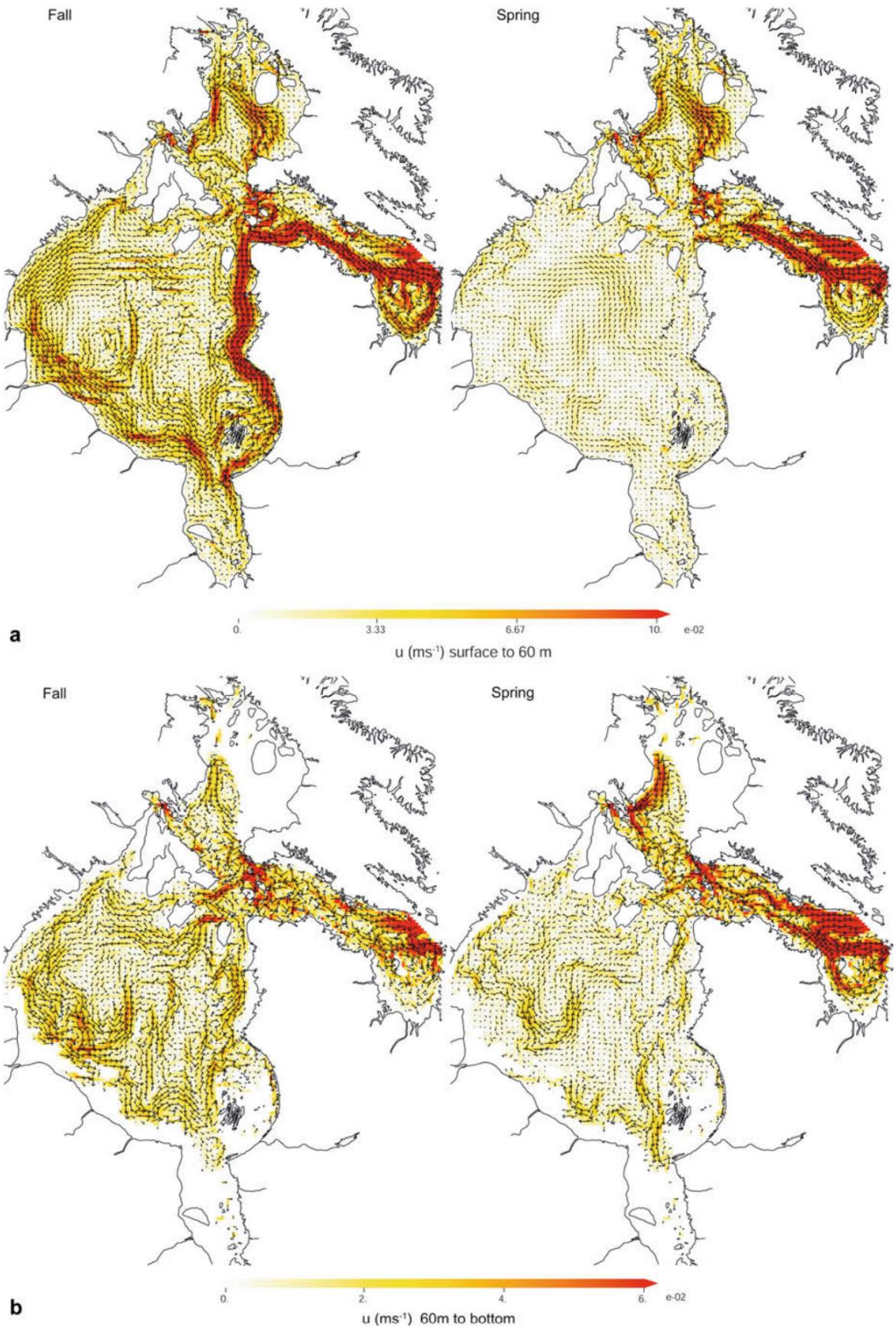

Figure 4. Horizontal currents within the Hudson Bay Complex, vertically averaged for fall and spring. Figure from Saucier et al. (2004). © 2004 Springer-Verlag.

Another feature of circulation in the Southampton Island region is the annual dense water pulse originating in Foxe Basin. Studies by Defossez et al. (2008, 2010) have shown that three coastal latent heat polynyas in western Foxe Basin (at Hall Beach, along Melville Peninsula, and at Lyon Inlet) produce a cold and saline water current that replaces roughly two-thirds of Foxe Basin's deep waters. Ice production and the consequent brine rejection within polynyas at Hall Beach and along Melville Peninsula produce dense waters that flow first southward, then southwestward along the coast until they descend into Foxe Channel, where the dense waters can merge with brine-rich waters coming from the Lyon Inlet polynya (Defossez et al., 2008). These dense waters are observed arriving in Foxe Channel in a pulse-like fashion, with the event lasting about three months following the mid-winter opening of the polynyas (Defossez et al., 2008). It has also been found that the production of new dense water, and therefore the deep water renewal in Foxe Basin/Channel, is strongly dependent on winter atmospheric conditions, e.g., mean winter temperature and wind speeds in the region (Defossez et al., 2008, 2010). However, the pulse of dense water was recorded even during a warmer winter, signifying that the phenomenon is or was an annual occurrence (Defossez et al., 2008). In fact, the pulse of cold and saline waters from the western Foxe Basin polynyas is the principal current component within Foxe Basin in wintertime (Defossez et al., 2010). It has also been shown that the dense water current has a maximal thickness of 140 m, and around summertime, when it finally reaches the sill found at 180 m depth between Southampton and Nottingham Islands, the current may still have enough kinetic energy to overflow the sill, thus transporting some deep waters from Foxe Basin into northern Hudson Bay (Defossez et al., 2008, 2010). This is consistent with findings of Saucier et al. (2004), who also projected that it might be possible for some dense water to overflow this sill between Foxe Basin and Hudson Bay.

Within the Southampton Island region, the main source of locally added freshwater (i.e., not counting the freshwater component carried by the source seawater) is the sea-ice meltwater (Jones and Anderson, 1994; Stewart and Barber, 2010). Within the Hudson Bay Complex, northern Foxe Basin sees the greatest sea ice thickness at 175-215 cm, whereas James Bay has ice of 100-125 cm thickness (Markham, 1981; Prinsenberg, 1986a; Gagnon and Gough, 2006). Around Southampton Island, southern Foxe Basin to the northeast of the Island, Frozen Strait immediately north of the Island, and Roes Welcome Sound along its western side see maximum ice thickness of 175-200 cm, whereas the waters along the Island's south side (Foxe Channel,

Evans and Fisher Straits, Bay of Gods Mercy) see maximum ice thickness of 150-175 cm (Markham, 1981). A more recent study using altimeter systems reported mean spring ice thickness from 2003-2016 to be 1.99 m for Foxe Basin, 1.35 m for the area around Southampton Island, 1.17 m for northwestern Hudson Bay, 1.34 m for central Hudson Bay, 1.54 m for eastern Hudson Bay, and 1.55 m for James Bay (Landy et al., 2017). Multiyear ice is not considered to contribute to the ice cover around the Island, with ice around the Island being described as thick first-year ice (CIS, 2016; Loewen et al., 2020).

Southampton Island region contains low volumes of river runoff, with discharge being low year-round (Loewen et al., 2020). Runoff is minimal at the northern coast of Southampton Island, with only a few streams discharging there (Stewart and Lockhart, 2005). Southampton Island rivers are marked in Figure 1. Duke of York Bay receives freshwater from the Cleveland River (Zhang, 2011). On the other side of the Island, Bay of Gods Mercy receives runoff from the Boas River, which is the longest and widest river found on the Island (Zhang, 2011). The Ford River discharges into South Bay, and so does the Kirchoffer River. The latter is the only river for which historical discharge data are available. The Kirchoffer River flow peaks at >490 $m^3 s^{-1}$ around late June/early July and reaches a minimum of little to no flow between October and May, giving a mean annual discharge rate of about 26.0 $m^3 s^{-1}$ (Loewen et al., 2020). Mean monthly flow rates of Kirchoffer River in August ranged from 12.2 – 71.8 $m^3 s^{-1}$ (ECCC, 2022), as seen in Table 1 below. This flow rate is low compared to discharges of other freshwater sources to northwestern Hudson Bay; for example, the discharge of Chesterfield Inlet is estimated to be 2387 $m^3 s^{-1}$ in August (Budgell, 1976).

Table 1. Mean, minimum, and maximum discharges of Kirchoffer River and Chesterfield Inlet in August.

	Year	**Month**	**Mean (m^3/sec)**	**Min. (m^3/sec)**	**Max. (m^3/sec)**	**Source**
Kirchoffer River	1985	8	71.8	8.71	276	ECCC, 2022
	1988	8	33.5	14.4	64.2	
	1989	8	12.2	6.18	27.5	
	1990	8	46.8	20.4	120	
	1991	8	27	16.4	52	
Chesterfield Inlet	NA	8	~2387	NA	NA	Budgell, 1976

Another source of freshwater to the Southampton Island region is Wager Bay, located west of the Island. Wager Bay receives freshwater from several small rivers with a combined catchment of about 28,551 km^2, and this bay is connected to Roes Welcome Sound by long, shallow (depths reaching a minimum of 30 m) narrows that restrict water movement between Wager Bay and Roes Welcome Sound (Kamula et al., 2016). In August in Wager Bay, salinity has been found to range from 29.1 to 33.3 and stable oxygen isotope composition ($\delta^{18}O$) of seawater ranged from -4.13 to -2.07 (as per an unpublished dataset from the August 2016 expedition funded by Parks Canada and Government of Nunavut Fisheries and Sealing division).

2.3 Seawater Carbonate System

The surface ocean takes up/releases CO_2 from/to the atmosphere through gas exchange in response to disequilibrium between dissolved CO_2 in seawater and gaseous CO_2 in the atmosphere (AMAP, 2013). In addition to air-sea gas exchange, which is dependent on temperature, wind, and gas concentrations, among other factors, other sources of CO_2 in seawater include respiration and remineralization of marine organic carbon, oxidation of terrestrial organic carbon, and river inputs (AMAP, 2013). Concentration of CO_2 in seawater can also be decreased through primary production (AMAP, 2013).

The carbonate system in seawater is defined by the following set of reactions (Sarmiento and Gruber, 2006):

$$CO_{2(g)} \leftrightarrow CO_{2(aq)} + H_2O \leftrightarrow H_2CO_3 \leftrightarrow H^+ + HCO_3^- \leftrightarrow 2H^+ + CO_3^{2-} \quad \text{Eq. 1}$$

Upon dissolution, gaseous CO_2 becomes aqueous CO_2, and a reaction between aqueous CO_2 and water produces carbonic acid (H_2CO_3) (Sarmiento and Gruber, 2006). H_2CO_3 is a weak acid that dissociates to produce bicarbonate (HCO_3^-) and carbonate (CO_3^{2-}) ions, releasing hydrogen (H^+) ions (i.e., protons) in the process (Sarmiento and Gruber, 2006).

Due to the difficulty of analytically differentiating between $CO_{2(aq)}$ and H_2CO_3, they are typically expressed through a hypothetical species $H_2CO_3^*$ (Sarmiento and Gruber, 2006):

$$H_2CO_3^* = CO_{2(aq)} + H_2CO_3 \quad \text{Eq. 2}$$

The carbonate system can then be expressed in terms of the following equilibria and their corresponding equilibrium constants, where brackets represent total concentrations and pCO_2 is the partial pressure of CO_2 in the atmosphere (Sarmiento and Gruber, 2006):

$$CO_{2(g)} + H_2O \leftrightarrow H_2CO_3^* \qquad K_0 = \frac{[H_2CO_3^*]}{pCO_2} \qquad \text{Eq. 3}$$

$$H_2CO_3^* \leftrightarrow H^+ + HCO_3^- \qquad K_1 = \frac{[H^+][HCO_3^-]}{[H_2CO_3^*]} \qquad \text{Eq. 4}$$

$$HCO_3^- \leftrightarrow H^+ + CO_3^{2-} \qquad K_2 = \frac{[H^+][CO_3^{2-}]}{[HCO_3^-]} \qquad \text{Eq. 5}$$

Using these equilibrium equations, it is possible to plot fractions of the three aqueous carbonate species as a function of pH, as seen in Figure 5.

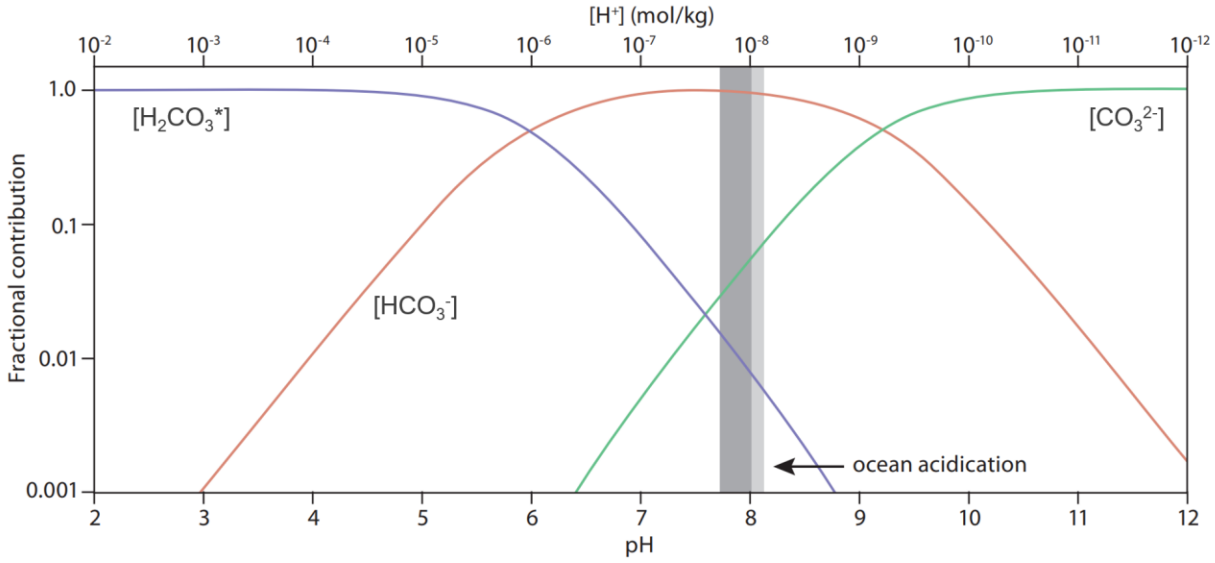

Figure 5. Fractional contribution of the carbonate system species as a function of seawater pH. The observed surface ocean acidification since the Industrial Revolution is represented by the light grey band (0.1 pH units), whereas the projected ocean acidification to the year 2100 is represented by the dark grey band (0.25 pH units). Figure modified from AMAP, 2013. © 2013 Arctic Monitoring and Assessment Programme.

In seawater, interaction of the carbonate system with other compounds that participate in acid-base reactions has the net effects of making HCO_3^- the predominant form of carbonate and pH around 8.1 (AMAP, 2013). There are four measurable variables of the carbonate system in seawater: pH, total alkalinity (TA), total dissolved CO_2 (DIC), and partial pressure of CO_2 (pCO_2) (AMAP, 2013; Sarmiento and Gruber, 2006). pH (Eq. 6) is a measure of acidity, expressed as a negative logarithm of the proton concentration (Sarmiento and Gruber, 2006). TA (Eq. 7) is a measure of the excess of bases over acids in solution (Sarmiento and Gruber, 2006).

In other words, TA is the buffering capacity of seawater, or its ability to resist acidification (AMAP, 2013). DIC (Eq. 8) is the total concentration of dissolved inorganic carbon in seawater and pCO_2 (Eq. 9) is the partial pressure exerted by CO_2 in equilibrium with seawater (Sarmiento and Gruber, 2006). It is possible to fully characterize the various components of the carbonate system with just two of the aforementioned variables (AMAP, 2013).

$$\mathrm{pH} = -\log_{10}[\mathrm{H}^+] \quad \text{Eq. 6}$$

$$\mathrm{TA} = [\mathrm{HCO_3^-}] + 2[\mathrm{CO_3^{2-}}] + [\mathrm{OH^-}] - [\mathrm{H^+}] + [\mathrm{B(OH)_4^-}] + \text{minor bases} \quad \text{Eq. 7}$$

$$\mathrm{DIC} = [\mathrm{H_2CO_3^*}] + [\mathrm{HCO_3^-}] + [\mathrm{CO_3^{2-}}] \quad \text{Eq. 8}$$

$$\mathrm{pCO_2} = \frac{[\mathrm{H_2CO_3^*}]}{\mathrm{K_0}} \quad \text{Eq. 9}$$

TA and DIC are the only two of the four variables discussed above that are conservative with changes in temperature, salinity, and pressure (Sarmiento and Gruber, 2006). Solubility of all atmospheric gases increases as water temperature decreases (Sarmiento and Gruber, 2006). That is, as a water mass loses heat, its capacity to store CO_2 increases, consequently decreasing pCO_2. Conversely, pCO_2 will increase in a water parcel that experiences warming. Temperature also has an effect on seawater pH by changing temperature-dependent equilibrium constants. With an increase in temperature, constants K_1 and K_2 from Eq. 4 and Eq. 5 will also increase, leading to greater dissociation rates of carbonic acid and bicarbonate ion (Sarmiento and Gruber, 2006). With greater dissociation of H_2CO_3 and HCO_3^- in warmer water, concentration of H^+ ion increases, consequently driving pH down. In contrast, decreases in seawater temperature would decrease the equilibrium constants, thereby increasing the pH. As a result of increased air temperatures and decreased sea ice, both consequences of climate change, sea surface temperatures in the Arctic are generally increasing (CliC/AMAP/IASC, 2016).

2.4 Ocean Acidification

As stated previously, ocean acidification is a phenomenon in which ocean pH decreases over time through the uptake of CO_2 from the atmosphere (IPCC, 2011). Simply put, at a constant TA, an increasing oceanic carbon uptake results in increases in DIC and $pCO_{2(sw)}$, and decreases in pH (AMAP, 2013). As seen in Figure 5, since the Industrial Revolution, the mean global ocean pH at the surface has already seen a reduction by 0.1 units (AMAP, 2013).

One of the major and more well-known consequences of ocean acidification is increasing solubility of the calcium carbonate mineral, $CaCO_3$ (AMAP, 2013). $CaCO_3$ is the main biogenic mineral particulate in seawater, with many marine organisms, such as molluscs, coccolithophores, and certain species of foraminifera, using it to form tests, shells and exoskeletons (Libes, 2009). The two most common forms of biogenic $CaCO_3$ in seawater are calcite and aragonite, with aragonite being the less stable form (Millero, 2013). At a given temperature, pressure, and salinity, aragonite is 1.5 times more soluble than its polymorph, calcite (Millero, 2013). In the presence of aqueous CO_2, $CaCO_3$ dissolves as shown in Eq. 10 (AMAP, 2013).

$$CaCO_{3(s)} + CO_2 + H_2O \leftrightarrow Ca^{2+} + 2HCO_3^- \quad \text{Eq. 10}$$

As seen in Eq. 10, as the concentration of dissolved CO_2 rises, more dissolution of $CaCO_3$ is expected. The likelihood of the mineral avoiding dissolution is given by its saturation state, Ω (Eq. 11) (AMAP, 2013). The saturation state of a calcium carbonate mineral is calculated as a product of concentration of calcium and carbonate ions divided by the equilibrium solubility product, K_{SP} (Eq. 12), which is dependent on temperature, pressure, and salinity (AMAP, 2013).

$$\Omega = \frac{[Ca^{2+}][CO_3^{2-}]}{K_{SP}} \quad \text{Eq. 11}$$

$$K_{SP} = [Ca^{2+}]_{sat}[CO_3^{2-}]_{sat} \quad \text{Eq. 12}$$

$CaCO_3$ becomes thermodynamically unstable when $\Omega < 1$, at which point the mineral becomes susceptible to dissolution (AMAP, 2013). These conditions make it difficult for calcifying organisms to build and maintain their $CaCO_3$ structures (AMAP, 2013).

2.5 Influences on the Seawater Carbonate System

2.5.1 Air-Sea Exchange

Sea-air flux of CO_2 can be calculated by multiplying the difference between seawater and atmospheric pCO_2 by the transfer velocity, k, as shown in Eq. 13 (Millero, 2013). The transfer velocity depends on ice conditions and wind speeds, among other factors (Millero, 2013).

$$\text{Sea} - \text{air } CO_2 \text{ flux} = k\left(pCO_{2(sw)} - pCO_{2(atm)}\right) = k\Delta pCO_2 \quad \text{Eq. 13}$$

The magnitude and direction of the disequilibrium between atmospheric and seawater pCO_2 determines the magnitude and direction of the sea-air CO_2 flux (Ahmed et al., 2020). Since

atmospheric concentrations of CO_2 are fairly stable over short timescales, whether CO_2 will be taken up or released by seawater is generally determined by $pCO_{2(sw)}$ (Ahmed et al., 2020).

Ahmed et al. (2021) found that sea-air flux of CO_2 in Hudson Bay during the 2018 BaySys cruise (May 25 – July 13, 2018) ranged from -84 to 9 mmol m^{-2} d^{-1}, with a mean of -5±9 mmol m^{-2} d^{-1}, characterizing Hudson Bay as a moderate to weak net sink for atmospheric CO_2. Previous studies in Hudson Bay found it to also be a weak CO_2 sink in October (Else et al., 2008a) and a weak source of CO_2 in August and September (Else et al., 2008b). In the fall, the air-sea CO_2 flux in the Bay was reported to be -0.73 mmol m^{-2} d^{-1} (Else et al., 2008a). In the summer to fall season, Hudson Bay was reported to have a mean air-sea flux of 1.98 mmol m^{-2} d^{-1}, indicating that there was a net outgassing of CO_2 to the atmosphere (Else et al., 2008b).

2.5.2 Freshwater

Major sources of freshwater to an ocean environment are continental runoff, ice melt, and precipitation falling directly on seawater. With greater quantities of moisture being moved from lower latitudes poleward due to climate change, precipitation is increasing in the Arctic (CliC/AMAP/IASC, 2016), and progressively, precipitation is being received as rain at the expense of snow (McCrystall et al., 2021). River runoff is also generally increasing in the Arctic as a result of climate change (CliC/AMAP/IASC, 2016). Eastern Hudson Bay and James Bay have also been seeing rising trends in river discharge, in large attributed to the diversion of Caniapiscau River into the La Grande Rivière system in Québec for hydropower production (Déry et al., 2016). Therefore, the Arctic is receiving increasingly greater freshwater inputs through greater precipitation, river runoff, and glacier and ice sheet melting rates (CliC/AMAP/IASC, 2016). As previously stated, Hudson Bay receives approximately one-third of Canada's river discharge, with peak river runoff occurring in May (Déry et al., 2011). Additionally, Hudson Bay experiences complete ice cover in winter and open water in summer. River discharge to Hudson and James Bays adds about 630 – 870 km^3 yr^{-1} of freshwater (Lammers et al., 2001; Saucier et al., 2004) and net precipitation (precipitation minus evaporation) adds another 220 km^3 yr^{-1} (St-Laurent et al., 2011). Recent estimates of ice thickness within the Hudson Bay Complex calculated the potential freshwater yield from sea-ice melt to range from 0.70 m in northwestern Hudson Bay to 1.41 m in Foxe Basin (Landy et al., 2017). These freshwater inputs result in Hudson Bay experiencing seasonal strong upper surface

layer stratification (Ferland et al., 2011; Ahmed et al., 2020), as freshwater is less dense than seawater. Stratification impedes vertical water column mixing, thereby hindering the upwelling of DIC and nutrients from deep waters, and the transport of atmospheric CO_2 to deep waters (AMAP, 2013).

Freshwater input through river run-off, sea-ice melt, and precipitation is also characterized by lower DIC, TA, pH, and Ca^{2+} ion concentration than seawater, with river run-off generally having greater alkalinity than sea-ice melt (AMAP, 2013). The addition of poorly buffered freshwater to the surface ocean reduces the capacity of surface waters to absorb CO_2, increases their sensitivity to acidification, and lowers Ω (AMAP, 2013; Azetsu-Scott et al., 2010). The extent to which this happens will depend on the source and volumes of freshwater (Azetsu-Scott et al., 2010). For example, western Hudson Bay rivers that flow through Palaeozoic limestone bedrock will have greater TA and likely greater calcium concentration than eastern Hudson Bay rivers that flow through an igneous rock watershed (Azetsu-Scott et al., 2014).

In Hudson Bay, most river runoff is contained within a nearshore coastal domain that extends to 100-150 km from shore in the southwest (Granskog et al., 2009). The Hudson Bay Complex coastal domain also encompasses part of the Riverine Coastal Domain (RCD), a term used to describe the zone extending 1 to 20 km from shore and down to water depths of 10-20 m, where many processes are driven by accumulation of river runoff (Carmack et al., 2015, 2016). Upon a river discharging into a sea, low density coastal buoyancy-boundary currents form and, due to the Coriolis force, these currents get deflected to the right in the Northern Hemisphere (Carmack et al., 2016, and references therein). As multiple continental runoff sources aggregate, a contiguous RCD forms, constituting the first step in the flux of freshwaters across shelves and into offshore environments (Carmack et al., 2016, and references therein). The RCD within this study region flows along the western coast of Foxe Basin, around the northern end of Southampton Island, through Roes Welcome Sound, and around the coast of Hudson Bay towards Hudson Strait (Carmack et al., 2015). Besides directly affecting the seawater carbonate cycle and ocean acidification through their inputs of DIC, TA, and H^+ and Ca^{2+} ions, river inflows also indirectly affect the carbonate cycle and the state of ocean acidification through their supplies of nutrients, organic matter, sediment, and heat. Fluxes of organic matter and sediment into coastal waters increase turbidity and reduce light penetration into the water

column, thereby having the potential to reduce rates of photosynthesis and increase respiration (CliC/AMAP/IASC, 2016). On the other hand, fluxes of nutrients and heat have the potential to increase primary production (CliC/AMAP/IASC, 2016).

2.5.3 Sea Ice

Relative to CO_2 fluxes observed in open waters, fluxes in waters with an incomplete or broken ice cover can be much greater in wintertime (Else et al., 2012). This could be either due to sea ice and its formation and movement causing an increase in the turbulence at the boundary layer, and/or frazil ice disrupting the sea-surface microlayer (AMAP, 2013; see also Loose et al., 2011, and references therein). It has also been found that dissolved gases get rejected from forming ice with greater efficiency than salt, with gas exchange rates in incomplete ice cover greater than would be expected from linear scaling between complete ice cover and open water area (Loose et al., 2009).

Sea ice also plays a role in the carbonate system through a process called the sea ice pump (Loose et al., 2011; Rysgaard et al., 2011). A pump is defined as a process that moves carbon from the atmosphere and surface waters to the deep sea (Emerson and Hedges, 2008). The sea ice pump is proposed to work as follows: during the formation of sea ice, brine containing inorganic carbon gets rejected (AMAP, 2013). This brine, dense and rich in inorganic carbon, sinks below the mixed layer, thereby pumping carbon to depths (AMAP, 2013). Additionally, if there is precipitation of $CaCO_3$ within the ice and the mineral does not get removed with brine, the ice becomes enriched in TA over DIC (AMAP, 2013). Once the ice melts, $CaCO_3$ might dissolve instead of sinking, raising the TA of surface waters and consequently promoting CO_2 uptake from the atmosphere (AMAP, 2013). This added carbon might get pumped from surface waters into abyssal waters when the sea ice pump process repeats the following winter (AMAP, 2013).

2.5.4 Biological Pump

During photosynthesis (Eq. 14), CO_2 is taken up by primary producers and converted to organic matter (OM) (Sarmiento and Gruber, 2006). The reverse of this process is respiration or remineralization (Sarmiento and Gruber, 2006).

$$106\ CO_2 + 16\ HNO_3 + H_3PO_4 + 78\ H_2O \leftrightarrow C_{106}H_{175}O_{42}N_{16}P + 150\ O_2 \qquad \text{Eq. 14}$$

The biological pump happens when primary production generates OM and it gets transported to deep waters by sinking particulate organic matter (POM), zooplankton migration, or transport of dissolved organic matter (DOM) (AMAP, 2013). The net result of the biological pump is an increase in pH and decrease in DIC in the euphotic zone and a decrease in pH and increase in DIC at depths where OM gets remineralized (AMAP, 2013). If OM accumulates on the seafloor without degradation, then carbon is removed from the system for long time scales. Since OM degradation in the water column is depth dependent, shallow shelf seas like Hudson Bay are expected to be sites of carbon sequestration in bottom sediments. An increased uptake of carbon due to increased primary production may lead to increased carbon storage in the ocean. Armstrong et al. (2019), using modeling, showed that the Arctic Ocean's carbon storage will increase in the coming decades, although the biological contribution to this will be small relative to the inorganic carbon pool.

As mentioned previously, climate change is leading to increased air temperatures and decreased sea ice cover, which leads to warmer sea surface temperatures in the Arctic (CliC/AMAP/IASC, 2016). The reduced sea ice cover, resulting in greater light availability, and the flux of heat from the atmosphere and rivers into the ocean generally increases biological productivity in the Arctic (CliC/AMAP/IASC, 2016). The delivery of nutrients by rivers can also increase primary production, whereas the flux of sediments and organic matter may limit light availability, which in turn reduces productivity, as previously discussed in Section 2.5.2. Most primary productivity in the ocean can be attributed to phytoplankton. During phytoplankton blooms, DIC is consumed and pH is raised, with pH values of up to 9.7 previously recorded during algal blooms (AMAP, 2013). On the other hand, remineralization of the bloom after its collapse can reduce pH and increase the concentration of DIC. The sinking of OM and the proportion of OM that reaches the seafloor are determined in large part by phytoplankton size and community structure. In Hudson Bay, sediment cores (Kuzyk et al., 2009), sediment trap data (Lapoussière et al., 2009; 2013), and a 3D coupled bio-physical ocean model (Sibert et al., 2011) have all been used to estimate carbon sinking exports and fluxes to the seafloor. A large phytoplankton-based food web establishment at the subsurface chlorophyll maxima may be supported by a longer ice-free season in Hudson Bay, which would intensify the export of carbon from pelagic diatoms to deeper waters (Jacquemot et al., 2022).

Submerged vegetation, such as seagrasses and macroalgae found on continental shelves and in estuaries, are also important to carbon sequestration and burial (Smith, 1981; Duarte et al., 2005; Duarte, 2017). A substantial portion of macroalgal production gets exported beyond their habitats (Duarte and Cebrian, 1996; Barrón and Duarte, 2015), either getting deposited in shelf sediments, or reaching the deep ocean, where it can remain for long time periods (Krause-Jensen and Duarte, 2016). Macroalgal production that does not get exported may be consumed by herbivores or detritivores, or it may get buried in sediments at the site of its growth (Duarte, 2017). Macroalgal production may also get respired or decomposed at any stage of its journey. The fate of macroalgal carbon depends in part on the form and size of macroalgae, production rates, extent, resistance to grazing and decomposition, and the potential of this carbon to reach areas where physical and biogeochemical conditions are favourable for carbon preservation (Krause-Jensen et al., 2018, and references therein). Besides their capacity to sequester and store carbon, macroalgae can also increase local rates of sedimentation (Eckman et al., 1989), slow water flows (Rosman et al., 2007), and create zones of favourable conditions for calcifiers by raising seawater pH through photosynthesis (Middelboe and Hansen, 2007). Macroalgal beds, as well as other metabolically intense ecosystems, can contribute to daily variations in pH of up to 1.0 unit (Duarte et al., 2013, and references therein). For many coastal ecosystems, metabolic processes are the primary contributors to observed pH fluctuations, greater than the contribution of pH decreases from anthropogenic CO_2 inputs (Duarte et al., 2013).

2.5.5 Carbonate Pump

The carbonate pump is a biologically mediated process whereby plankton calcification (i.e., $CaCO_3$ precipitation) results in the downward transport of carbon when the hard body structures of marine organisms sink to deep waters (Volk and Hoffert, 1985). As plankton form their shells and exoskeletons by producing $CaCO_3$ minerals, there is a corresponding decrease in CO_3^{2-} and Ca^{2+} ion concentration, which reduces TA and DIC in a 2:1 ratio, increases pCO_2, and lowers pH in the region of $CaCO_3$ precipitation (AMAP, 2013). Three notable depths are identified in the depth distributions of $CaCO_3$ in the ocean. Saturation horizon is the depth where $\Omega = 1$; below this depth, $CaCO_3$ becomes thermodynamically unstable (AMAP, 2013). The lysocline is a depth below which $CaCO_3$ dissolution rate experiences a sharp increase (Millero, 2013). Lastly, the calcium carbonate compensation depth is the water depth at which the rate of supply of $CaCO_3$ is equal to its rate of dissolution, meaning that $CaCO_3$ minerals will not reach the seafloor (Libes,

2009). As such, as $CaCO_3$ structures sink, a small fraction gets buried in the sediments, and the rest dissolve either in the sediments or in the water column, which increases TA and DIC in the region of $CaCO_3$ dissolution (AMAP, 2013).

2.5.6 Solubility Pump

Equilibrium between gaseous and aqueous CO_2 is achieved when the partial pressure of the gas in the atmosphere is equal to pCO_2 of the surface water (AMAP, 2013). This is the foundation of Henry's Law (Eq. 15), which states that the concentration of a dissolved gas is equal to the product of the partial pressure of the gas and the equilibrium constant for its solubility (Libes, 2009).

$$[H_2CO_3^*] = pCO_2 \cdot K_0 \qquad \text{Eq. 15}$$

As mentioned previously, solubility of all atmospheric gases rises as water temperature drops (Sarmiento and Gruber, 2006). In other words, the cooler the seawater gets, the more CO_2 it is able to hold. In the Atlantic Ocean, as warm surface currents flow northward, they lose heat to the atmosphere and the surface water temperature falls (AMAP, 2013). CO_2 solubility increases with falling temperatures, resulting in CO_2 undersaturation of seawater (AMAP, 2013). Consequently, the undersaturated water takes up CO_2 from the atmosphere as per Henry's Law (AMAP, 2013). With additional loss of heat, the surface water becomes denser and sinks in the process of deep water formation, driving thermohaline circulation (AMAP, 2013). Through this process, the solubility pump removes carbon from the atmosphere and moves it to the deep sea, where it remains for centuries (AMAP, 2013). However, deep water formation within the Hudson Bay Complex occurs mostly as a result of ice formation and associated brine rejection within polynyas, such as the Kivalliq Polynya in northwestern Hudson Bay (Stewart and Barber, 2010; Granskog et al., 2011; Bruneau et al., 2021) or the polynyas found in western Foxe Basin (Defossez et al., 2008, 2010).

2.6 Stable Isotopes as Tracers of Processes Affecting the Carbonate System

Isotopes are atoms that have the same number of protons but different number of neutrons, that is, they have the same atomic number but different masses (Millero, 2013). Stable isotopes are those isotopes that are chemically stable and that do not spontaneously convert to other elements (in contrast to radioactive isotopes) (Emerson and Hedges, 2008). Atoms or molecules with the same elements but different mass numbers arising from the different number of neutrons also

have different free energies (Emerson and Hedges, 2008). Due to this difference in free energy, the isotopes do not partition equally among substances in thermodynamic equilibrium, resulting in an "equilibrium isotope effect" (Emerson and Hedges, 2008). Due to their difference in mass, isotopes can also experience differential diffusion rates and/or bond breaking/forming rates, a phenomenon referred to as a "kinetic isotope effect" (Emerson and Hedges, 2008). Due to the kinetic isotope effects, molecules with the lighter isotope will diffuse or form faster, consequently enriching the remaining pool of reactants with the heavier isotope (Emerson and Hedges, 2008). As such, the equilibrium and kinetic isotope effects both lead to isotopic fractionation, which is a state of unequal isotope composition among different compounds linked by a reaction or process (Emerson and Hedges, 2008). Isotopic fractionation is both temperature and pressure dependent (Emerson and Hedges, 2008).

2.6.1 Stable Carbon Isotopes

Carbon has two stable isotopes, ^{12}C and ^{13}C, which have abundances of 98.9% and 1.1%, respectively (Emerson and Hedges, 2008). The two isotopes are differentiated as "lighter" (^{12}C) and "heavier" (^{13}C) due to differences in the mass-to-charge ratios (Emerson and Hedges, 2008). The isotopic composition of a sample is reported as the per mil (‰) relative deviation (δ) between isotope ratios of the sample and the simultaneously measured standard material (Emerson and Hedges, 2008). The carbon isotope composition of a sample would then be calculated as per Eq. 16, where R is the heavy to light isotope ratio quotient (Emerson and Hedges, 2008). The standard material typically used in stable carbon isotope composition analyses is Vienna PeeDee Belemnite (VPDB).

$$\delta^{13}C = \left[\frac{(^{13}C/^{12}C)_{sample} - (^{13}C/^{12}C)_{standard}}{(^{13}C/^{12}C)_{standard}}\right] \cdot 1000 = \left[\frac{R_{sample} - R_{standard}}{R_{standard}}\right] \cdot 1000 \quad \text{Eq. 16}$$

The difference between the product's and reactant's δ values is the difference fractionation factor, ε (Emerson and Hedges, 2008). Eq. 17 shows how ε is calculated for ^{13}C.

$$\varepsilon^{13}C = \delta^{13}C_{product} - \delta^{13}C_{reactant} \quad \text{Eq. 17}$$

As described in previous sections, DIC concentration in seawater may increase due to air-sea gas exchange, oxidation of terrestrial organic carbon, and respiration and remineralization of marine organic carbon. The generated excess of DIC may then be released to the atmosphere as CO_2 during air-sea gas exchange or it may be taken up by primary producers during photosynthesis,

being converted from inorganic to organic carbon. The degree to which the various sources and sinks of DIC affect the seawater carbonate system cannot be understood by looking at DIC concentrations alone. One approach to distinguishing between the relative importance of each of these processes in a given region is to look at the stable carbon isotopic composition of DIC, $\delta^{13}C_{DIC}$, since each major reaction involving DIC is associated with a unique change in $\delta^{13}C_{DIC}$. In other words, air-sea CO_2 exchange, metabolic processes, formation and dissolution of $CaCO_3$, degradation of CH_4, and addition and removal of freshwater all result in variations in the concentration and stable carbon isotopic composition of DIC.

The $\delta^{13}C$ of atmospheric CO_2 has been reported to be about -8.4‰ in 2015 (Graven et al., 2020), and the typical seawater $\delta^{13}C_{DIC}$ values are around 0-2‰ (Burt et al., 2016). As such, the uptake of ^{13}C-depleted atmospheric CO_2 by surface waters would lower $\delta^{13}C_{DIC}$ while simultaneously increasing DIC. It has been estimated that an uptake in the North Atlantic of 100 μmol kg^{-1} of atmospheric DIC would reduce surface water $\delta^{13}C$ by 0.5‰ (Lynch-Stieglitz et al., 1995). The opposite is true when CO_2 gets released from surface waters to the atmosphere, surface ocean $\delta^{13}C_{DIC}$ increases while DIC decreases (Inoue and Sugimura, 1985). However, since it takes over 5 years to achieve isotopic equilibrium between ^{12}C and ^{13}C of the atmosphere and surface seawater, fractionation due to air-sea CO_2 exchange may be considered negligible in water bodies where surface water residence time is considerably shorter than the time it takes to achieve isotopic equilibrium (Sarmiento and Gruber, 2006).

Among processes occurring within a water column (excluding methane degradation, which is unlikely to be a key player in oxic ocean environments given methane's relatively low concentrations and slow degradation rates (e.g., Kitidis et al., 2010)), photosynthesis by primary producers results in the greatest fractionation of stable carbon isotopes. Organic matter preferentially takes up ^{12}C over ^{13}C during photosynthesis, resulting in $\delta^{13}C$ of organic matter decreasing, while $\delta^{13}C$ of the remaining pool of DIC in the surrounding water increases (Sarmiento and Gruber, 2006). Photosynthetic fractionation of stable carbon isotopes by marine primary producers ranges from ε = -30‰ to -18‰ (Zeebe and Wolf-Gladrow, 2001; Hoefs, 2009), depending on the species and growth rate of phytoplankton and the fugacity of CO_2 (Emerson and Hedges, 2008). Respiration (i.e., degradation of dissolved and/or particulate organic matter) does not result in isotopic fractionation of carbon (Norrman et al., 1995; Hullar

et al., 1996; Emerson and Hedges, 2008). However, respiration of isotopically light organic matter will lower the $\delta^{13}C$ value of the surrounding pool of DIC. As such, with photosynthesis being limited to the euphotic zone and respiration occurring throughout the water column, biological processes can create gradients in DIC concentration and $\delta^{13}C_{DIC}$ values with depth in a water column. In like manner as DIC, phosphate is also consumed by photosynthesis and released by respiration; consequently, there is an inverse correlation between the concentration of phosphate and $\delta^{13}C_{DIC}$ (Broecker and Peng, 1982). An example of vertical profiles of DIC, $\delta^{13}C_{DIC}$, dissolved oxygen, and dissolved inorganic phosphorus are shown in Figure 6 to illustrate the correlations and anticorrelations between these variables.

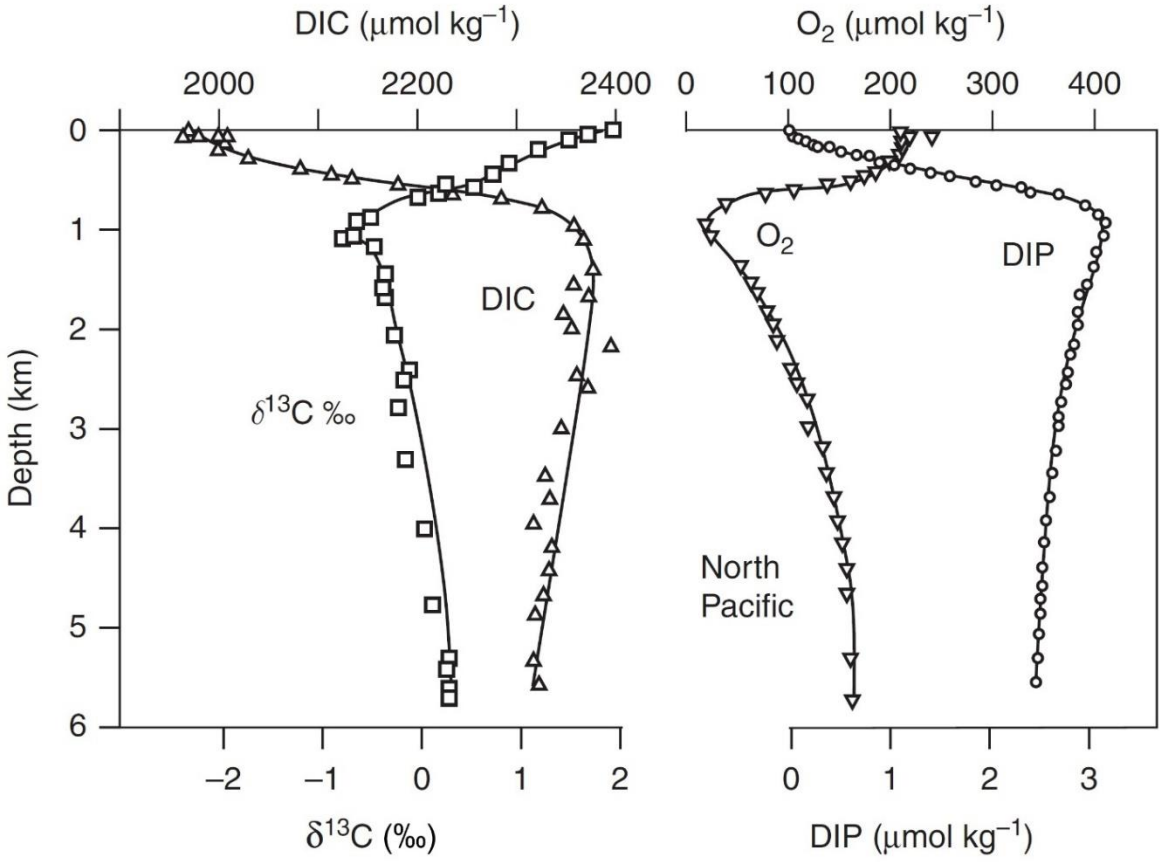

Figure 6. Profiles of dissolved inorganic carbon (DIC), stable carbon isotope ratios of DIC ($\delta^{13}C$), dissolved oxygen (O_2) and dissolved inorganic phosphorus (DIP) in the north Pacific Ocean. Figure from Emerson and Hedges (2008). © 2008 S. R. Emerson and J. I. Hedges.

Plotting $\delta^{13}C_{DIC}$ against phosphate concentration for a given region where photosynthesis and respiration were the only sources of perturbation would give a slope, $\frac{\Delta\delta^{13}C_{DIC}}{\Delta PO_4}$, as per Eq. 18 (Broecker and Peng, 1982):

$$\frac{\Delta\delta^{13}C_{DIC}}{\Delta PO_4} = \frac{\varepsilon^{13}C_{plant-DIC}}{DIC_{mean}} \cdot \left[\frac{C}{P}\right]_{OM} \quad \text{Eq. 18}$$

where $\varepsilon^{13}C_{plant\text{-}DIC}$ is the biological difference fractionation factor of ^{13}C ($\varepsilon^{13}C_{plant\text{-}DIC} = \delta^{13}C_{plant} - \delta^{13}C_{DIC}$), DIC_{mean} is the mean seawater DIC concentration, and $[C/P]_{OM}$ is the carbon to phosphate ratio of phytoplankton-derived organic matter (106:1; Redfield et al., 1963). By solving for the $\frac{\varepsilon^{13}C_{plant-DIC}}{DIC_{mean}}$ term using Eq. 18, it is possible to estimate respiratory DIC inputs from the change in $\delta^{13}C_{DIC}$. It is important to note that low values of $\delta^{13}C$ can also be a result of riverine input, not just respiration (as is assumed in Eq. 18). Dissolution of biogenic soils and carbonate bedrock tend to produce $\delta^{13}C_{DIC}$ values of about -25‰ and 0‰, respectively (Spiker, 1980). Hudson Bay rivers were found to be enriched in ^{13}C at an average $\delta^{13}C_{DIC}$ value of -3.2‰ (Burt et al., 2016). Note that this average does not account for southwestern rivers (Churchill, Severn, Winisk, Hayes, and Nelson) as those rivers were not sampled in the Burt et al. (2016) study. The Churchill, Nelson, and Hayes rivers are expected to have more negative values of $\delta^{13}C_{DIC}$ (Burt et al., 2016).

2.6.2 Stable Oxygen Isotopes

Two of the stable oxygen isotopes, ^{16}O and ^{18}O, have abundances of 99.8% and 0.2%, respectively (Emerson and Hedges, 2008). The oxygen isotope composition of a sample is calculated as per Eq. 19, where R is the heavy to light isotope ratio quotient (Emerson and Hedges, 2008). The standard material typically used in stable oxygen isotope composition analyses is Vienna Standard Mean Ocean Water (VSMOW).

$$\delta^{18}O = \left[\frac{(^{18}O/^{16}O)_{sample} - (^{18}O/^{16}O)_{standard}}{(^{18}O/^{16}O)_{standard}}\right] \cdot 1000 = \left[\frac{R_{sample} - R_{standard}}{R_{standard}}\right] \cdot 1000 \quad \text{Eq. 19}$$

Water molecules containing the heavy oxygen isotope ($H_2{}^{18}O$) are harder to evaporate and easier to precipitate than water molecules containing the light oxygen isotope ($H_2{}^{16}O$) (Emerson and Hedges, 2008). Consequently, during evaporation, fractionation of stable oxygen isotopes leaves the remaining water enriched in ^{18}O. As temperature decreases, fractionation due to evaporation increases, e.g., $\varepsilon(\delta^{18}O\text{-}H_2O_{condensate} - \delta^{18}O\text{-}H_2O_{vapour})$ is 9-9.8‰ at 20°C and 11-11.7‰ at 0°C

(Majoube, 1971; Emerson and Hedges, 2008). During condensation and precipitation, fractionation leaves the remaining water vapor enriched in ^{16}O, as isotopically heavy water preferentially precipitates out. On a global scale then, it is observed that slightly ^{18}O-depleted water evaporates from sub-tropical waters and ^{18}O-enriched water is lost to condensation and precipitation over mid-latitudes, so that water vapour becomes increasingly ^{18}O-depleted with increasing latitude (Emerson and Hedges, 2008). As a result, precipitation above 50ºN typically has $\delta^{18}O$ values of -25‰ to -10‰, depending on location (IAEA, 2001). Formation of sea ice also results in slight fractionation of stable oxygen isotopes in seawater. As sea ice forms, it preferentially incorporates ^{18}O into its structure, with $\varepsilon(\delta^{18}O\text{-}H_2O_{ice} - \delta^{18}O\text{-}H_2O_{water})$ at 0°C being between 2.8‰ (Suzuoki and Kimura, 1973) and 3.1‰ (O'Neil, 1968). $\delta^{18}O$ values of water are practically not affected by any biochemical processes and are only altered by physical processes (evaporation/precipitation, freezing/melting, and water mass mixing). Consequently, $\delta^{18}O$ of water can be used as a water mass tracer as different water masses have distinct $\delta^{18}O$ signatures. That is, $\delta^{18}O$ can be used in conjunction with salinity (S) to estimate fractions of sea-ice meltwater (f_{SIM}), meteoric water (f_{MW}, includes riverine input and direct precipitation), and seawater (f_{SW}), as per mass-balance equations shown by Eq. 20, Eq. 21, and Eq. 22 (Östlund and Hut, 1984).

$$S_{sample} = S_{SW} \cdot f_{SW} + S_{SIM} \cdot f_{SIM} + S_{MW} \cdot f_{MW} \quad \text{Eq. 20}$$

$$\delta^{18}O_{sample} = \delta^{18}O_{SW} \cdot f_{SW} + \delta^{18}O_{SIM} \cdot f_{SIM} + \delta^{18}O_{MW} \cdot f_{MW} \quad \text{Eq. 21}$$

$$f_{SW} + f_{SIM} + f_{MW} = 1 \quad \text{Eq. 22}$$

Hudson Bay rivers have $\delta^{18}O$ values ranging from -16.82 to -10.76‰ (Burt et al., 2016). End-member values for Hudson Bay determined by Ahmed et al. (2020) and Granskog et al. (2011) are listed in Table 2. Values presented in Ahmed et al. (2020) are based on samples collected in the spring of 2018, while values presented in Granskog et al. (2011) are from late-summer and fall sampling in 2005 (except for river samples, which were mostly sampled during the summers of 2005-2007). The values determined by Ahmed et al. (2020) and Granskog et al. (2011) are notably different for the SW end-member and for the salinity of the SIM end-member. Ahmed et al. (2020) determined their SW end-member by averaging values from 45 surface samples, whereas Granskog et al. (2011) chose their SW end-member values as the point of transition on a $\delta^{18}O$-salinity plot from a mostly two-component system (Hudson Strait waters and deeper waters

in Foxe Basin and Hudson Bay at the entrance to Hudson Strait) to a three-component system in Hudson and James Bays. Ahmed et al. (2020) attributed the differences in salinity of SIM to the timing of sample collection, with their samples being collected in late spring after brine drainage had occurred, whereas Granskog et al. (2011) chose their values based on landfast sea ice sampled in winter and spring.

Table 2. Salinity and stable oxygen isotope ratio ($\delta^{18}O$) end-member values estimated for Hudson Bay. Uncertainties are based on one standard deviation.

	Ahmed et al. (2020)		**Granskog et al. (2011)**	
Water Mass	**Salinity**	**$\delta^{18}O$ (‰)**	**Salinity**	**$\delta^{18}O$ (‰)**
Seawater	32.1±0.1	-2.5±0.2	32.8±0.1	-1.5±0.2
Sea-ice melt	1.4±0.5	-0.8±0.2	5.0±1.0	0.0±0.5
Meteoric water	0.05±0.1	-15.4±0.2	0.1±0.1	-14.0±1.0

2.7 Apparent Oxygen Utilization

Apparent oxygen utilization (AOU) measures how dissolved oxygen concentration in a water parcel has changed since the parcel was transported to interior ocean and stopped being in contact with the atmosphere (Sarmiento and Gruber, 2006). As such, AOU estimates cumulative aerobic remineralization in seawater since the water parcel was last at the surface (Sarmiento and Gruber, 2006). AOU is calculated as the difference between dissolved oxygen equilibrium saturation concentration ($[O_2]_{sat}$) and observed dissolved oxygen concentration ($[O_2]_{obs}$), as per Eq. 23 (Sarmiento and Gruber, 2006).

$$\mathrm{AOU} = [\mathrm{O_2}]_{\mathrm{sat}} - [\mathrm{O_2}]_{\mathrm{obs}} \qquad \text{Eq. 23}$$

$[O_2]_{sat}$ is the expected O_2 concentration of a water parcel if it was at equilibrium with the atmosphere at sea pressure of 0 db and at its in-situ salinity and potential temperature, θ (Libes, 2009). θ is the temperature a water parcel would have if it were adiabatically brought to sea surface (Libes, 2009).

Chapter 3: Methods

3.1 Data Collection

Data collection for the Southampton Island Marine Ecosystem Project (SIMEP) took place from August 6 – 27, 2019, aboard RV *William Kennedy*. The cruise began in Coral Harbour, Nunavut, proceeded clockwise around Southampton Island, ending back in Coral Harbour. Twenty-two stations were sampled for salinity, dissolved inorganic carbon (DIC), total alkalinity (TA), stable oxygen isotope ratio of seawater ($\delta^{18}O\text{-}H_2O$), and stable carbon isotope ratio of DIC ($\delta^{13}C_{DIC}$) (note that 2 stations are missing $\delta^{13}C_{DIC}$ data), providing comprehensive full water column coverage. Locations of stations sampled are shown in Figure 7.

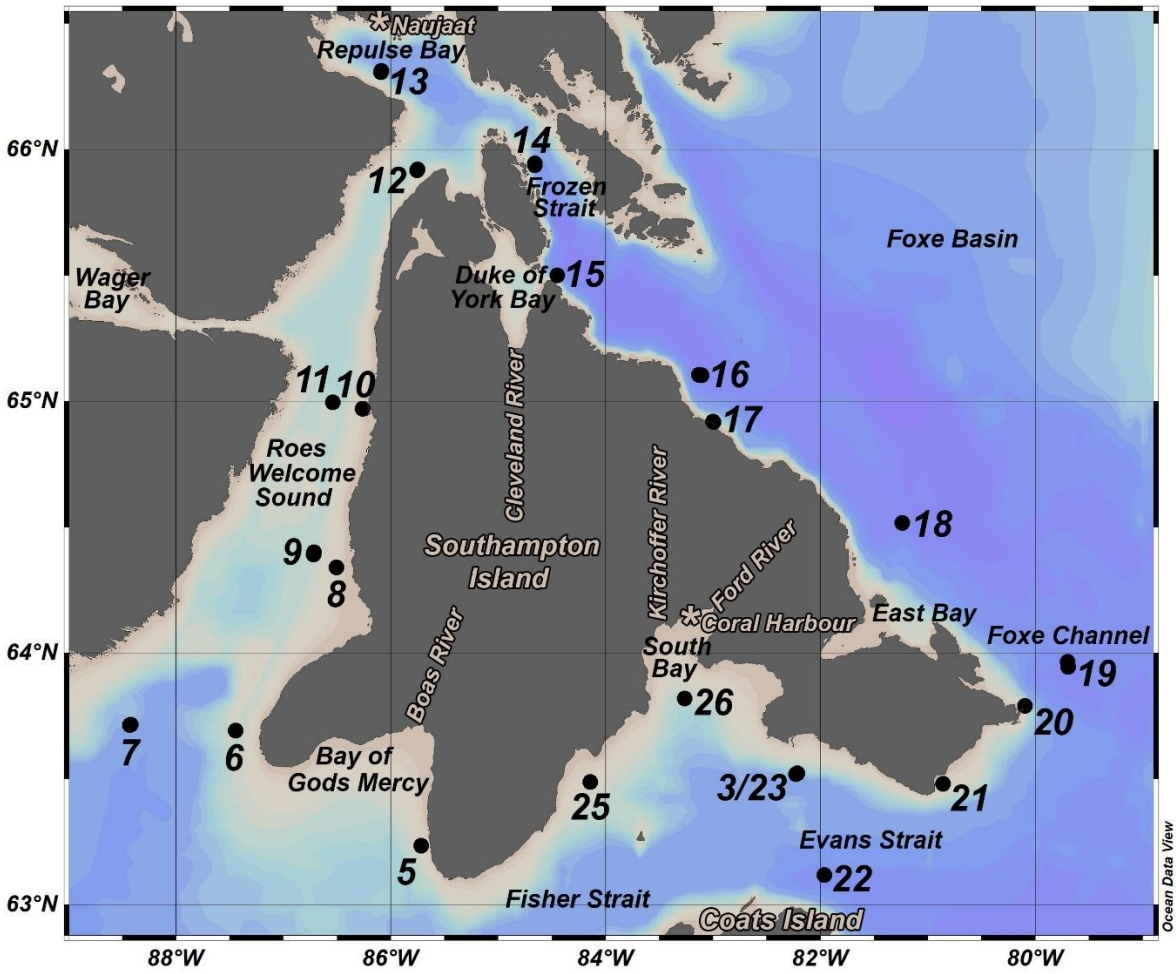

Figure 7. Stations sampled during the 2019 SIMEP cruise. In total, 22 stations were sampled between August 6 and 27, 2019. Communities of Coral Harbour (also known as Salliq) and Naujaat are marked with asterisks. Boas River discharging into Bay of Gods Mercy, Kirchoffer and Ford Rivers discharging into South Bay, and Cleveland River discharging into Duke of York Bay are also marked.

Water samples were collected using a Seabird rosette equipped with 12 5-L Niskin bottles and a Seabird 19 plus V2 CTD profiler with several auxiliary sensors. The CTD measured pressure, conductivity, and temperature, and an auxiliary SBE 43 sensor measured dissolved oxygen concentration (see Table 3 for sensor specifications).

Table 3. Specifications of select rosette sensors used during the 2019 SIMEP cruise, as per Sea-Bird Electronics (2016) and Sea-Bird Scientific (2022).

Sensor	Measurement range	Initial accuracy	Resolution
Temperature	-5 to 35°C	±0.005°C	0.0001°C
Conductivity	0 to 9 S/m	±0.0005 S/m	- 0.00005 S/m (most oceanic water; resolves 0.4 ppm in salinity) - 0.00007 S/m (high salinity water; resolves 0.4 ppm in salinity)
Pressure	0 to 350 m	±0.1% of full-scale range	0.002% of full-scale range
Dissolved oxygen (SBE 43)	120% of surface saturation in all natural waters (fresh and salt)	±2% of saturation	NA

The CTD depth was used as the depth measurement in every calculation and figure in this document. The CTD sensors were located at the bottom of the rosette. As such, the "true" depth of water collected by rosette bottles was roughly 1 m higher than the CTD reading. For example, section plots of discrete samples in this study show that the surface sample of Station 5 was collected at 1.9 m (CTD depth), however, the "true" depth of that water sample would have been around 0.9 m (CTD depth minus ~1 m). Considering that rosette mixes water during its travel through the water column, and that it likely entrains deeper water during its upcast (e.g., see Burt et al., 2016), no corrections were implemented to account for the difference between CTD depth and "true" depth of a water sample, and CTD depth was used throughout this document for all figures and calculations.

SIMEP 2019 water samples were collected in the following order: DIC/TA, $\delta^{13}C_{DIC}$, and bulk water, from which $\delta^{18}O\text{-}H_2O$ and salinity were then subsampled. DIC/TA samples were collected in either 250-mL or 500-mL borosilicate glass bottles with glass stoppers or 60-mL clear glass vials with rubber stoppers and aluminum crimp seals. The 60-mL vials were only used after the

inventory of larger bottles was exhausted. In total the 60-mL vials were used only 17 times out of 167 DIC/TA samples. First, a sampling tubing was connected to the Niskin spigot and the water was allowed to run through the tubing to clean it and to remove any air bubbles. The glass DIC/TA bottles were then filled smoothly from the bottom, with tubing touching the bottom of the bottle, and were overflowed one and a half times their volume (three times their volume for 60-mL vials). The glass stopper was inserted to prevent contamination. $\delta^{13}C_{DIC}$ samples were collected in 30-mL amber glass vials with conical screw caps using the same technique but were overflowed by three times their volume. 400 mL of bulk water were collected for most samples directly from the rosette in pre-acid-washed 500-mL Nalgene bottles which were rinsed three times with sample water. After all sampling from the rosette was completed (10-15 minutes), ~1% of the stoppered DIC/TA sample volume was removed to prevent bottles from breaking in case of thermal expansion. The DIC/TA and $\delta^{13}C_{DIC}$ samples were then spiked with saturated mercuric chloride solution to halt biological activity, with volumes of $HgCl_2$ used outlined in Table 4. Once the samples were spiked, the DIC/TA stopper was greased and the sample was securely closed with electrical tape around the bottle neck and stopper, and $\delta^{13}C_{DIC}$ samples were parafilmed.

Table 4. Volumes of saturated mercuric chloride ($HgCl_2$) solution used to spike gas samples.

Variable	**Vial type**	**Volume of $HgCl_2$ used (µL)**
DIC/TA	250-mL borosilicate glass bottle with glass stopper	100
	500-mL borosilicate glass bottle with glass stopper	200
	60-mL clear glass vial with rubber stopper and aluminum crimp seal	40
$\delta^{13}C_{DIC}$	30-mL amber glass vial with conical screw cap	20

Bulk water was subsampled within an hour for $\delta^{18}O\text{-}H_2O$ and salinity. $\delta^{18}O\text{-}H_2O$ samples were collected in 20-mL glass scintillation vials with a watertight seal, parafilmed, and stored in a dry, dark place. Salinity samples were collected in 125-mL glass bottles. The bottles were rinsed 3 times with sample water before filling. This project also used data collected by E. Kitching during the 2019 SIMEP cruise. Phosphate (PO_4^{3-}), silicic acid ($Si(OH)_4$), nitrite (NO_2^-), and combined nitrate and nitrite ($NO_3^- + NO_2^-$) concentrations were sampled by filtering seawater using a syringe (acid washed and rinsed with sample water) and pre-baked (450°C for 5 hours)

Whatman GF/F filters into 5-mL vials (acid washed and rinsed with sample water). The samples were stored in a -20°C freezer.

3.2 Sample Analyses

In total, 150 DIC/TA samples were analyzed at the Bedford Institute of Oceanography (BIO, DFO, Dartmouth, NS) in January 2020 and 17 DIC/TA samples were analyzed at the Canada Excellence Research Chairs (CERC) laboratory at the University of Manitoba (Winnipeg, MB) in December 2020. At BIO, DIC was measured following methods of Johnson et al. (1993). Acidified water samples were purged with a stream of high purity nitrogen in an automated gas extraction system. The dried gas stream was analyzed for CO_2 by coulometry (UIC Inc., Joliet, USA). Following Dickson et al. (2007), a series of sodium carbonate solutions were used to calibrate the method. At the CERC laboratory, DIC was measured on an auto-analyzer (AS-C3, Apollo SciTech, Newark, DE, USA) by adding 1 mL of 10% H_3PO_4 to a 0.75-mL subsample followed by non-dispersive infrared CO_2 detection (LI-7000, LI-COR, Lincoln, NE). Results from both laboratories were normalized to measurements of a certified reference material (CRM, batch #183 (BIO) and 185 (CERC)) prepared by Dr. Andrew Dickson of the Scripps Institution of Oceanography (San Diego, USA). Analytical precisions of DIC analyzers were 0.03% at BIO and 0.5% at the CERC laboratory.

At BIO, TA was analyzed by open-cell potentiometric titration following methods described by Dickson et al. (2007). An automated sample handling system delivered calibrated 50 mL of seawater to a beaker held at 25°C. Using a computer controlled Dosimat dispenser, 0.1N HCl was used to titrate the samples to the Gran equivalence point as measured by a combination glass electrode. At the CERC laboratory, TA was measured using Gran titration (Gran, 1952) of a ~12-mL sample with 0.05M HCl solution on a TIM-840 titration system (Radiometer Analytical, ATS Scientific, Burlington, Ontario, Canada) equipped with a temperature probe (Radiometer Analytical, Lyon, France) and an Orion ROSS Sure-Flow pH electrode (Orion 8172BNWP, Thermo Scientific). Results from both laboratories were normalized to measurements of a CRM (batch #183 (BIO) and 185 (CERC)) prepared by Dr. Andrew Dickson (Scripps Institution of Oceanography, San Diego, USA). Analytical precisions of TA analyzers were 0.05% at BIO and 0.3% at the CERC laboratory.

A correction for the dilution by mercuric chloride was applied to the DIC and TA data. 0.04% by volume saturated mercuric chloride was used (0.07% for samples collected in 60-mL vials), therefore the DIC and TA values were multiplied by 1.0004 (1.0007 for samples collected in 60-mL vials) to obtain the DIC and TA values in the original seawater sample prior to preservation by $HgCl_2$. A decision was made not to implement a correction that would account for the exchange of CO_2 with the headspace in the sampling bottle as the exact headspace volume of each sample was unknown, but headspace was under 2% by volume for all samples, thus the correction would not have been significant.

Salinity samples were analyzed at BIO (DFO, Dartmouth, NS) in December 2019 on the Guildline 8400b "Autosal" Laboratory Salinometer with a precision better than 0.002. $\delta^{18}O\text{-}H_2O$ samples were analyzed at the Ján Veizer Stable Isotope Laboratory (University of Ottawa, Ottawa, ON) in February 2020 on a Finnigan MAT Delta plus XP stable isotope ratio mass spectrometer and a GasBench II. Results were normalized to VSMOW using three calibrated internal standards covering most of the natural range. The routine precision of the analysis is reported by the laboratory to be ±0.15‰ (2σ). $\delta^{13}C_{DIC}$ samples were analyzed at the Stable Isotope Laboratory (University of Manitoba, Winnipeg, MB) in March 2021 on a GasBench II (Thermo Finnigan™) connected to a Delta V Plus Isotope-Ratio Mass-Spectrometer (IRMS, Thermo Finnigan™) via an open-split interface (ConFlo IV, Thermo Finnigan™). Analytical precision of the $\delta^{13}C_{DIC}$ analyzer was ±0.05‰. PO_4^{3-}, $Si(OH)_4$, NO_2^-, and $NO_3^- + NO_2^-$ samples were analyzed at the Maurice Lamontagne Institute (DFO, Mont-Joli, QC) in October-November 2020 on a Seal Analytical segmented flow analyzer (Model AA3) with dual channel high resolution colorimeters. Average analytical precision values for PO_4^{3-}, $Si(OH)_4$, NO_2^-, and $NO_3^- + NO_2^-$ analyses reported for 2019 to 2022 were 3.8%, 1.3%, 6.9%, and 0.94%, respectively.

3.3 Specification on Salinity and Temperature Data Used

Throughout this thesis, bottle salinity values (i.e., salinity analyzed from discrete water samples) were used for figures and calculations. Where other water samples were collected but bottle salinity values were missing, the missing values (n = 7/160) were replaced with CTD salinity from the upcast rosette bottle files so that each water sample had an associated salinity value. Figure 8 shows that there is no offset between bottle salinity (sample values) and CTD salinity from the upcast rosette bottle files.

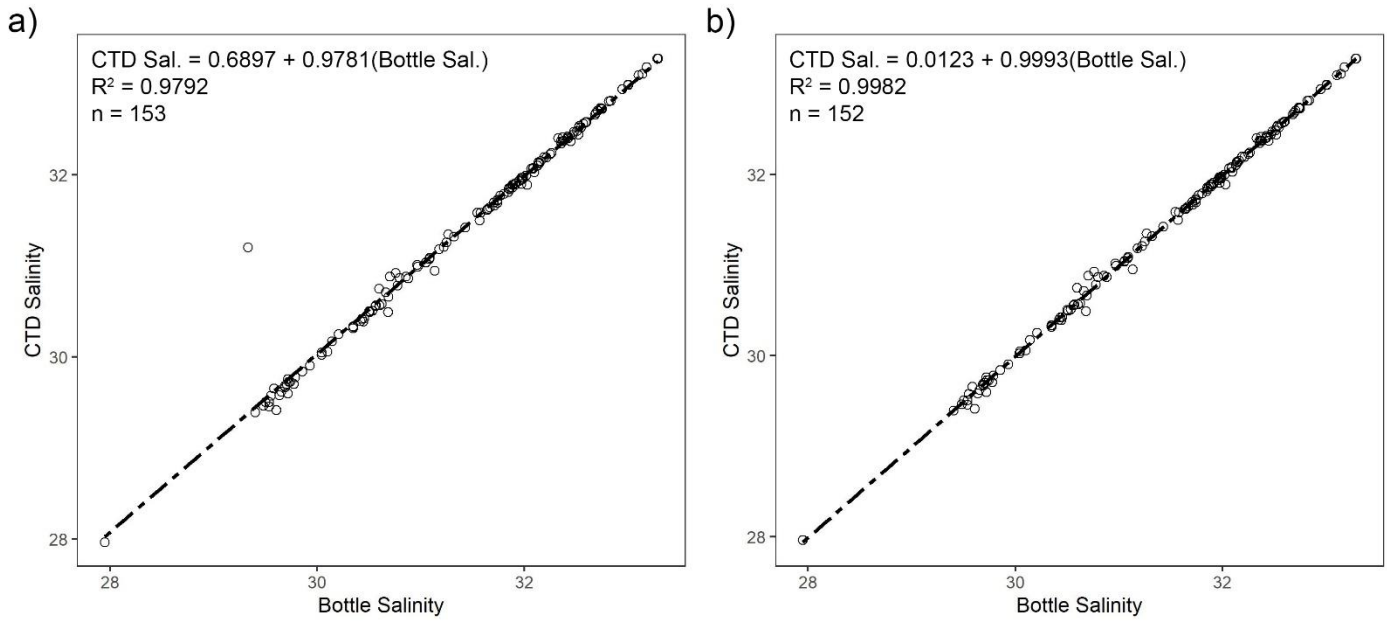

Figure 8. Rosette CTD salinity values plotted against bottle salinity values. CTD salinity values are from rosette bottle (i.e., upcast) files, and bottle salinity values are from analyzed samples. Plot a includes all available values, while plot b excludes one outlier. Linear regression lines, regression equations, and R^2 values are shown.

Downcast rosette CTD temperatures were used for one surface plot and one section plot of temperature values in Section 4.1. Due to errors in processing of the rosette CTD downcasts, data from the top 5 m of all casts needed to be removed, and values at 5 m depth were considered "surface" values. If there were multiple casts completed at one station, only values from the first downcast were used to represent the least disturbed water column, except Stations 11 and 12 where the second downcasts had to be used. For all other figures and for all calculations in this document, temperature (or potential temperature, θ) values from the upcast rosette bottle files were used. Upcast temperature values are recorded at the time of Niskin bottles closing; thus, the upcast values represent the true in-situ temperature of the collected water samples.

3.4 Carbonate System Calculations

DIC, TA, PO_4^{3-} (in lieu of total P), $Si(OH)_4$ (in lieu of total Si), bottle salinity, and CTD temperature and pressure data from the rosette bottle files (i.e., upcast values) were used as

inputs in an MS Excel program developed for CO_2 system calculations (version 3.0, Pierrot et al., 2021). Constants used in the calculations were K_1 and K_2 from Lueker et al. (2000), KSO_4 from Dickson (1990), KF from Perez and Fraga (1987), and total boron value from Lee et al. (2010). No DIC and TA values that were deemed questionable or bad by the analyzing laboratory were used in this analysis. In cases of missing PO_4^{3-} and $Si(OH)_4$ concentration values, concentration of 0 was assumed. Concentrations of total NH_3 and total H_2S were assumed to be 0 for the calculations. Missing bottle salinity values (n = 7 out of 160) were replaced by CTD salinity measurements from the rosette bottle files (i.e., upcast values). R package oce (Kelley and Richards, 2021) was used to determine seawater density (ρ; calculated using Gibbs Seawater (GSW) Equation of State, longitude, latitude, and in-situ salinity, temperature, and pressure) in order to convert some concentrations from mass per volume to mass per mass. The output of the calculations includes values of pH on the total scale, pCO_2, and calcium carbonate solubility (Ω_{ca} and Ω_{ar}).

Increase (decrease) in water temperature can decrease (increase) gas solubility, thereby driving changes in pCO_2, as discussed in Section 2.3. In order to determine temperature-normalized values of pCO_2, i.e., pCO_2 values with effects of localized water warming and cooling removed, equation of Takahashi et al. (1993, 2002) was used:

$$pCO_2(\text{at } T_{mean}) = pCO_{2(obs)} \cdot \exp(0.0423(T_{mean} - T_{obs})) \quad \text{Eq. 24}$$

where T is the seawater temperature in °C and the subscripts "mean" and "obs" stand for average and observed values, respectively. The mean water temperature associated with surface pCO_2 values was 5.03±2.75°C (mean ± standard deviation, n = 17). Using Eq. 24, temperature-normalized values of pCO_2 at 5°C were derived.

3.5 Freshwater Fractions Calculations

Fractions of seawater (f_{SW}), sea-ice meltwater (f_{SIM}), and meteoric water (f_{MW}) were calculated for each sample using bottle salinities (except when bottle salinities were missing, CTD salinity values from rosette bottle (i.e., upcast) files were used) and $\delta^{18}O$-H_2O data using a three-end-member mixing model (Eq. 20, Eq. 21, and Eq. 22; Östlund and Hut, 1984) described in Section 2.6.2. Selection of end-member values is described in Section 4.2.

Jones and Anderson (1994) defined "excess" TA (ΔTA) as differences in TA between samples and a given water mass, corrected for differences in salinity. ΔTA is used as a tracer of water masses to understand the relative prevalence of different influences. Following their approach, ΔTA was calculated as follows (Eq. 25):

$$\Delta TA = TA_{measured} - \frac{S_{measured}}{S_{Pac}} \cdot TA_{Pac} \quad \text{Eq. 25}$$

where S_{Pac} and TA_{Pac} were salinity and TA end-members of Pacific water as defined by Jones et al. (2008), 32 and 2250 µmol kg^{-1}, respectively, and $S_{measured}$ were bottle salinity values (except when bottle salinities were missing, CTD salinity values from rosette bottle (i.e., upcast) files were used). The Pacific end-member was chosen for this calculation as source seawaters in the study region were most likely to be of Pacific origin based on general circulation in the region (see Figure 2, Section 2.2); however, the interpretation of the results would have been the same if an Atlantic end-member was used instead.

3.6 Calculations of Apparent Oxygen Utilization and Dissolved Oxygen Saturation

In order to determine AOU and dissolved oxygen saturation ($[O_2]_{sat}$) values for each collected water sample, in-situ oxygen concentration values ($[O_2]_{obs}$, measured by the rosette CTD profiler at sample locations during the upcast) were first converted from units of mg L^{-1} to µmol kg^{-1} using molar weight of O_2 of 31.9988 g mol^{-1} and ρ. ρ and θ_{ITS-90} were both calculated with the R package oce (Kelley and Richards, 2021) using GSW Equation of State, coordinates, in-situ salinity, temperature, and pressure, and for θ_{ITS-90}, a reference pressure of 0 db. For in-situ salinity, bottle salinity values were used, or when bottle salinities were missing, CTD salinity values from the upcast rosette bottle files were used. For in-situ temperature and pressure, CTD values from the upcast rosette bottle files were used. $\theta_{IPTS-68}$, necessary for calculation of $[O_2]_{sat}$, was calculated by multiplying θ_{ITS-90} by 1.00024 (Saunders, 1990).

$[O_2]_{sat}$ was calculated using Eq. 26 (Garcia and Gordon, 1992, 1993), using observed practical salinity (S) from bottle samples or upcast CTD values, $\theta_{IPTS-68}$, and a set of constants.

$$\ln([O_2]_{sat})\ (\mu mol\ kg^{-1}) = A_0 + A_1 \cdot T_s + A_2 \cdot T_s^2 + A_3 \cdot T_s^3 + A_4 \cdot T_s^4 + A_5 \cdot T_s^5 + S(B_0 + B_1 \cdot T_s + B_2 \cdot T_s^2 + B_3 \cdot T_s^3) + C_0 \cdot S^2 \quad \text{Eq. 26}$$

where $T_s = \ln\left[\frac{298.15 - \theta_{IPTS-68}}{273.15 + \theta_{IPTS-68}}\right]$, with $\theta_{IPTS-68}$ in ℃.

The constants for Eq. 26 are as follows (Garcia and Gordon, 1992, 1993):

A_0	A_1	A_2	A_3	A_4	A_5
5.80871	3.20291	4.17887	5.10006	-9.86643×10^{-2}	3.80369
B_0	B_1	B_2	B_3	C_0	
-7.01577×10^{-3}	-7.70028×10^{-3}	-1.13864×10^{-2}	-9.51519×10^{-3}	-2.75915×10^{-7}	

AOU was then calculated as the difference between $[O_2]_{sat}$ and $[O_2]_{obs}$, as per Eq. 23 in Section 2.7.

3.7 Calculations of Saturation States of Partial Pressure of Carbon Dioxide

In order to determine the percent saturation of pCO_2 in seawater, it was first assumed that the partial pressure of water (pH_2O) was saturated at the water surface. In order to calculate atmospheric water vapor pressure at saturation, the following equation (Eq. 27) from Weiss and Price (1980) was used:

$$pH_2O(S,T) = \exp\left(24.4543 - 67.4509\left(\frac{100}{T}\right) - 4.8489\ln\left(\frac{T}{100}\right) - 0.000544S\right) \quad \text{Eq. 27}$$

where $pH_2O(S,T)$ is the water vapor pressure (in atm) at a specified salinity (S) and temperature (T, in Kelvins). In these calculations, S and T are bottle salinity and associated temperature values (from upcast rosette bottle files) of the surface (1.2 – 3.5 m) samples. Station 18 was not included in calculations outlined in this section as technical difficulties were experienced with the rosette and samples from the top 60 m of the water column could not be obtained at this station.

The next assumption is that air pressure at the time and location of sampling was equal to the air pressure measured at an Environment and Climate Change Canada (ECCC) weather station in Coral Harbour, Southampton Island, NU (64.18 N, 83.35 W), adjusted for elevation. The pressure readings are available at hourly resolution from ECCC (ECCC – MSC, 2022). The pressure was measured at an elevation of 57.00 m above mean sea level, thus it had to be corrected to sea level pressure using the barometric formula (Eq. 28):

$$P = P_h\left[\frac{T_h + (h - h_h)L_h}{T_h}\right]^{\frac{-gM}{RL_h}} \quad \text{Eq. 28}$$

where P is calculated pressure at sea level (in Pa), P_h is measured pressure at altitude (in Pa), T_h is measured temperature at altitude (in K), L_h is temperature lapse rate at altitude (-0.0065 K/m), h is height at which pressure is to be calculated (i.e., sea level, 0 m), h_h is height at altitude (i.e., 57.00 m), g is gravitational acceleration (9.80665 m/s^2), M is molar mass of Earth's air (0.0289644 kg/mol), and R is the gas constant (8.3144598 J/(mol·K)).

Using pH_2O and P calculated using Eq. 27 and Eq. 28, respectively, atmospheric pCO_2 could be calculated using Eq. 29 (Pierrot et al., 2009):

$$pCO_2 = xCO_2(P - pH_2O) \quad \text{Eq. 29}$$

where pCO_2 is atmospheric pCO_2 (in µatm), xCO_2 is the dry mole fraction of CO_2 in the atmosphere (in µmol/mol), P is atmospheric pressure (in atm), and pH_2O is water vapour pressure (in atm). Dry mole fraction of CO_2 in the atmosphere was measured at an hourly resolution at an ECCC site in Churchill, Manitoba (site location was 58.737902 N, 93.820581 W). The altitude of air sample collection was 89 m above sea level. Data are available through the World Data Centre for Greenhouse Gases (ECCC, 2021).

Seawater pCO_2 percent saturation can then be calculated using Eq. 30.

$$pCO_2 \text{ Saturation } (\%) = \left(\frac{\text{Measured seawater } pCO_2}{\text{Atmospheric } pCO_2}\right) \cdot 100 \quad \text{Eq. 30}$$

pCO_2 percent saturation could only be calculated for surface samples as it is unknown what atmospheric pCO_2 values were at the time when deeper waters were last in contact with the atmosphere.

3.8 Calculations Involving Stable Carbon Isotopic Composition of Dissolved Inorganic Carbon

The estimated rate of change in $\delta^{13}C_{DIC}$ from respiratory DIC inputs $\left(\frac{\varepsilon^{13}C_{plant-DIC}}{DIC_{mean}}\right)$ and the photosynthetic fractionation of stable carbon isotopes by marine primary producers ($\varepsilon^{13}C_{plant-DIC}$) in this study region were determined using $\delta^{13}C_{DIC}$, PO_4^{3-}, and DIC data, Redfield C:P ratio of organic matter (106:1; Redfield et al., 1963), and Eq. 18.

DIC_{mix} and $\delta^{13}C_{mix}$ represent DIC and $\delta^{13}C_{DIC}$ expected from conservative mixing of source seawater, river water (RW), and SIM. DIC_{mix} and $\delta^{13}C_{mix}$ were estimated using Eq. 31 and Eq. 32, respectively:

$$DIC_{mix} = DIC_{RW}f_{RW} + DIC_{SIM}f_{SIM} + DIC_{SW}f_{SW} \quad \text{Eq. 31}$$

$$\delta^{13}C_{mix} = \frac{DIC_{RW}\delta^{13}C_{RW}f_{RW} + DIC_{SIM}\delta^{13}C_{SIM}f_{SIM} + DIC_{SW}\delta^{13}C_{SW}f_{SW}}{DIC_{RW}f_{RW} + DIC_{SIM}f_{SIM} + DIC_{SW}f_{SW}} \quad \text{Eq. 32}$$

For f_{RW}, f_{SIM}, and f_{SW}, fractions of MW (in lieu of RW), SIM, and SW calculated using salinity and $\delta^{18}O$ data were used (see Sections 3.5 and 4.2). Determination of DIC_{SW} and $\delta^{13}C_{SW}$ is described in Section 4.2. DIC_{RW} was set to 1433 µmol kg^{-1} (average value for the Hayes, Nelson, Winisk, and Churchill Rivers) and DIC_{SIM} was set to 330 µmol kg^{-1}, as per an unpublished 2018 BaySys Project dataset.

Hayes, Nelson, Winisk, and Churchill Rivers had $\delta^{13}C_{DIC}$ values of -6.53‰, -5.98‰, -6.65‰, -7.38‰, respectively, as per an unpublished 2018 BaySys Project dataset. These river samples were collected between June 18 and 28, 2018. The annual discharge rates for the Hayes, Nelson, Winisk, and Churchill Rivers have been reported as 18.62 km^3 yr^{-1}, 94.24 km^3 yr^{-1}, 14.69 km^3 yr^{-1}, and 20.57 km^3 yr^{-1} (Déry et al., 2005). A flow-weighted average for the four rivers gave $\delta^{13}C_{RW}$ of -6.31‰.

$\delta^{13}C_{SIM}$ was set to 0.54‰, which was the average value of 5 samples from 2 ice cores from an unpublished 2018 BaySys Project dataset. The two ice cores were collected on June 3 and 4, 2018, one in Foxe Channel near Hudson Strait (64.22°N, 78.62°W) and another in NE Hudson Bay near Hudson Strait (62.24°N, 78.72°W). Data from the bottom 5 cm of the ice cores was not included in the $\delta^{13}C_{SIM}$ average as the values were significantly more depleted in the bottom 5 cm than in the rest of the ice core.

Deviations of the sample DIC and $\delta^{13}C_{DIC}$ values from those expected from conservative mixing can be quantified using Eq. 33 and Eq. 34, respectively (Erlenkeuser et al., 2003; Alling et al., 2012):

$$\Delta DIC = \frac{DIC_{sample} - DIC_{mix}}{DIC_{mix}} \quad \text{Eq. 33}$$

$$\Delta\delta^{13}C_{DIC} = \delta^{13}C_{sample} - \delta^{13}C_{mix} \quad \text{Eq. 34}$$

Vectors for various processes creating deviations in the sample DIC and $\delta^{13}C_{DIC}$ from conservative mixing values can be visualized on a plot of $\Delta\delta^{13}C_{DIC}$ versus ΔDIC. In order to estimate a vector for outgassing of CO_2, the approach of Alling et al. (2012) was taken. First, the $\delta^{13}C$ of $CO_{2(aq)}$ in seawater was estimated from $\delta^{13}C_{DIC}$ as follows (Rau et al., 1996):

$$\delta^{13}C_{CO_2} = \delta^{13}C_{DIC} + 23.644 - \frac{9701.5}{T} \quad \text{Eq. 35}$$

where T is the sample temperature in Kelvin and $\delta^{13}C_{DIC}$ is assumed to approximate $\delta^{13}C_{HCO_3^-}$.

Continuing the assumption that $\delta^{13}C_{DIC} \approx \delta^{13}C_{HCO_3^-}$, the difference fractionation factor (ε) between $CO_{2(aq)}$ and HCO_3^- could then be estimated as:

$$\varepsilon_{CO_2} = \delta^{13}C_{CO_2} - \delta^{13}C_{DIC} \quad \text{Eq. 36}$$

The difference fractionation factor allows for an estimation of the fractionation factor, α, as follows (Emerson and Hedges, 2008):

$$\varepsilon \approx 1000 \cdot \ln \alpha \approx 1000 \cdot (\alpha - 1) \quad \text{Eq. 37}$$

Lastly, as per Alling et al. (2012), the equation for the CO_2 outgassing vector is given as:

$$\Delta\delta^{13}C_{DIC} \approx \Delta DIC(\alpha_{CO_2} - 1) \cdot 1000 \quad \text{Eq. 38}$$

This approach assumes that the transfer of CO_2 is from seawater to the atmosphere (i.e., unidirectional), and that outgassing results in a small loss of DIC so that the final DIC concentration divided by the DIC concentration expected from conservative mixing is close to unity (i.e., $DIC_{final}/DIC_{mix} \approx 1$).

$CaCO_3$ dissolution vector could be determined as follows (Alling et al., 2012):

$$\Delta\delta^{13}C \approx \Delta DIC \cdot (\delta^{13}C_{CaCO_3} - \delta^{13}C_{mix}) \quad \text{Eq. 39}$$

3.9 Statistical Analysis

Certain figures in this thesis were made using Ocean Data View (ODV, Schlitzer, 2021). Several R packages were used in the processing, analysis, and visualization of the data (Grolemund and Wickham, 2011; Wickham, 2016, 2019; Wickham et al., 2019; Wickham and Bryan, 2019; Hester and Wickham, 2020; Müller, 2020; Pedersen, 2020; Firke, 2021; Kelley and Richards, 2021).

Chapter 4: Results

4.1 Ice, Salinity and Temperature Distributions

Figure 9 shows the distribution of ice around Southampton Island from June 6 until August 22, 2019, captured by satellite imagery (NASA, n.d.). Roes Welcome Sound and the straits south of the Island had been mostly ice free from the beginning of July, whereas a considerable quantity of ice remained northeast of the Island until the beginning of August.

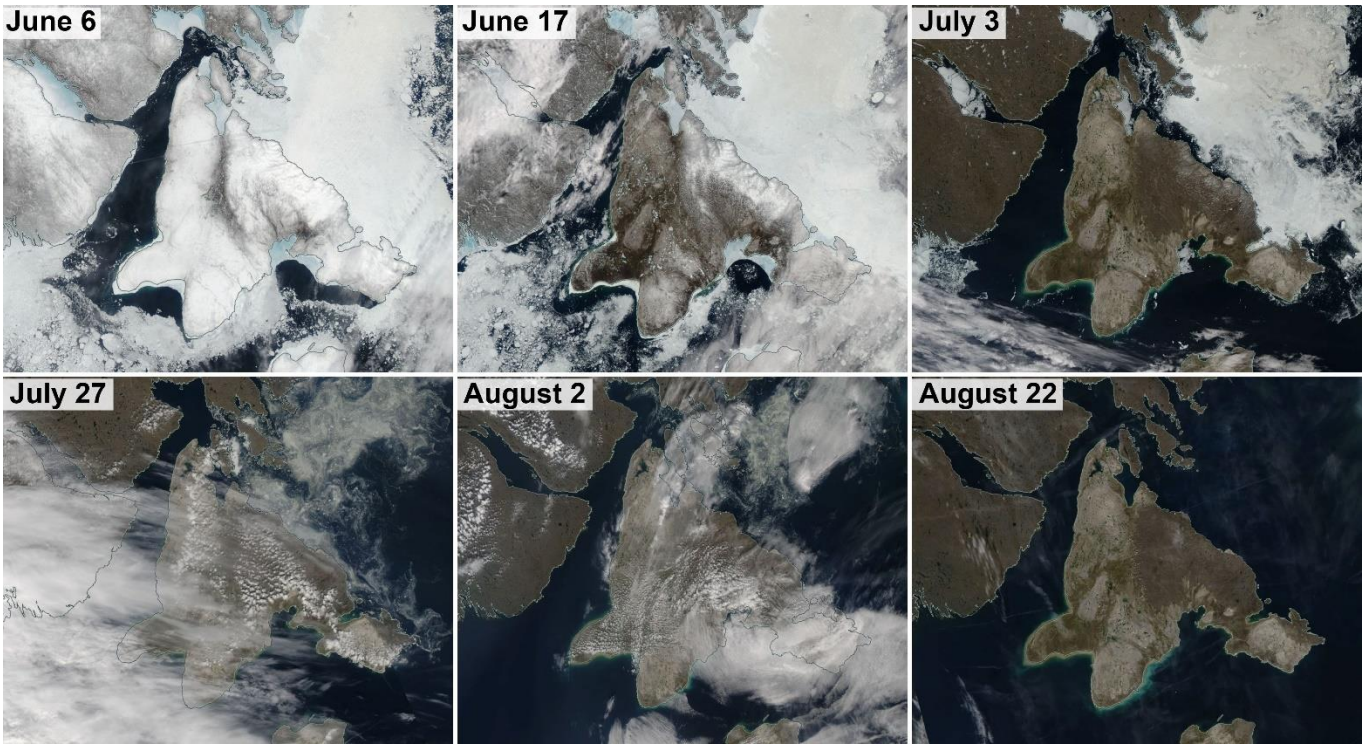

Figure 9. Satellite images from 2019 of Southampton Island, Nunavut. Images taken from NASA, n.d. © 2013 - 2023 United States Government as represented by the Administrator of the National Aeronautics and Space Administration.

Figures 10 and 11 show surface distributions of bottle salinity and downcast CTD temperature, respectively. Highest surface salinities were found north and southeast of the Island (Station 12 at the northern end of Roes Welcome Sound, salinity = 31.97; Station 14 in Frozen Strait, salinity = 31.74; Station 13 in Repulse Bay, salinity = 31.05; Station 21 near Evans Strait, salinity = 30.86; Station 20 near Foxe Channel, salinity = 30.68). These areas generally had lower temperatures, with the lowest surface temperature (1.00°C) measured at Station 14 in Frozen Strait. High salinity waters were also found near the outflow of Wager Bay (Station 11,

salinity = 30.56), however, these waters were warmer (7.08°C). The sample with the lowest salinity value (27.95) was collected at the surface of Station 17 near Foxe Basin but whereas these surface waters were fresh and cool (3.20°C), other low salinity surface waters that surrounded the southern half of the Island were fresh and warm. These surface water characteristics span from Station 9 southeastward to Station 22, with highest surface temperatures recorded at Station 25 near South Bay (9.43°C) and at Station 7 near the entrance to northwest Hudson Bay (8.73°C). As shown in Figure 9, the region from Roes Welcome Sound southeastward to Evans Strait was ice-free since early July, allowing surface waters to gain heat.

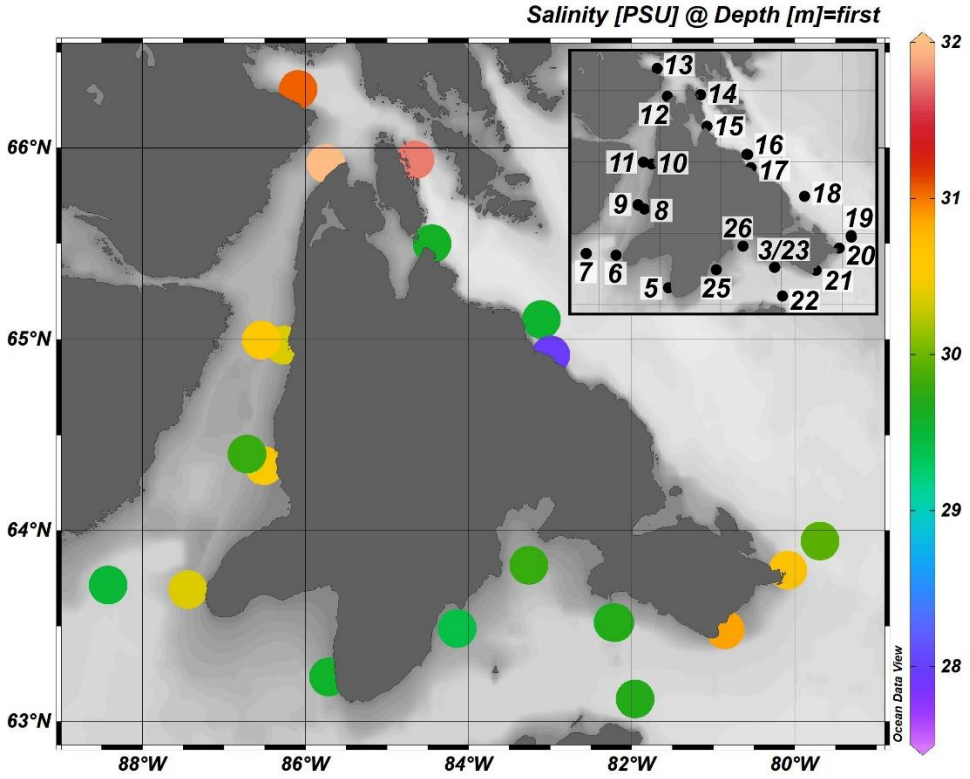

Figure 10. Bottle salinity values at the surface (sample depth <5 m). Inset shows station IDs.

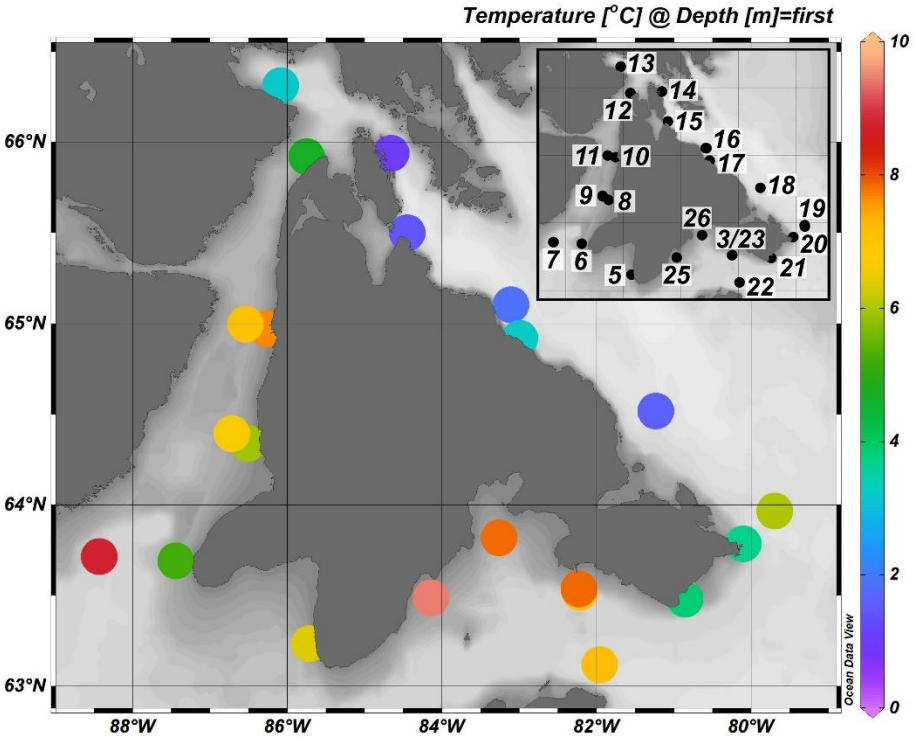

Figure 11. Surface plot of downcast rosette CTD temperatures (measurement depth = 5 m). For stations with multiple rosette casts, only data from the first downcast were used (except Stations 11 and 12 where the second downcasts were used).

Figure 12 shows section plots of depth profiles of bottle salinity and downcast rosette CTD temperature values. Coldest deep waters were observed at Station 19, the station located furthest to the east in Foxe Channel. The cold water mass came up higher in the water column at Station 19 than at similarly deep stations (14, 16, 18). The sample with the greatest salinity (33.29) and lowest θ (-1.76°C) was collected at Station 19 in Foxe Channel, at a depth of 295.1 m. High salinity, low temperature waters were also present below ~30 m at Station 7 near the entrance to northwest Hudson Bay, near the bottom of Stations 9 and 11 in Roes Welcome Sound, below ~20 m on the Foxe Basin/Channel side of the Island, below ~60 m at Station 22 near Coats Island, and below ~30 m in South Bay. All stations seem to have undergone surface freshening and/or warming, and the water column appears stratified.

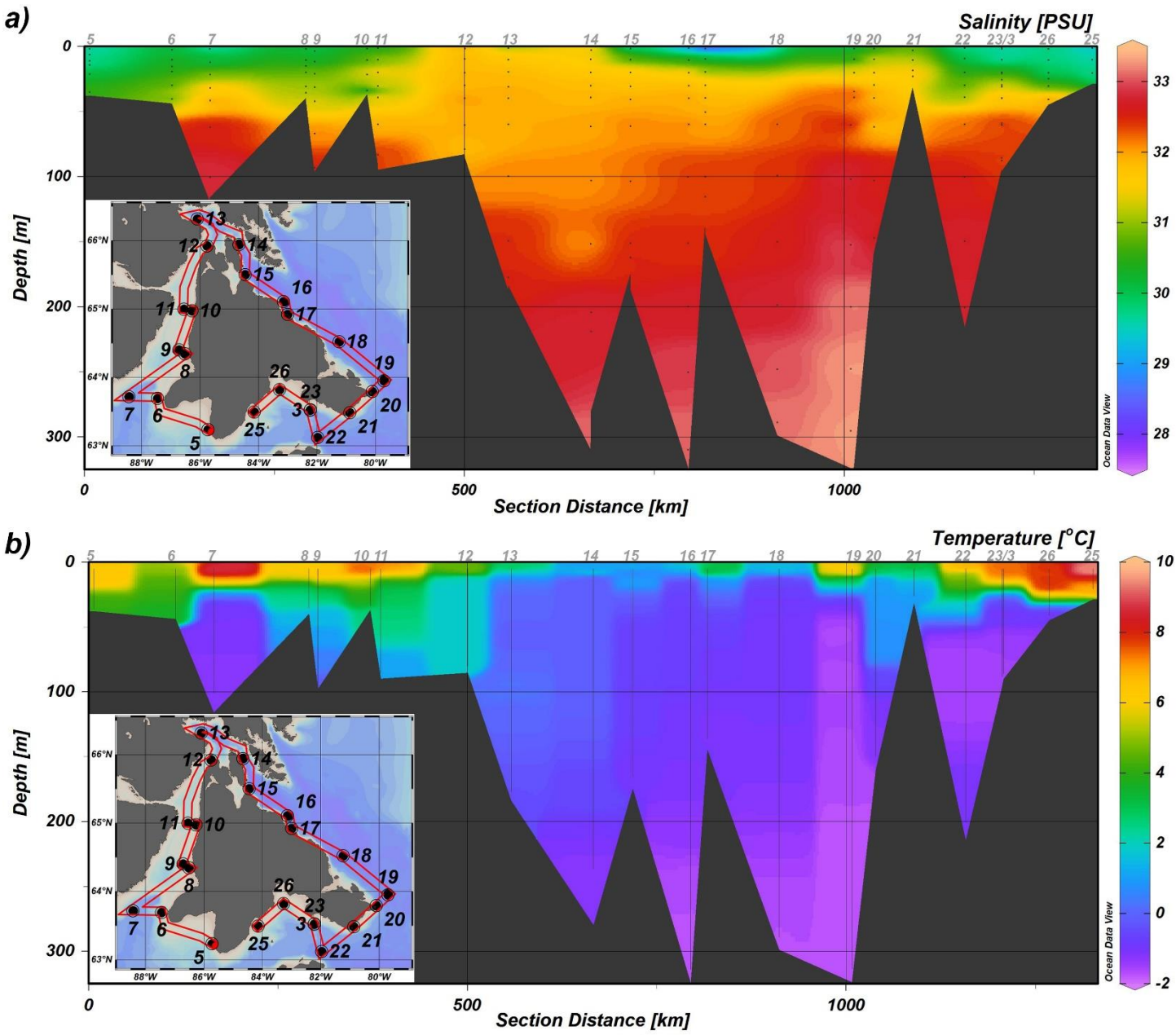

Figure 12. Section plots of a) bottle salinity and b) downcast rosette CTD temperature values. For panel a, where other water samples were collected but bottle salinity values were missing, the missing values (n = 7/160) were replaced with CTD salinity from the upcast rosette bottle files. For panel b, data from the top 5 m of all casts were removed. For stations with multiple rosette casts, only data from the first downcast were used (except Stations 11 and 12 where the second downcasts were used). Station IDs are provided above the panels in gray.

In a plot of θ versus bottle salinity (Figure 13, panel b), most samples fall along the same salinity – θ mixing line between a cold, high salinity water mass and a warm, low salinity water mass.

However, samples from Stations 16 and 17 (Foxe Basin) fall along a different, shallower line (green points in Figure 13) reflecting low temperatures in the fresh water mass. Samples from Station 15 (square points in Figure 13) in Frozen Strait do not fall on either line as θ increased with depth in the first 30 m of the column, with the θ at 19.9 m (1.79°C) greater than the θ at 10.1 m (1.75°C), which in turn was greater than the θ at 1.7 m (1.35°C), while salinity followed the normal pattern of being fresher at the surface (29.58) and increasing with depth (31.71). Lower temperature and lower salinity at the surface of Station 15 indicate the presence of recent ice melt that has not yet warmed.

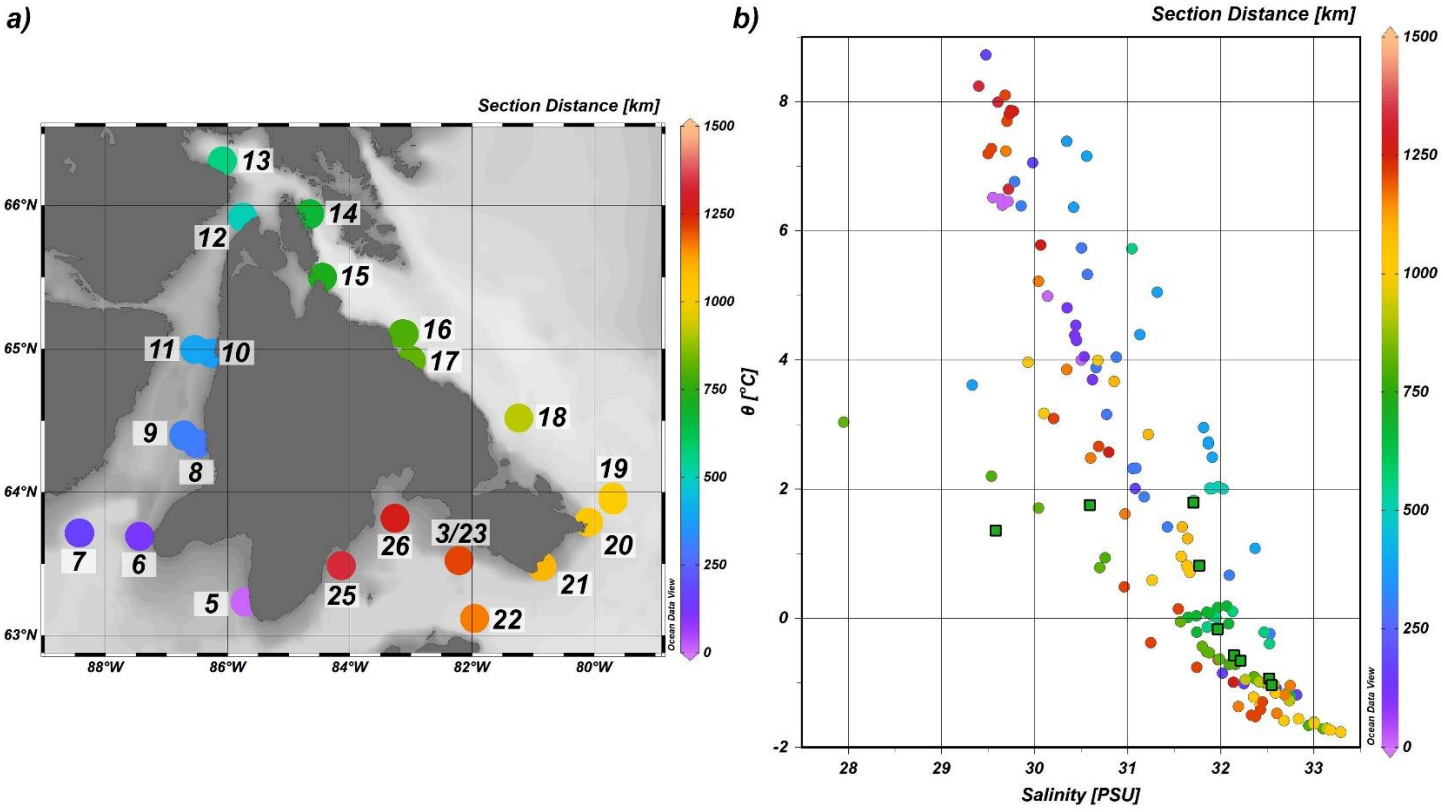

Figure 13. Plot of upcast potential temperatures (θ) versus bottle salinities, with colour representing section distance in both the map (a) and plot (b). Where other water samples were collected but bottle salinity values were missing, the missing values (n = 7/160) were replaced with CTD salinity from the upcast rosette bottle files. Square points in panel b denote samples from Station 15.

4.2 $\delta^{18}O$ Distribution and Relationships with Salinity and Temperature

Surface values of stable oxygen isotope composition of seawater (shown as $\delta^{18}O$) ranged from -3.12‰ (Station 22 near Coats Island) to -2.03‰ (Station 17 near Foxe Basin). As seen in Figure 14, surface waters west (Station 6 – 11) and south (Stations 3, 5, 22 – 26) of the Island were more depleted in the heavy ^{18}O isotope than surface waters on the Foxe Basin/Channel side of the Island.

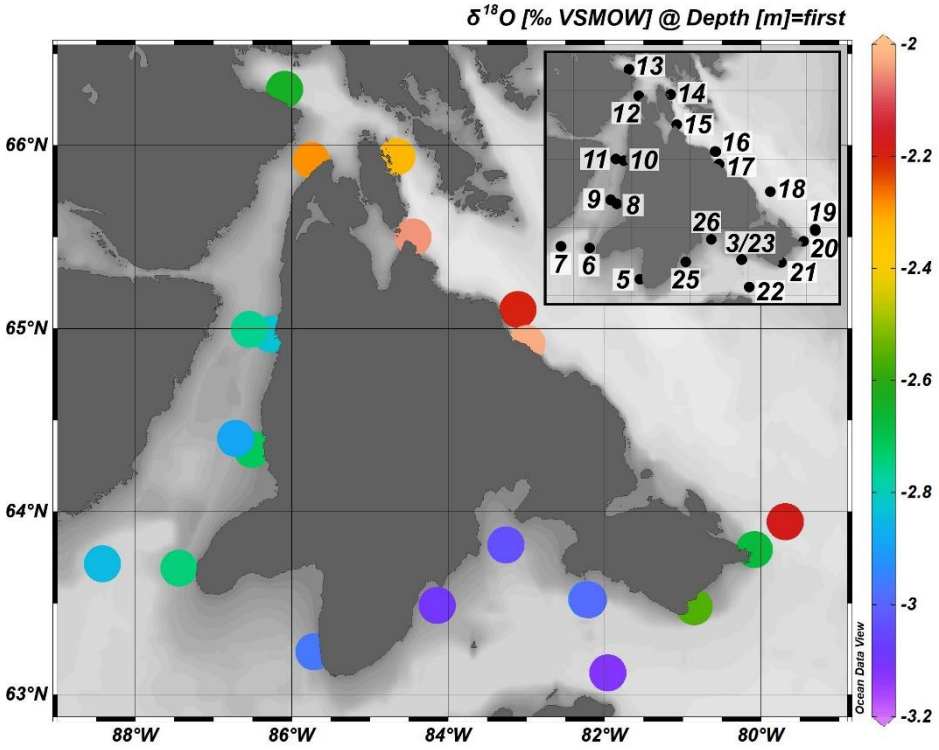

Figure 14. Stable oxygen isotope ratio ($\delta^{18}O$) of surface seawater samples (sample depth <5 m). Inset shows station IDs.

Figure 15 shows the distribution of $\delta^{18}O$ through the whole water column. The most ^{18}O-depleted waters ($\delta^{18}O$ = -3.17‰) were found at 10.9 m of Station 5 near Bay of Gods Mercy. ^{18}O-depleted waters were generally found in the top ~50 m of the water column to the south and west of the Island. The most ^{18}O-enriched waters were found near the bottom of Station 22 near Coats Island, with the highest value of $\delta^{18}O$ (-1.74‰) being found at 200.6 m depth. At similar depths (147.0 – 204.3 m) across other stations (13-16, 18-20), $\delta^{18}O$ was more depleted at -2.27±0.05‰ (mean ± standard deviation, n = 13).

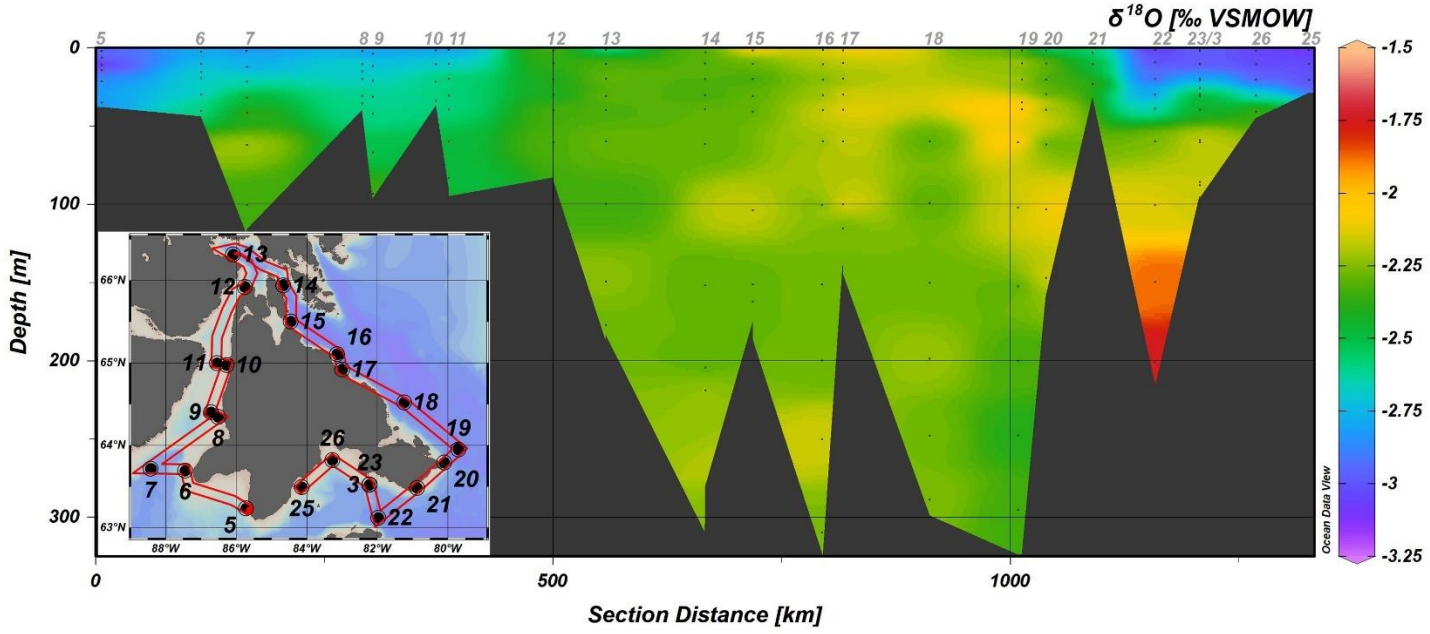

Figure 15. Section plot of stable oxygen isotope ratios ($\delta^{18}O$) of seawater. Station IDs are provided above the panel in gray.

In order to estimate the SW end-member parameters, an average was taken of all values between 50 and 155 m depth (effective depth range: 50.3 – 150.8 m) from Stations 15-18. These stations were chosen assuming they receive source seawater from the current flowing from the Canadian Arctic Archipelago (see Figure 2). Data above 50 m and below 155 m were excluded to avoid freshwater and brine signals, respectively. Station 14 was excluded due to the constricted waterway of Frozen Strait promoting water column mixing, and Station 19 was excluded as it showed more negative values of ΔTA than Stations 15-18, possibly indicating a bigger presence of Atlantic-influenced water from Hudson Strait or brine at Station 19. As a result, the calculated SW end-member had the following parameters (values are presented as mean ± standard deviation): salinity of 32.3±0.2 (n = 13), $\delta^{18}O$ of -2.2±0.1‰ (n = 11), DIC of 2155.40±23.71 µmol kg^{-1} (n = 13), and $\delta^{13}C_{DIC}$ of 0.61±0.11‰ (n = 9; note that $\delta^{13}C_{DIC}$ data were missing for Station 17). The selected SW end-member lies within a dense cluster of samples in plots of $\delta^{18}O$ versus salinity (Figures 16 – 18), although not at the extreme right or top of the plots.

For the apparent MW end-member, a regression line was plotted through salinity – $\delta^{18}O$ points from the top 50 m of the water column (effective depth range: 1.2 – 42.2 m) that had $\delta^{18}O$ more

depleted (i.e., more negative) than -2.3‰. The -2.3‰ upper limit for $\delta^{18}O$ was chosen to omit samples that fell along the apparent SW-SIM mixing line. One apparent outlier (Station 10, depth = 33.7 m, salinity = 29.3, $\delta^{18}O$ = -2.63‰) was excluded from the regression line. The resulting equation of the regression line was $\delta^{18}O = -11.1 + 0.3 \cdot Salinity$ ($R^2 = 0.8570$, n = 74). Assuming salinity of 0, the $\delta^{18}O$ value of the apparent MW end-member was -11.1‰. Although this value lies within the range of river water in Hudson Bay (cf. Granskog et al., 2011; Burt et al., 2016), it is much more enriched than precipitation at the latitude of the sampling sites and thus possibly incorporates a considerable fraction of SIM. In other words, the main freshwater source in the SIMEP study area which is referred to as MW in this work could be a mixture of MW and SIM, preformed within the system before the sampling campaign. Alternatively, the predominant source of meteoric water in the study region could be a mix of Hudson Bay's northwestern rivers (Churchill, Nelson, and Hayes Rivers) which have relatively enriched $\delta^{18}O$ values ranging from -12.71‰ to -10.81‰ (Burt et al., 2016).

This study used the SIM end-member from Ahmed et al. (2020) as determined for Hudson Bay. Values of Ahmed et al. (2020) were determined by averaging salinity and $\delta^{18}O$ of 63 ice-core samples taken across 10 stations within Hudson Bay during the BaySys spring – early summer cruise. Table 5 provides a summary of end-member values used in the mixing model in this study.

Table 5. End-member values used to calculate fractions of seawater, sea-ice melt, and meteoric water in the samples in this study.

Water Mass	Salinity	$\delta^{18}O$-H_2O (‰)	Reference
Seawater	32.3±0.2	-2.2±0.1	This study
Sea-ice melt	1.4±0.5	-0.8±0.2	Ahmed et al. (2020)
Meteoric water	0	-11.1	This study

In Figures 16 – 18, $\delta^{18}O$ is plotted against salinity, with colour representing water depth in Figure 16, θ in Figure 17, and section distance in Figure 18. SW – SIM and SW – MW mixing lines are shown in each figure, according to the SW, SIM, and MW end-members outlined in Table 5. As seen in Figure 16, the majority of <~50 m samples fall along the SW-MW mixing line, and some fall along the SW-SIM mixing line. Points that do not fall along either of the two mixing lines tend to be deep-water samples.

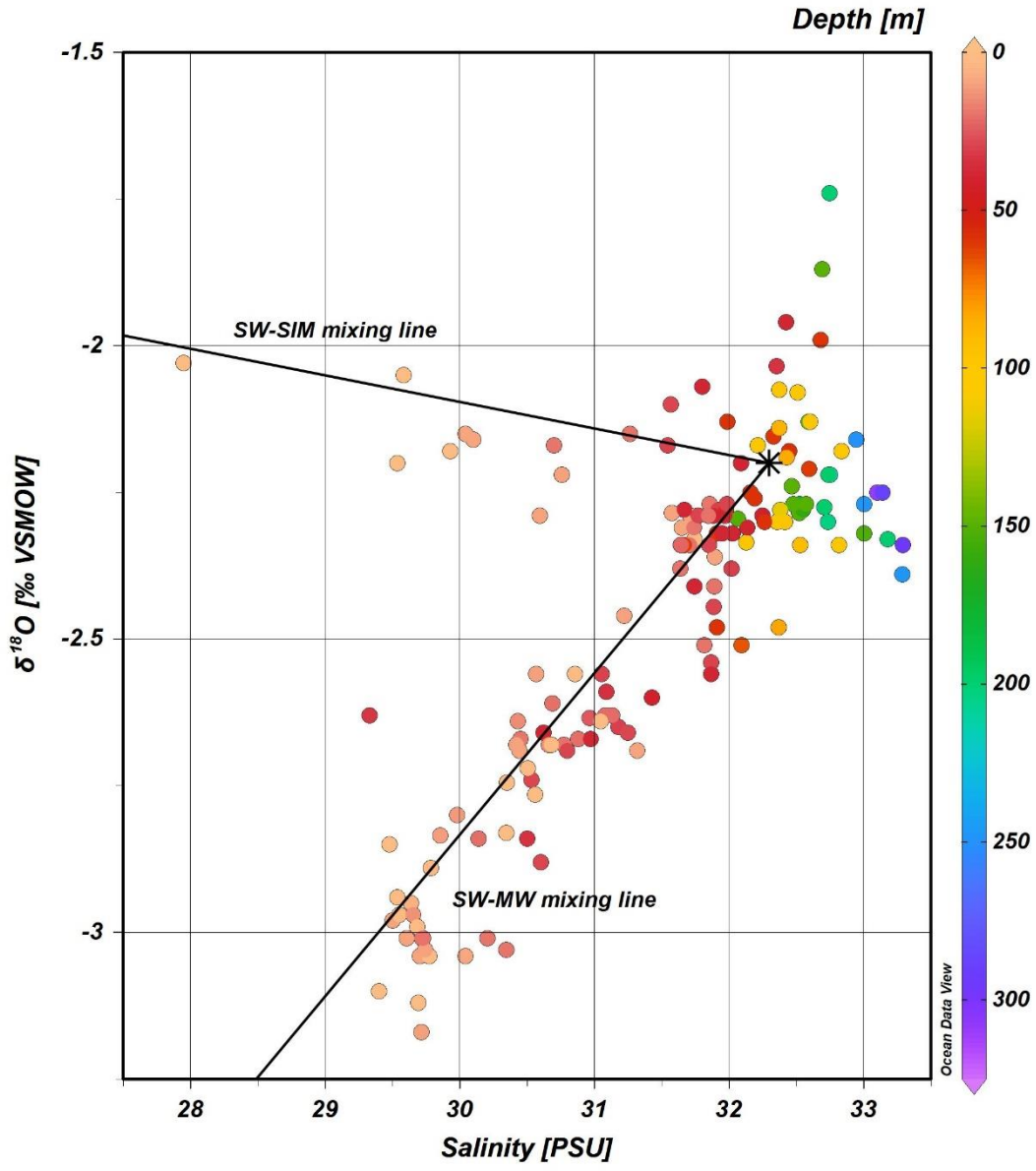

Figure 16. Stable oxygen isotope ratios ($\delta^{18}O$) of seawater plotted against salinity, with colour representing depth of the sample. Salinity values are bottle salinities (except when bottle salinities were missing, CTD salinity values from upcast rosette bottle files were used). Asterisk marks the seawater (SW) end-member values (32.3 PSU, -2.2‰). The mixing lines connect the SW end-member with sea-ice meltwater (SIM; 1.4 PSU, -0.8‰; Ahmed et al., 2020) and meteoric water (MW; 0 PSU, -11.1‰) end-member values.

As seen in Figure 17, samples with higher θ (>5°C) were characterized by lower salinity (<31.5) and depletion in ^{18}O (more negative $\delta^{18}O$ values, <-2.5‰), and they fall in proximity to the SW-MW mixing line. In contrast, samples with lower θ values (<1°C) tend to have higher salinity

(>31.5) and more enriched (i.e., less negative) $\delta^{18}O$ values (>-2.5‰). Most samples with lower θ values fall outside of the mixing lines and appear to cluster around the calculated SW end-member (salinity = 32.3, $\delta^{18}O$ = -2.2‰).

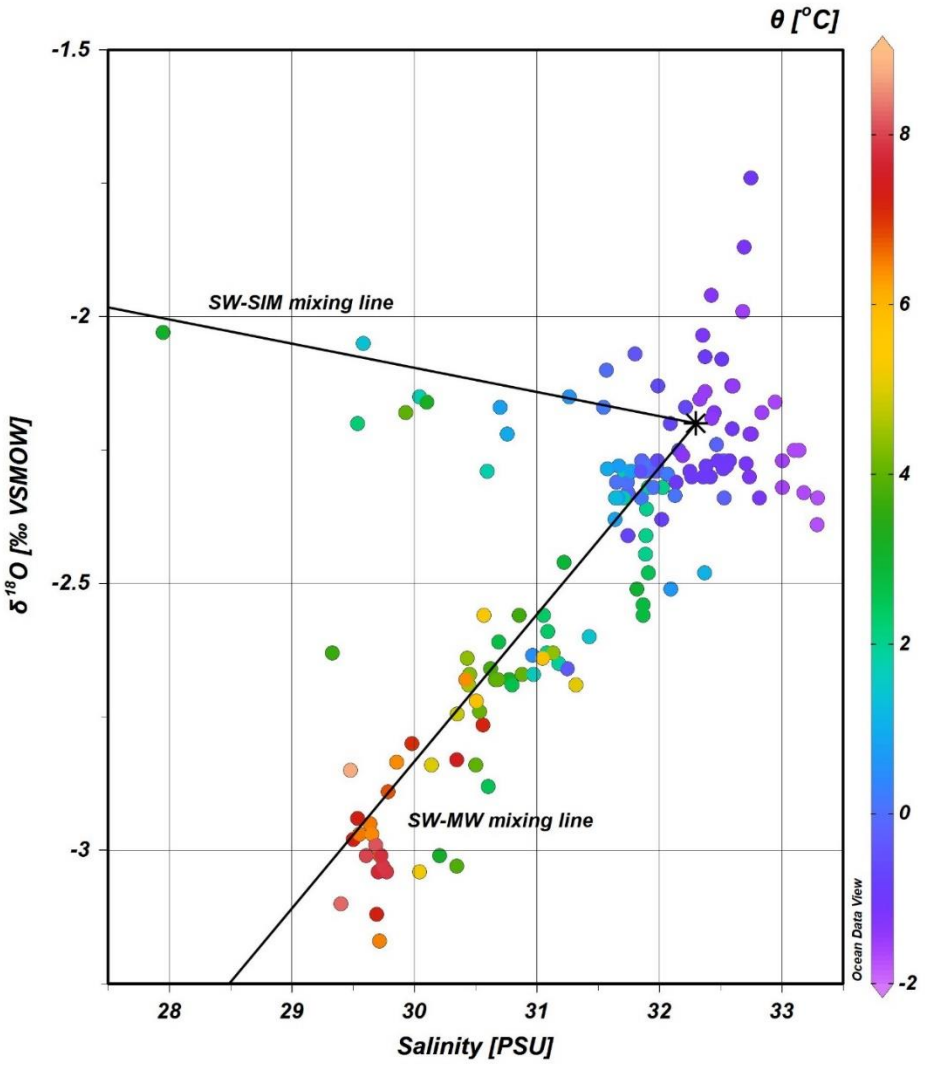

Figure 17. Stable oxygen isotope ratios ($\delta^{18}O$) of seawater plotted against salinity, with colour representing potential temperature (θ) of the sample. Salinity values are bottle salinities (except when bottle salinities were missing, CTD salinity values from upcast rosette bottle files were used). Asterisk marks the seawater (SW) end-member values (32.3 PSU, -2.2‰). The mixing lines connect the SW end-member with sea-ice meltwater (SIM; 1.4 PSU, -0.8‰; Ahmed et al., 2020) and meteoric water (MW; 0 PSU, -11.1‰) end-member values.

As seen in Figure 18, samples collected west and south of the Island (Stations 3-11, 23-26) tend to fall along the SW-MW mixing line, whereas samples from Foxe Basin/Channel to the

northeast of the Island (Stations 15, 16, 17, 19) tend to fall along the SW-SIM mixing line. The two points with the highest $\delta^{18}O$ values (>-1.9‰) belong to bottom samples (sample depths = 149.7 m, 200.6 m) of Station 22 (bottom depth = 215 m) near Coats Island. These two points approach the Hudson Bay SW end-member as defined by Granskog et al. (2011) (salinity = 32.8, $\delta^{18}O$ = -1.5‰) and demonstrate the high degree of variability in waters in the study region.

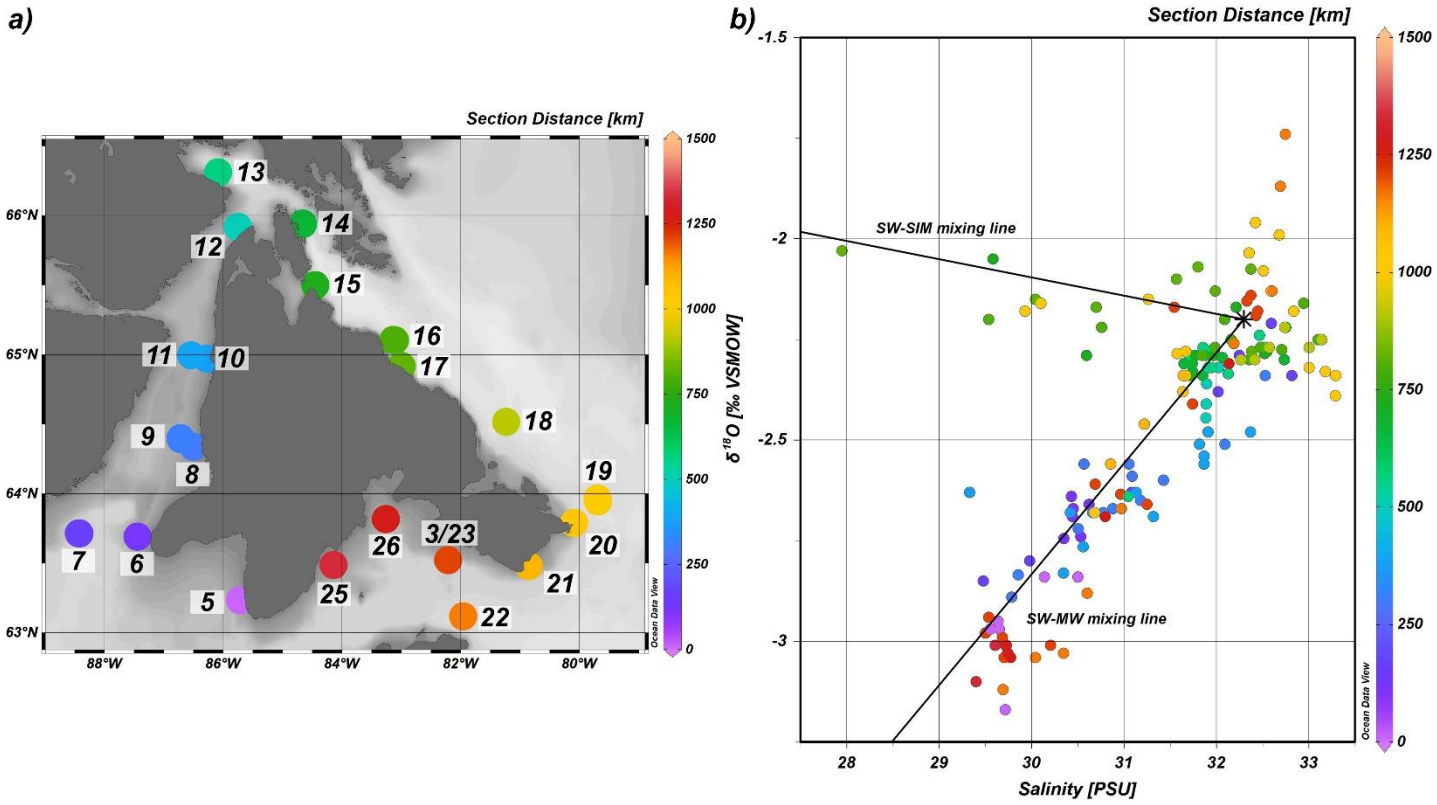

Figure 18. Stable oxygen isotope ratios ($\delta^{18}O$) of seawater plotted against salinity, with colour representing section distance in both the map (a) and plot (b). Salinity values are bottle salinities (except when bottle salinities were missing, CTD salinity values from upcast rosette bottle files were used). Asterisk marks the seawater (SW) end-member values (32.3 PSU, -2.2‰). The mixing lines connect the SW end-member with sea-ice meltwater (SIM; 1.4 PSU, -0.8‰; Ahmed et al., 2020) and meteoric water (MW; 0 PSU, -11.1‰) end-member values.

Using salinity and $\delta^{18}O$ end-member values outlined in Table 5, and a three-end-member mixing model described in Section 2.6.2, f_{SW}, f_{SIM}, and f_{MW} were calculated for each bottle sample. As seen in Figure 19, highest fractions of SIM were observed in surface samples of Stations 17 (f_{SIM} = 0.14, salinity = 27.9, $\delta^{18}O$ = -2.0‰, θ = 3.03°C), 15 (f_{SIM} = 0.091, salinity = 29.6, $\delta^{18}O$ = -

2.1‰, θ = 1.35°C), and 16 (f_{SIM} = 0.077, salinity = 29.5, $\delta^{18}O$ = -2.2‰, θ = 2.20°C). A contour of f_{SIM} = 0 in Figure 19 separates samples with positive f_{SIM} (indication of sea-ice melt) from those with negative f_{SIM} (indication of brine). As seen in Figure 19, most bottom waters and many surface waters around Southampton Island showed a signal of brine. The strongest signal (the most negative f_{SIM}) was found at Station 19 (sample depth = 247.7 m, f_{SIM} = -0.047, salinity = 33.3, $\delta^{18}O$ = -2.4‰, θ = -1.76°C). An unusual pattern was observed at Station 22 near Coats Island, where highest values of f_{SIM} for the station were observed near the bottom (f_{SIM} at 1.3 m = -0.020, f_{SIM} at 149.7 m = 0.022, f_{SIM} at 200.6 m = 0.034). As for the f_{MW}, the greatest values were observed in South Bay (Stations 3, 23-26), near Coats Island (Station 22), Bay of Gods Mercy (Station 5), and Roes Welcome Sound (Stations 6-11). The greatest f_{MW} (0.10) were found at Station 5 (depth = 10.9 m, salinity = 29.7, $\delta^{18}O$ = -3.2‰, θ = 6.45°C), Station 22 (depth = 1.3 m, salinity = 29.7, $\delta^{18}O$ = -3.1‰, θ = 7.23°C), and Station 25 (depth = 1.4 m, salinity = 29.4, $\delta^{18}O$ = -3.1‰, θ = 8.24°C). Negative f_{MW}, which result from the selected end-members not being representative of the particular water sample, were observed at several stations, with the most negative values (down to -0.046) found in the bottom samples of Station 22 and intermediate depth samples of Station 19. The presence of Hudson Bay seawater or Atlantic-influenced seawater from Hudson Strait inflow could explain the unusual distributions of freshwater at Station 22. As stated previously, $\delta^{18}O$ values of near-bottom samples from Station 22 approach the Hudson Bay SW end-member as defined by Granskog et al. (2011). It follows that the end-member values used for calculations of f_{SIM} and f_{MW} may not have been appropriate for Station 22, which would explain the positive f_{SIM} and negative f_{MW} calculated for bottom waters of Station 22.

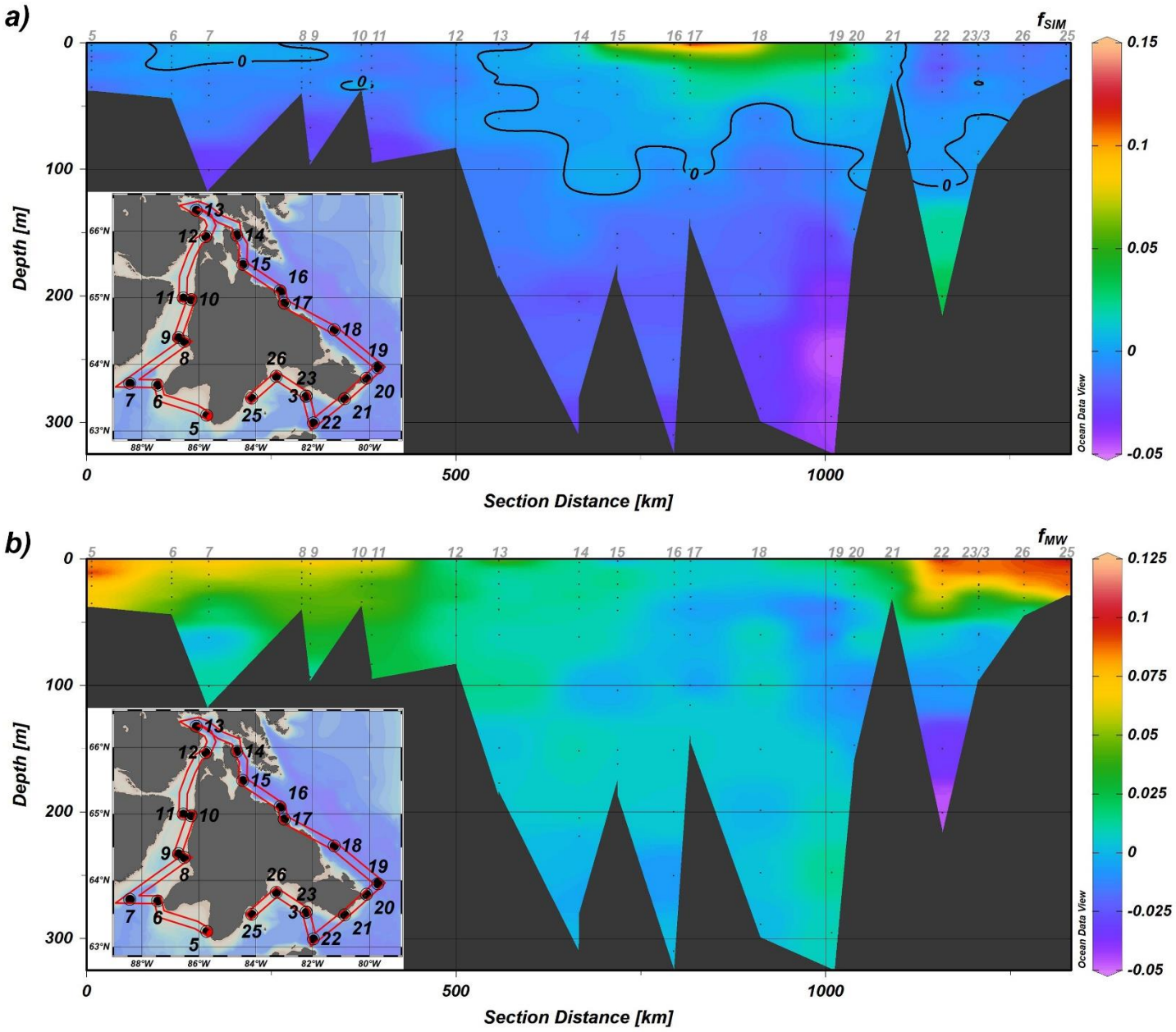

Figure 19. Fractions of a) sea-ice meltwater (f_{SIM}) and b) meteoric water (f_{MW}) calculated using seawater and MW end-member values calculated using data from this study, and SIM end-member values of Ahmed et al. (2020). Station IDs are provided above the panels in gray.

4.3 Nutrient Tracers

In order to get more insight into the influence of different source waters in the region, a plot of NO_3^- + NO_2^- versus PO_4^{3-} was made and Pacific (as per Yamamoto-Kawai et al., 2008), Atlantic and Arctic (as per Azetsu-Scott et al., 2012) lines were added, as shown in Figure 20. Many

water samples fell close to the Arctic line (in between lines defining Arctic and Pacific waters), and most near-surface samples did not fall along either line, instead showing $NO_3^- + NO_2^-$ depletion and varying PO_4^{3-} concentrations. It is important to note that there were no measurements of ammonium (NH_4^+) concentrations made during the cruise. As such, the values presented in Figure 20 could not be corrected for NH_4^+ as was done in the study by Azetsu-Scott et al. (2012). Pacific waters can undergo denitrification (reduction of NO_3^- and NO_2^- to gaseous forms of nitrogen) as they pass over the Arctic shelves and nitrification (conversion of NH_4^+ to NO_3^-) in the Canada Basin, hence including the NH_4^+ concentration together with $NO_3^- + NO_2^-$ accounts for these shelf-water effects as the total dissolved inorganic nitrogen ($NO_3^- + NO_2^- + NH_4^+$) would remain constant during nitrification (Yamamoto-Kawai et al., 2008). Had it been possible to do the NH_4^+ correction on the values presented here, $NO_3^- + NO_2^-$ value would increase for any sample where concentration of NH_4^+ was greater than 0. As such, it is possible that the samples that currently fall somewhere between the Arctic and Pacific lines would have fallen closer to the Arctic line if such a correction could be made.

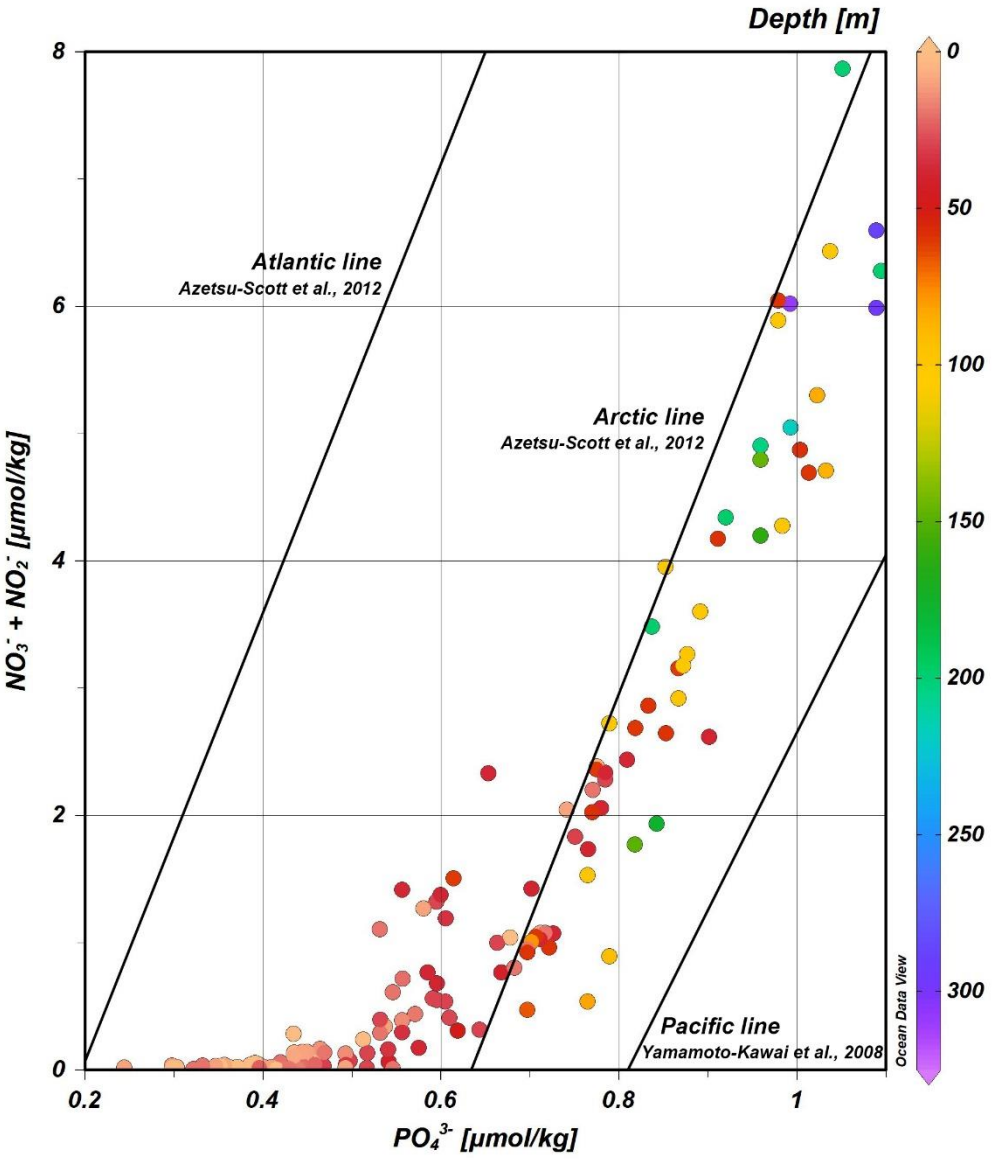

Figure 20. Sum of nitrate and nitrite (NO_3^- + NO_2^-) concentrations versus phosphate (PO_4^{3-}) concentration. Atlantic (NO_3^- + NO_2^- = 17.63· PO_4^{3-} - 3.46; R^2 = 0.93) and Arctic (NO_3^- + NO_2^- = 17.82· PO_4^{3-} - 11.30; R^2 = 0.87) lines are from Azetsu-Scott et al. (2012). Pacific line (NO_3^- + NO_2^- + NH_4^+ = 13.957 · PO_4^{3-} - 11.306; R^2 = 0.96) is from Yamamoto-Kawai et al. (2008).

4.4 Distribution of "Excess" Total Alkalinity

"Excess" total alkalinity (ΔTA) was calculated for the samples relative to a Pacific water end-member (salinity = 32, TA = 2250 µmol kg^{-1}; Jones et al., 2008). ΔTA ranged from -49.9 µmol kg^{-1} (Station 19, depth = 60.2 m) to 44.1 µmol kg^{-1} (Station 22, depth = 9.3 m). The mean of all ΔTA values was -6.1 µmol kg^{-1} (standard deviation = 19.7 µmol kg^{-1}, n = 153). The relatively

low value indicates a stronger Pacific influence. However, as seen in the plots of ΔTA against salinity (Figure 21), there is a pattern where increasing salinity correlates with ΔTA becoming more negative (ΔTA = 451 – 14.5·Salinity; R^2 = 0.6072, n = 153). This suggests that the distribution of ΔTA within the study region may be controlled by presence of freshwater, which lowers salinity and increases ΔTA, and brine, which increases salinity and decreases ΔTA.

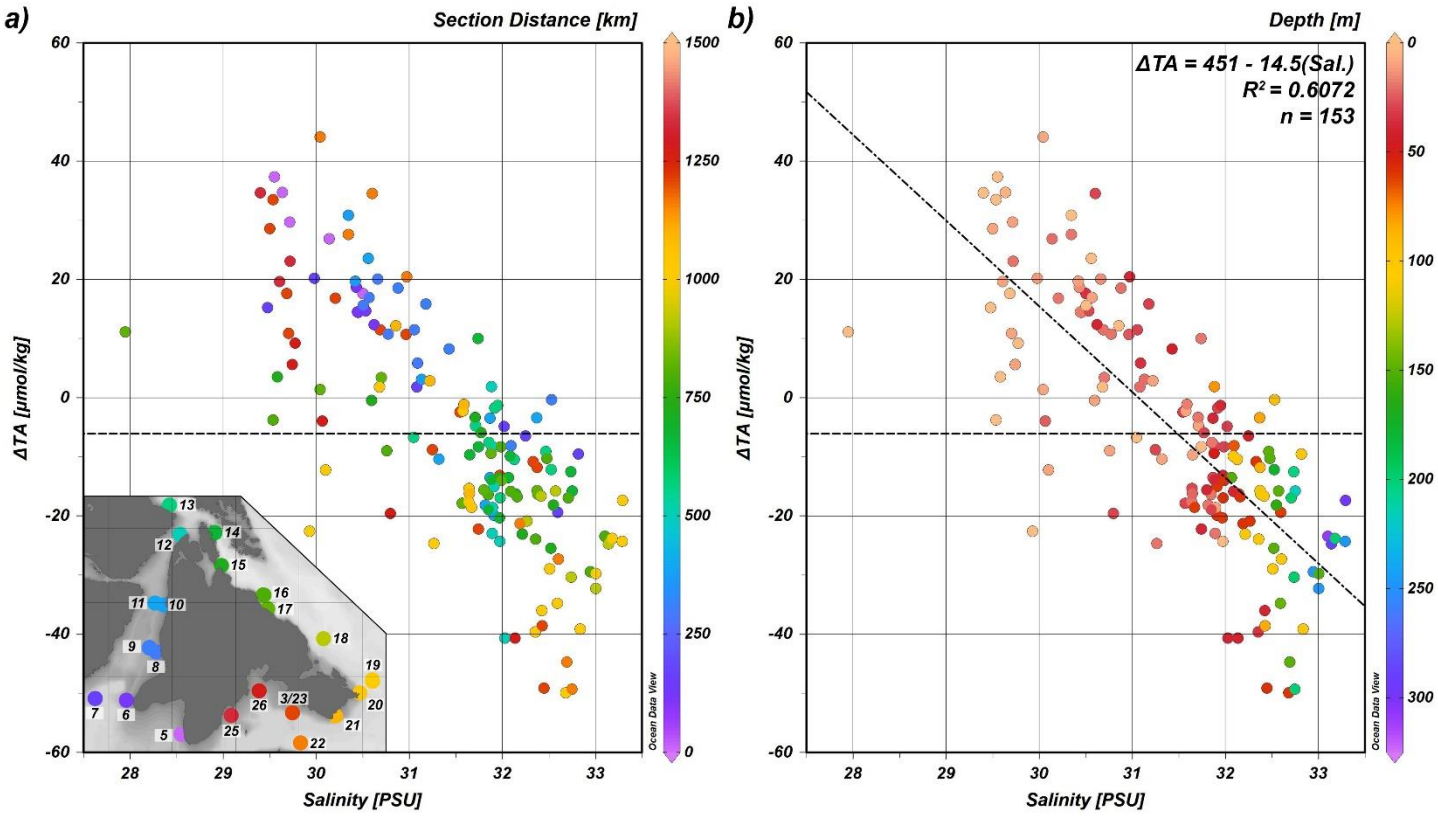

Figure 21. "Excess" total alkalinity (ΔTA) versus salinity for Southampton Island region, with colour representing section distance (a) and depth (b). Inset in plot a shows station IDs. Salinity values are bottle salinities (except when bottle salinities were missing, CTD salinity values from upcast rosette bottle files were used). Dashed horizontal line at ΔTA = -6.1 µmol kg^{-1} denotes the mean value of all samples (standard deviation = 19.7 µmol kg^{-1}; n = 153). Linear regression line, regression equation, and R^2 value are shown in plot b.

Figure 22 shows a section plot of depth profiles of ΔTA values. The most negative ΔTA values were mostly found at depth in South Bay, near Coats Island, and on the Foxe Basin/Channel side of the Island, particularly at Station 19. Positive ΔTA values were mostly found at surface on the south and west sides of the Island.

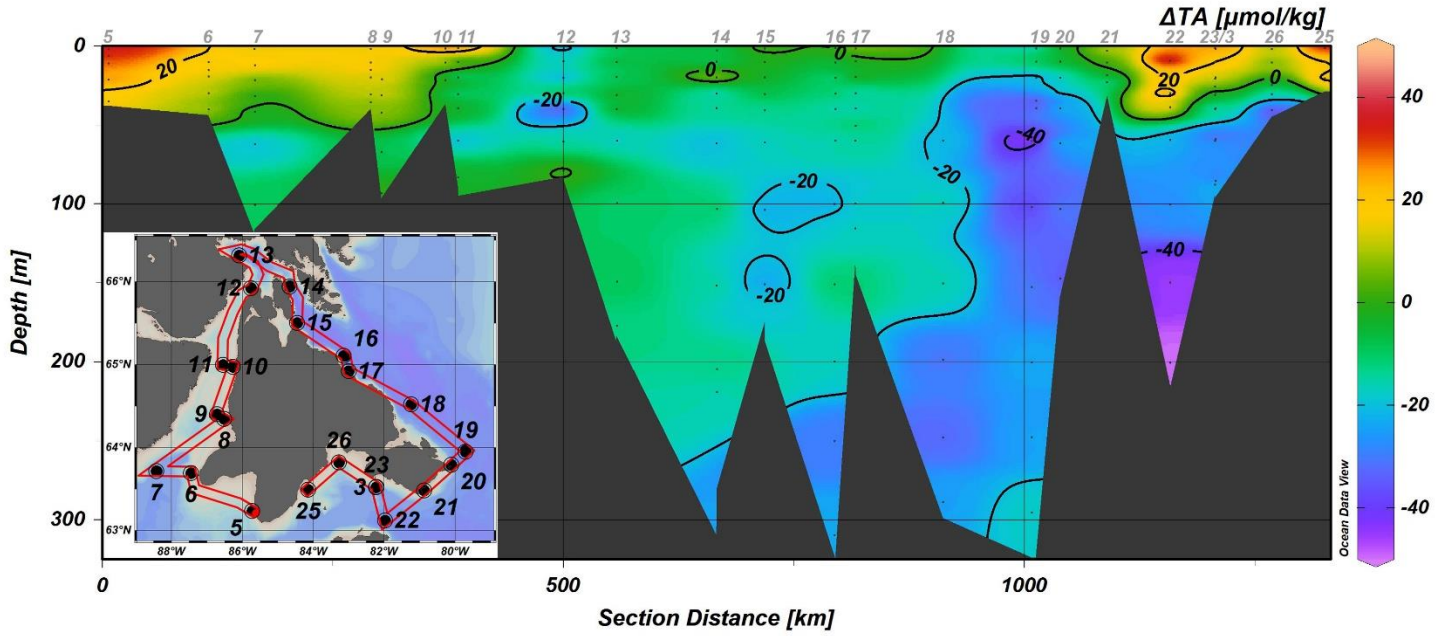

Figure 22. Section plot of "excess" total alkalinity (ΔTA) values. Station IDs are provided above the panel in gray.

4.5 Carbonate System

Observed values of DIC ranged from 1853.63 µmol kg^{-1} (Station 17, depth = 1.5 m) to 2253.23 µmol kg^{-1} (Station 19, depth = 247.7 m). Observed TA values ranged from 1976.25 µmol kg^{-1} (Station 17, depth = 1.5 m) to 2323.39 µmol kg^{-1} (Station 19, depth = 295.1 m). When looking at a plot of surface DIC values (Figure 23), the greatest values were observed north of the Island outside Repulse Bay at Stations 12 (2112.58 µmol kg^{-1}) and 14 (2114.41 µmol kg^{-1}), and the lowest values were observed along Foxe Basin/Channel approaching Hudson Strait (Station 17, DIC = 1853.63 µmol kg^{-1}; Station 19, DIC = 1928.69 µmol kg^{-1}; Station 16, DIC = 1941.57 µmol kg^{-1}).

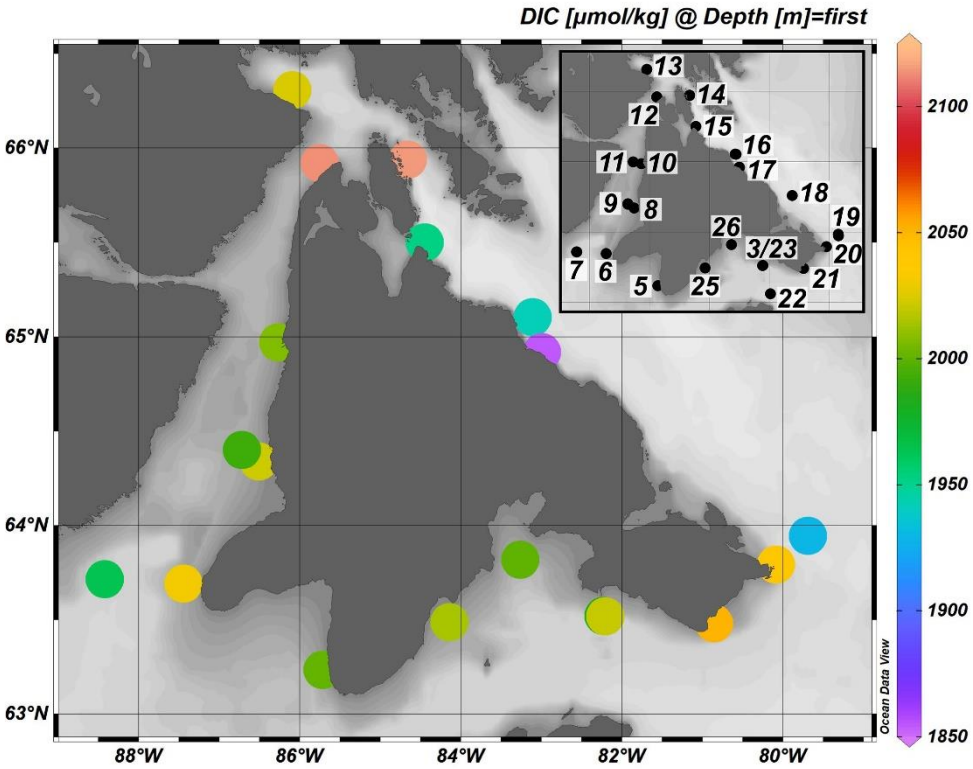

Figure 23. Dissolved inorganic carbon (DIC) values at the surface (sample depth <5 m). Inset shows station IDs.

Surface values of TA show a similar distribution to that of DIC. As seen in Figure 24, greatest surface TA values were seen north of the Island at Stations 12 (2223.84 µmol kg^{-1}) and 14 (2223.62 µmol kg^{-1}). High values were also observed at Station 21 near Evans Strait (2181.74 µmol kg^{-1}), at Station 13 in Repulse Bay (2176.36 µmol kg^{-1}), and at Station 11 near Wager Bay (2172.35 µmol kg^{-1}). Low surface values of TA were seen on the Foxe Basin/Channel side of the Island, with surface TA at Station 17 being 1976.25 µmol kg^{-1} and at Station 16 being 2073.08 µmol kg^{-1}.

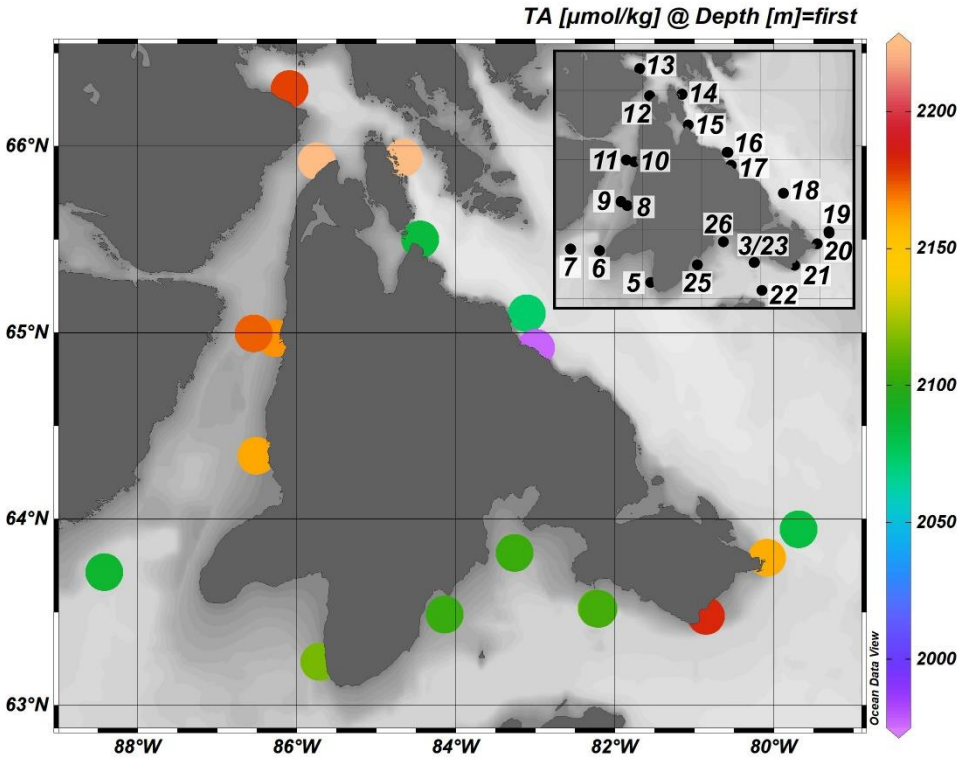

Figure 24. Total alkalinity (TA) values at the surface (sample depth <5 m). Inset shows station IDs.

Figure 25 shows a section plot of depth profiles of DIC and TA values. As seen in the plot, values for DIC and TA were lower at the surface and generally increase with depth across all stations. Particularly low values of DIC and TA were observed at the surface on the Foxe Basin side of the Island. Greatest values of both DIC and TA were observed at depths on the Foxe Channel side of the Island and at depths at the southern exit from Roes Welcome Sound at Station 7.

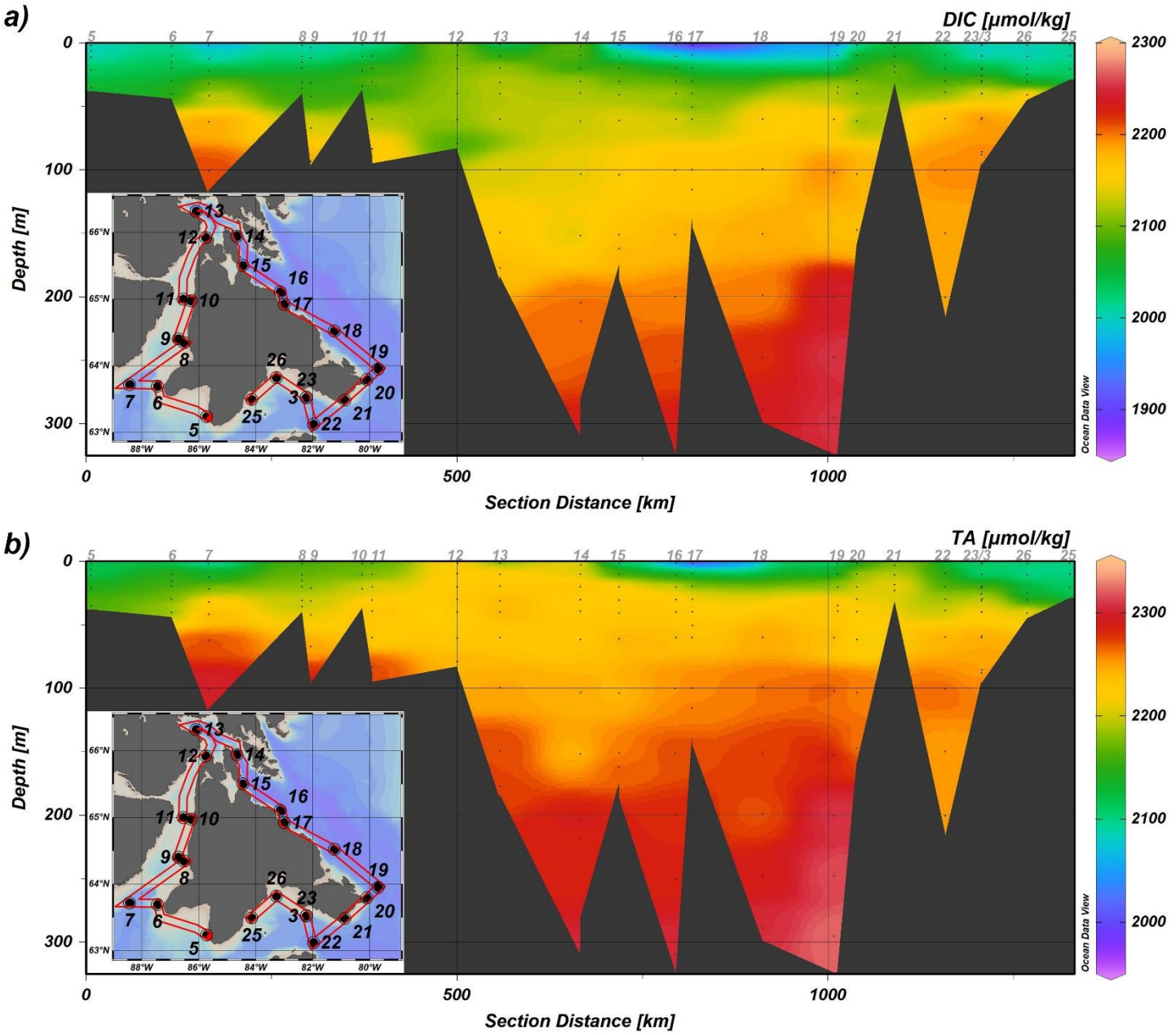

Figure 25. Section plots of a) dissolved inorganic carbon (DIC) and b) total alkalinity (TA) values. Station IDs are provided above the panels in gray.

Neither calcite nor aragonite was undersaturated at surface. Ω_{ar} at the surface ranged from 1.13 (Station 23 in South Bay) to 1.77 (Station 10 in Roes Welcome Sound). As shown in Figure 26, lower values of Ω_{ar} were observed in South Bay and in Frozen Strait, whereas higher values were observed in Roes Welcome Sound near Wager Bay, in Repulse Bay, and in Foxe Channel.

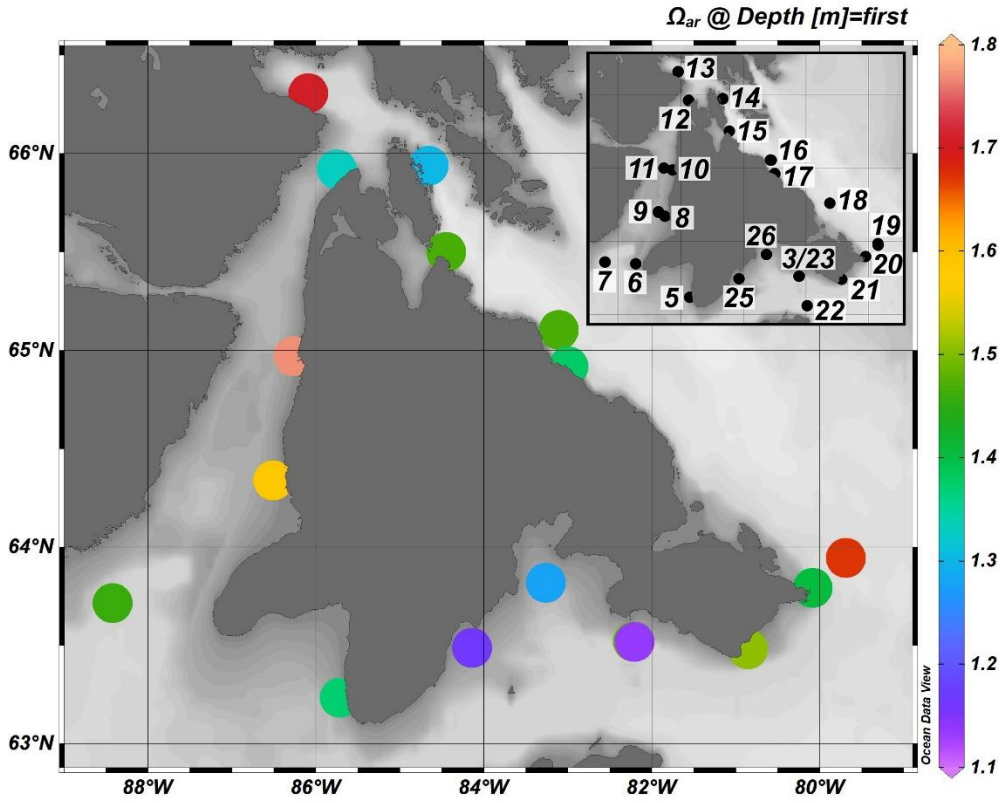

Figure 26. Aragonite saturation state (Ω_{ar}) values at the surface (sample depth <5 m). Inset shows station IDs.

pH ranged from 7.83 (Station 23 in South Bay, depth = 59.0 m) to 8.20 (Station 19 on Foxe Channel side of the Island, depth = 20.0 m). As seen from the section plot of depth profiles of pH (top panel of Figure 27), waters were more acidic south of the Island and at depth east of the Island. Meanwhile surface waters to the east of the Island, near-surface waters in Repulse Bay, and waters at depth at Station 12 at the northern entrance to Roes Welcome Sound all experienced higher values of pH, as seen in Figure 27.

The saturation state for calcite (Ω_{ca}) was above 1 for all samples, with values ranging from 1.25 to 2.86. Saturation state of aragonite (Ω_{ar}) is shown in the bottom panel of Figure 27. Ω_{ar} ranged from 0.78 (Station 23, depth = 59.0 m) to 1.78 (Station 19, depth = 9.9 m). Ω_{ar} fell below 1, indicating conditions potentially corrosive to aragonite, in bottom waters east and south of the Island.

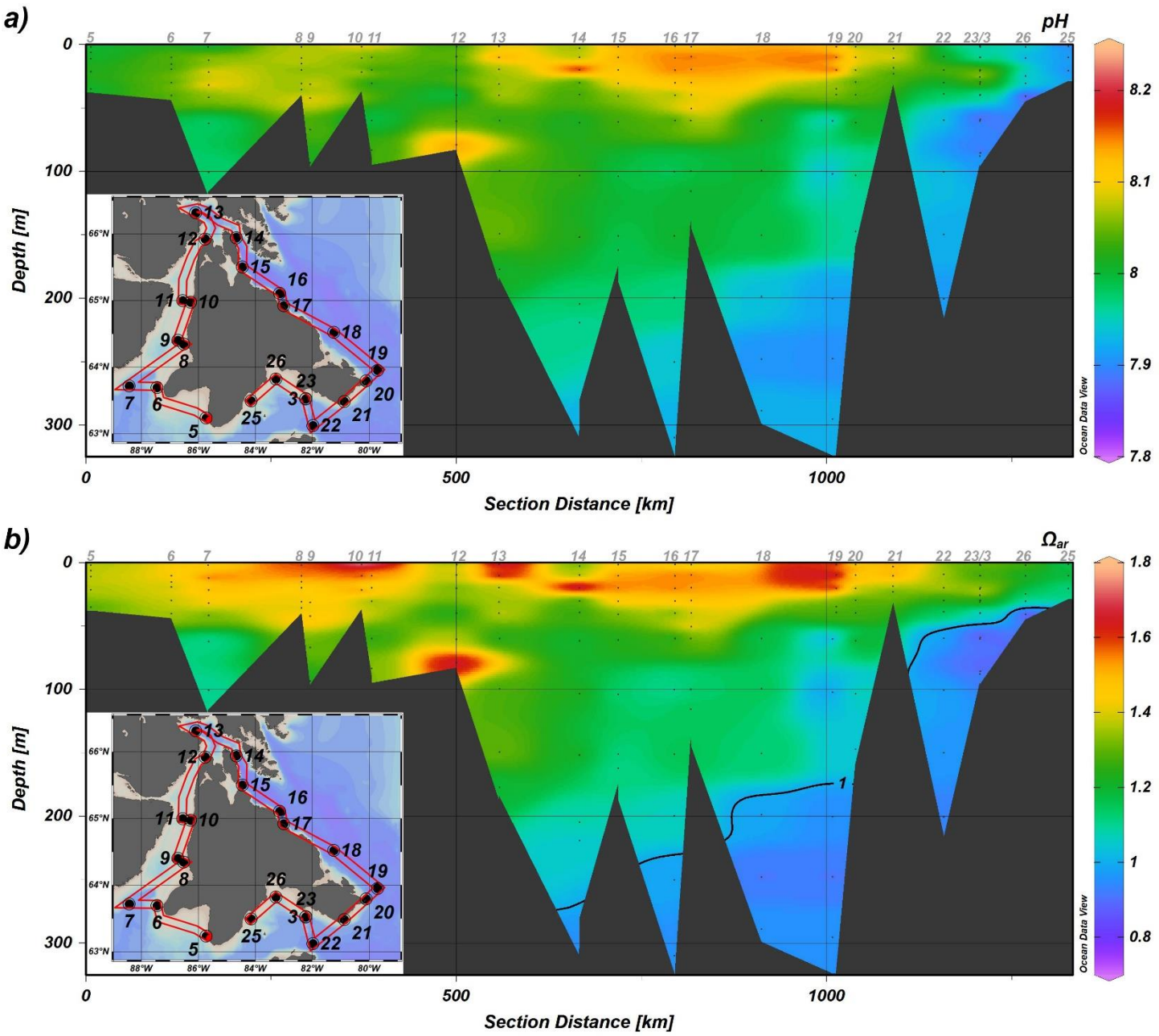

Figure 27. Section plots of a) pH values expressed on the total scale and b) aragonite saturation states (Ω_{ar}). Contour line denotes $\Omega_{ar} = 1$. Station IDs are provided above the panels in gray.

Surface values of pCO_2 ranged from 276.68 µatm (Station 19 in Foxe Channel) to 563.30 µatm (Station 23 in South Bay). As illustrated in Figure 28, high values of surface pCO_2 were observed in South Bay, Fisher and Evans Straits, Bay of Gods Mercy, and at the northern entry

to and southern exit from Roes Welcome Sound, whereas the eastern side of the Island showed low values of pCO_2.

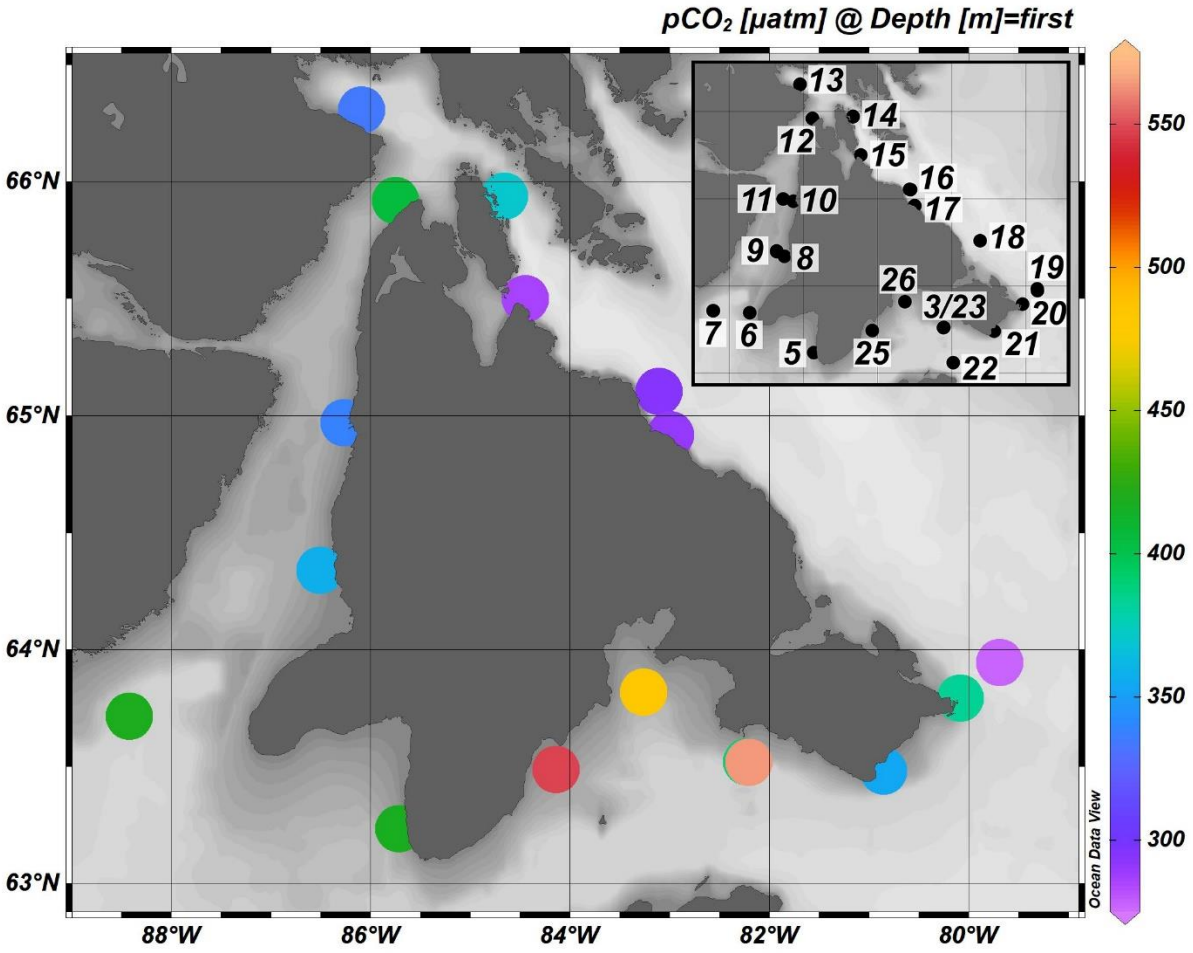

Figure 28. Surface plot of partial pressure of carbon dioxide (pCO_2) (sample depth <5 m). Inset shows station IDs.

Across all depths, pCO_2 values ranged from 247.92 µatm (Station 19, depth = 20.0 m) to 635.67 µatm (Station 23, depth = 59.0 m). As seen in Figure 29, lower values of pCO_2 were found at the surface on the eastern side of the Island and in Roes Welcome Sound, whereas higher values were found at depths at most stations (with the exception of Station 12, which curiously experienced a minimum in pCO_2 near its bottom) and Stations 23, 25 and 26 where seawater with relatively high pCO_2 (>~500 µatm) was observed in the upper portion of the water column.

Pronounced undersaturation was observed in the upper 50 m of the water column on the Foxe Basin side of Southampton Island.

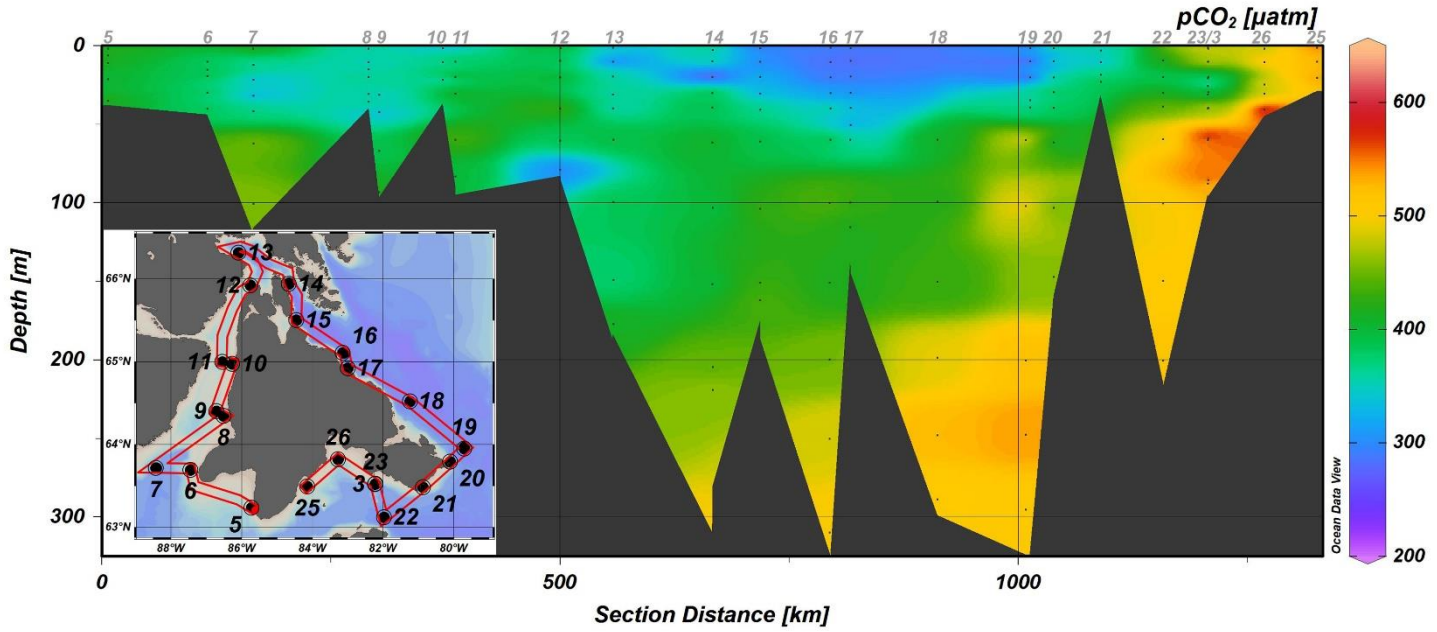

Figure 29. Partial pressure of carbon dioxide (pCO_2) values. Station IDs are provided above the panel in gray.

4.6 AOU and Processes Regulating Dissolved O_2 and CO_2

Depth profiles of O_2 percent saturation and AOU are shown in Figure 30. As discussed in Section 3.6, the O_2 percent saturation and AOU values were calculated at sampling depths using values from the upcast rosette bottle files as this allows further comparison with carbon data (e.g., pCO_2 saturation) from these sampling points. Near the surface throughout the whole study region, O_2 saturation values were near their air-saturated equilibrium value (i.e., 100%). Slight super-saturation was observed near the surface in Repulse Bay (Station 13) and on the Foxe Basin side of the Island (Stations 15-19). O_2 undersaturation was observed at intermediate and bottom depths throughout the whole region, with O_2 saturation minimum (77.6%) being observed in the bottom waters (200.6 m) of Station 22.

Greatest values of AOU were observed in bottom waters of Station 22 (sample depth = 200.6 m, AOU = 81.7 µmol kg^{-1}, O_2 saturation = 77.6%, θ = -1.04°C). As seen in Figure 30, high values were also observed near the bottom of Station 7 at the southern exit from Roes Welcome Sound,

near the bottom of Station 14 in Frozen Strait, and in bottom waters of the eastern side of the Island (Stations 15 – 20). Near-zero and negative values were found near the surface at most stations. Surface values ranged from -20.3 µmol kg^{-1} at Station 16 in Foxe Basin to 17.1 µmol kg^{-1} at Station 14 in Frozen Strait.

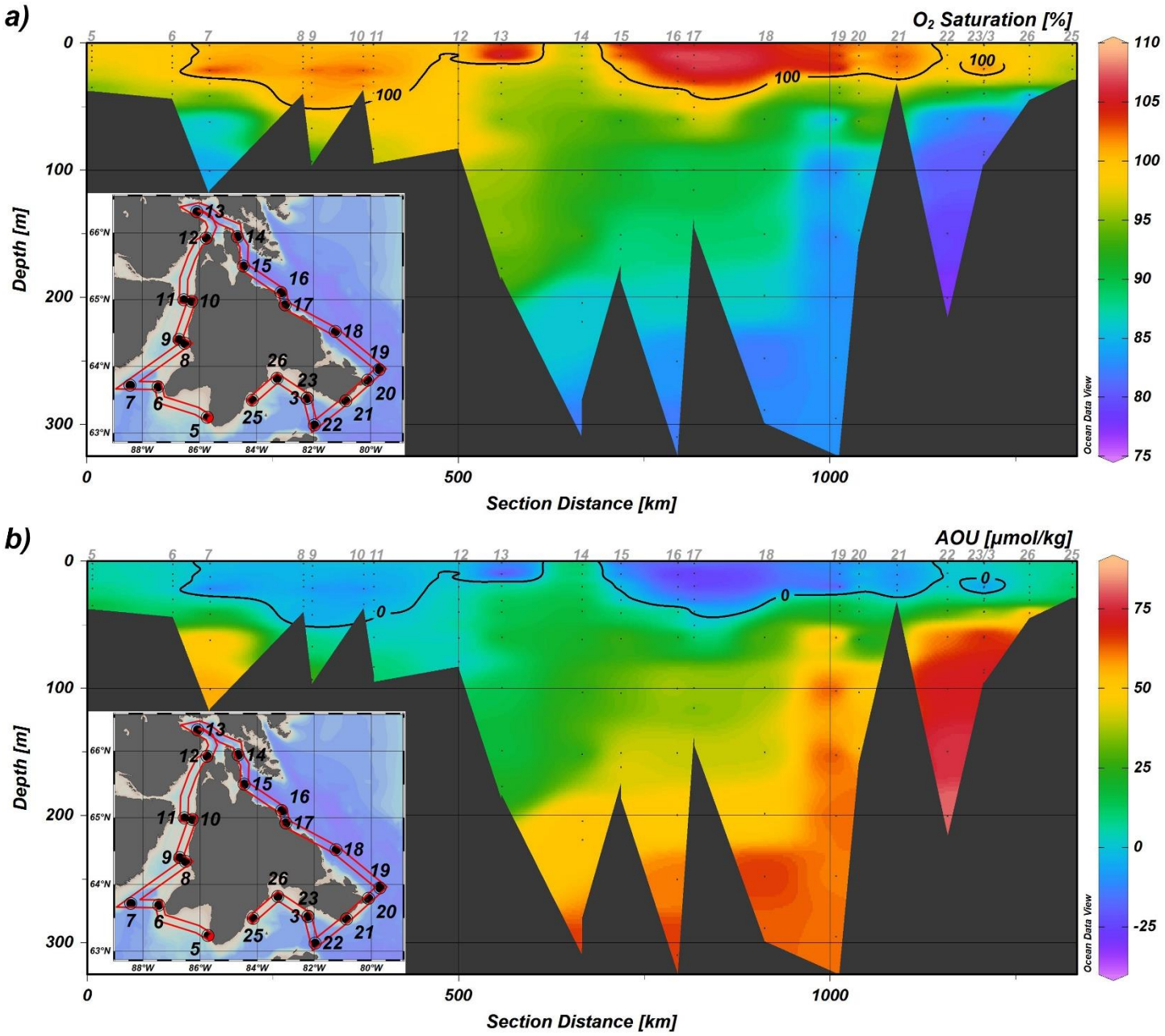

Figure 30. Section plots of a) dissolved oxygen (O_2) percent saturation and b) apparent oxygen utilization (AOU), both calculated at sampling depths using values from the upcast rosette bottle files. Contour line in panel a denotes O_2 saturation of 100%, and in panel b it denotes AOU of 0 µmol kg^{-1}. Station IDs are provided above the panels in gray.

The mean monthly value of atmospheric xCO_2 in Churchill for August 2019 was 400.89 ppm (standard deviation of the reported mean value = 1.7689 ppm; n = 6994) (ECCC, 2021). Using temperature and salinity values of the surface samples (n = 21), hourly values of pressure, air temperature, and xCO_2 from sources outlined in Section 3.7, and Eq. 27 – Eq. 29, the mean atmospheric pCO_2 was calculated to be 397.90 µatm (standard deviation = 2.60 µatm; n = 21). This allowed for calculation of percent saturation of seawater pCO_2 relative to the atmosphere using Eq. 30.

Surface distributions of AOU, O_2 saturation, and pCO_2 saturation are shown in Figure 31. The saturation states of surface seawater pCO_2 ranged from 69.2 to 140.5% relative to the atmosphere. O_2 saturation values of surface seawater ranged from 95.2 to 105.9%. Panel a shows that surface AOU values were negative in Repulse Bay, Foxe Basin, and Foxe Channel, positive in Frozen Strait, Bay of Gods Mercy, and South Bay, and close to zero elsewhere. The distribution pattern of surface O_2 saturation values, shown in panel b, corresponds to that of AOU values, where surface O_2 saturation values were >100% in Repulse Bay, Foxe Basin, and Foxe Channel, <100% in Frozen Strait, Bay of Gods Mercy, and South Bay, and close to 100% elsewhere. As seen in panel c, most surface samples displayed undersaturation in pCO_2 relative to the atmosphere. Of the 17 stations for which there are surface pCO_2 saturation values, only six experienced oversaturation: Station 12 at the northern entrance to Roes Welcome Sound, Station 7 at the southern exit from Roes Welcome Sound, Station 5 in Bay of Gods Mercy, and Stations 23 – 26 in South Bay, with greatest oversaturation being observed in South Bay (Station 23, pCO_2 saturation = 140.5%).

Stations 3 and 23 demonstrate how various properties changed in the same location over time during the cruise, as these two stations were located in the same place, but Station 3 was sampled on August 6, 2019, whereas Station 23 was sampled on August 25, 2019. Station 3 surface values were as follows: AOU = 1.7 µmol kg^{-1}, O_2 saturation = 99.4%, pCO_2 saturation = 98.2%. Station 23 surface values were as follows: AOU = 2.6 µmol kg^{-1}, O_2 saturation = 99.1%, pCO_2 saturation = 140.5%. As such, AOU and O_2 saturation values did not change noticeably in the nearly 3 weeks between sampling at that location, but the pCO_2 saturation increased by 42.3% likely due to a combined effect of respiration and warming (sea surface temperature increased by 0.83°C).

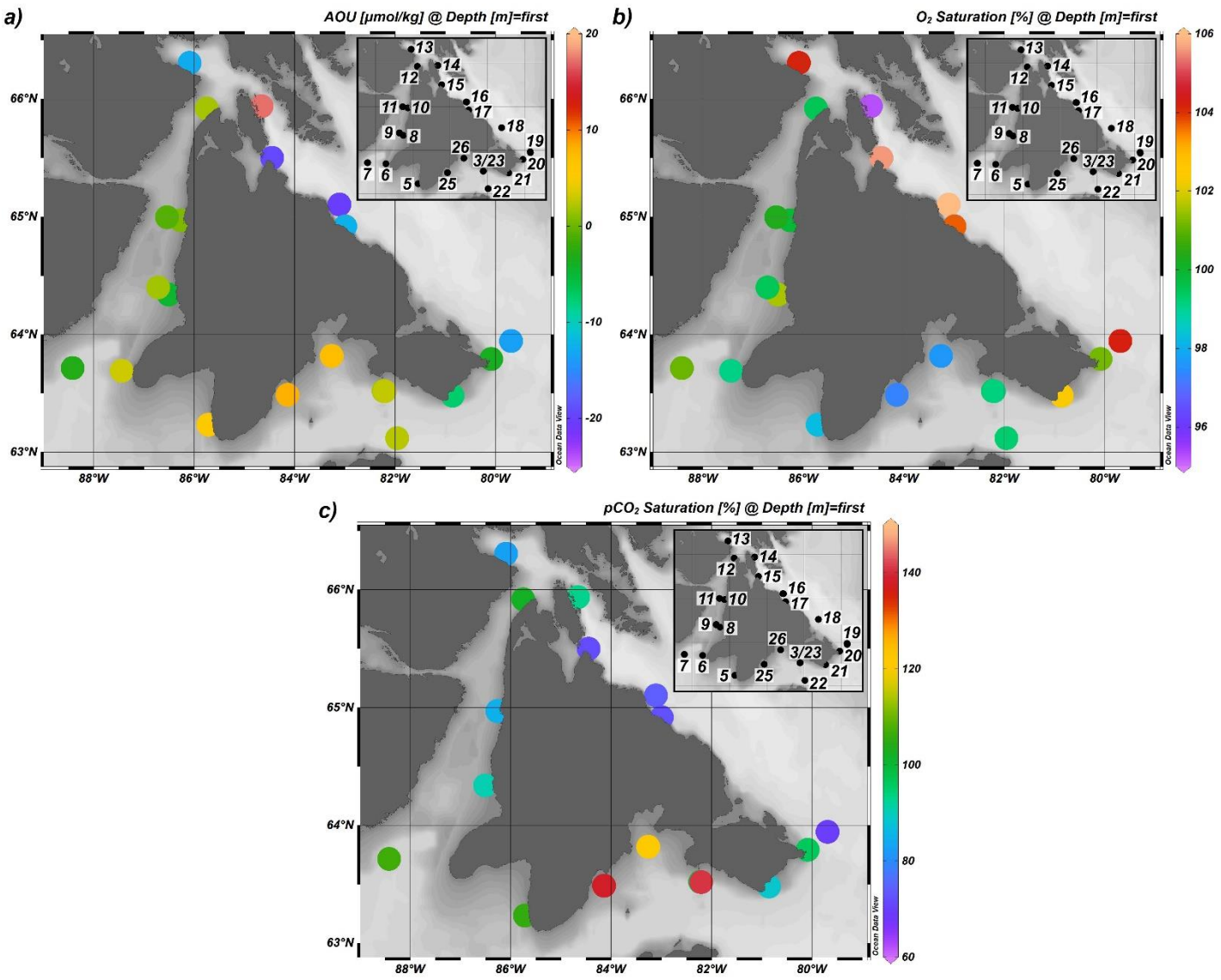

Figure 31. Surface plots of a) apparent oxygen utilization (AOU), b) dissolved oxygen (O_2) percent saturation, and c) percent saturation of seawater pCO_2. Insets show station IDs.

4.7 Carbon Isotopes

Figure 32 shows the distribution of stable carbon isotope composition of DIC, shown as $\delta^{13}C$, around the Island. Values ranged between 0.09‰ and 1.55‰. High values of $\delta^{13}C_{DIC}$ were found in the top ~20-30 m across most stations, with the highest value (1.55‰) found at 9.9 m at Station 19 in Foxe Channel. Lower values were observed in deeper waters, with the lowest

$\delta^{13}C_{DIC}$ (0.09‰) found at 61.9 m at Station 7 at the southern exit from Roes Welcome Sound.

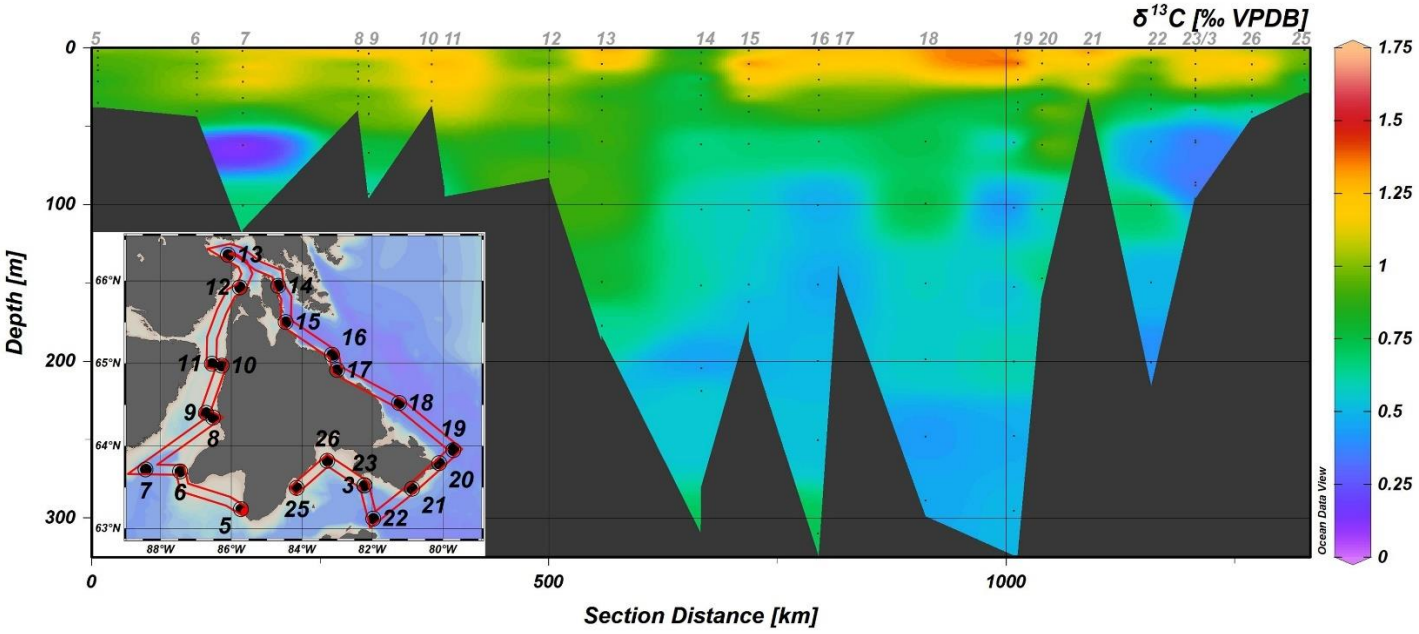

Figure 32. Section plot of stable carbon isotope ratios ($\delta^{13}C$) of dissolved inorganic carbon. Station IDs are provided above the panel in gray.

Values of $\delta^{13}C_{DIC}$ appeared to be inversely related to salinity (Figure 33), with higher salinity (deeper) samples generally having lower $\delta^{13}C_{DIC}$, and vice versa. There is noticeably more scatter in $\delta^{13}C_{DIC}$ at lower salinity.

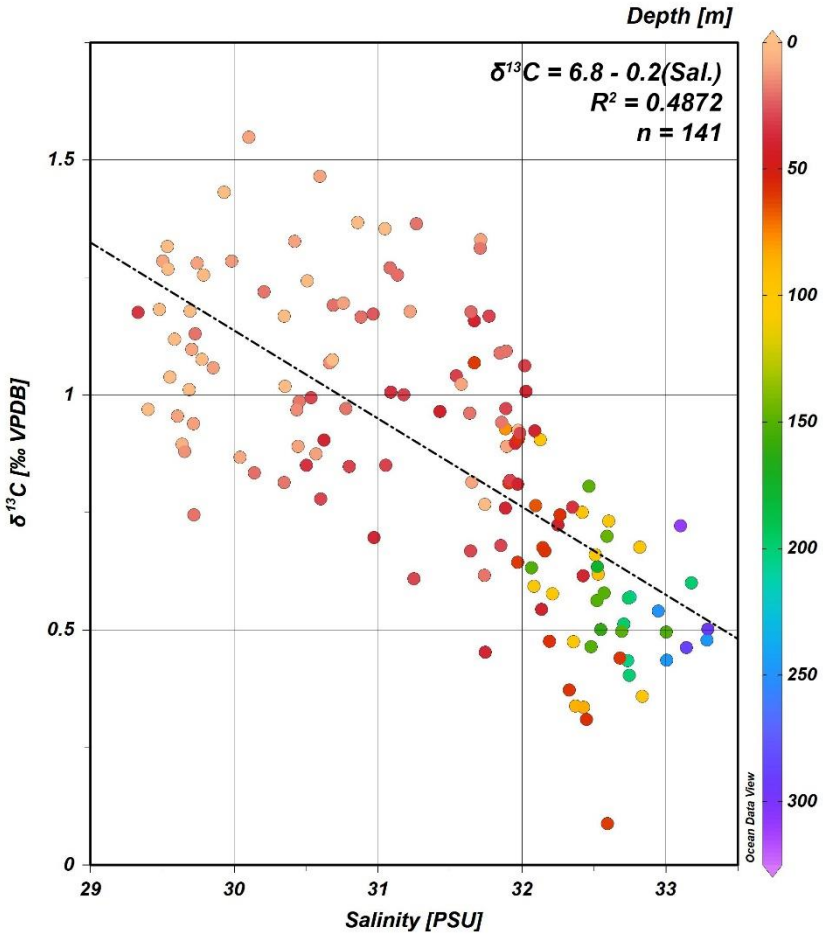

Figure 33. Stable carbon isotope ratios ($\delta^{13}C$) of dissolved inorganic carbon versus salinity, with colour representing sample depth. Salinity values are bottle salinities (except when bottle salinities were missing, CTD salinity values from upcast rosette bottle files were used). Linear regression line, regression equation, and R^2 value are shown.

A plot of $\delta^{13}C_{DIC}$ against PO_4^{3-} concentrations (Figure 34) produced a slope of -1.117 ‰ kg µmol^{-1} (R^2 = 0.7337, n = 129). Following Eq. 18, $\frac{\varepsilon^{13}C_{plant-DIC}}{DIC_{mean}}$ term was calculated by dividing the slope from Figure 34 by the Redfield C:P ratio of organic matter (106:1; Redfield et al., 1963). The resulting value of $\frac{\varepsilon^{13}C_{plant-DIC}}{DIC_{mean}}$ term was -0.011 ‰ kg µmol^{-1}, which represents the estimated rate of change in $\delta^{13}C_{DIC}$ from respiratory DIC inputs in this study area. A simple arithmetic mean of all available DIC values (n = 153) gives 2096.79 µmol kg^{-1}. Multiplying the DIC mean value by the $\frac{\varepsilon^{13}C_{plant-DIC}}{DIC_{mean}}$ value (-0.011 ‰ kg µmol^{-1}) suggests that photosynthetic fractionation of stable carbon isotopes by marine primary producers in this study region is -23‰.

This falls within the range reported in literature, $\varepsilon^{13}C$ = -30‰ to -18‰ (Zeebe and Wolf-Gladrow, 2001; Hoefs, 2009).

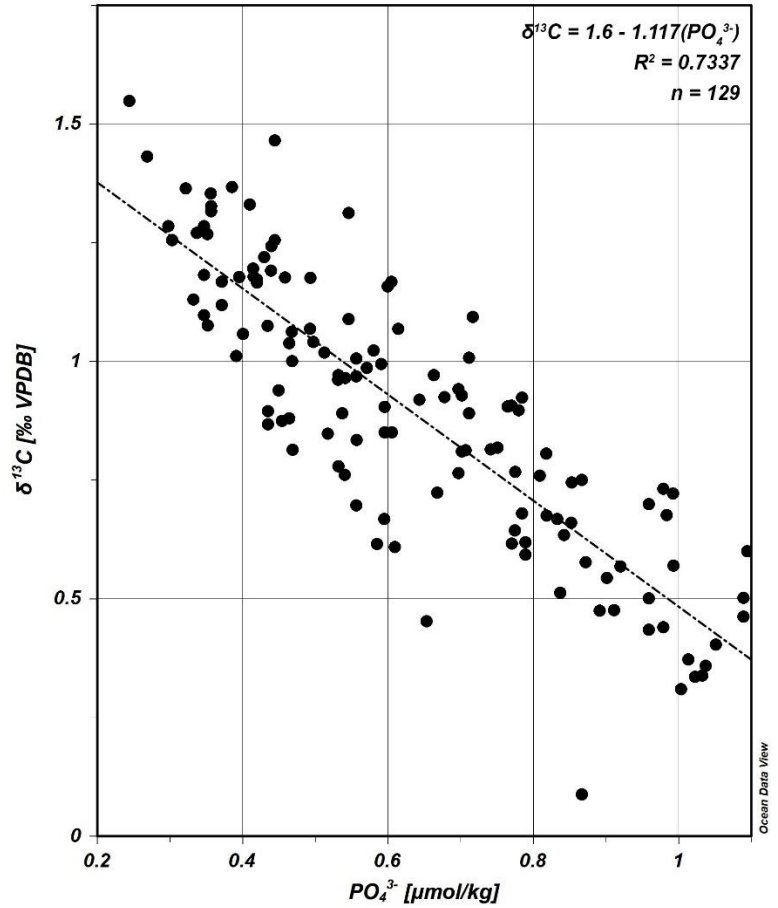

Figure 34. Stable carbon isotopic composition of dissolved inorganic carbon ($\delta^{13}C$) versus phosphate (PO_4^{3-}) concentrations. Linear regression line, regression equation, and R^2 value are shown.

From the plot of $\delta^{13}C_{DIC}$ against DIC concentrations (Figure 35), it can be seen that the slope of the best fit line through these data produced a much shallower slope (-0.003‰ kg µmol^{-1}, R^2 = 0.6801, n = 136) than would be expected if photosynthesis and respiration were the only processes controlling concentration and isotopic composition of DIC (-0.011‰ kg µmol^{-1}). It is also apparent from the figure that isolating any one region around the Island would not appreciably change the slope of the best fit line through the data.

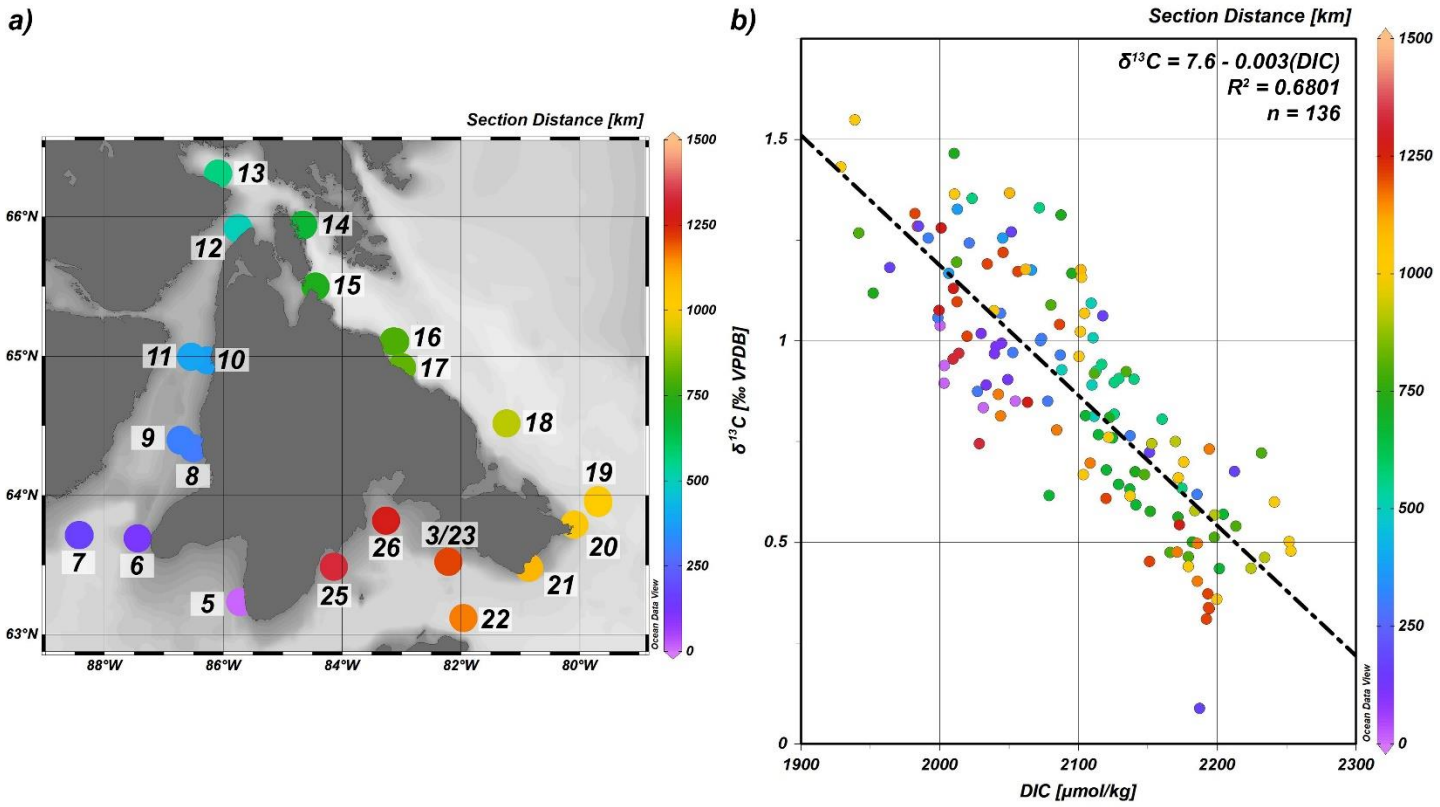

Figure 35. Stable carbon isotopic composition of dissolved inorganic carbon ($\delta^{13}C$) plotted against dissolved inorganic carbon (DIC), with colour representing section distance in both the map (a) and plot (b). Linear regression line, regression equation, and R^2 value are shown.

To examine the effects of various processes on DIC concentrations and isotopic compositions, deviations of observed DIC and $\delta^{13}C_{DIC}$ from values expected from conservative mixing of RW, SIM, and SW, were calculated using Eq. 31 – Eq. 34. Results are plotted in Section 5.4. Below is a description of how vector slopes for the various processes that could produce these deviations were determined in order to visualize them on a plot of $\Delta\delta^{13}C_{DIC}$ versus ΔDIC.

The three processes that decrease DIC concentrations and increase $\delta^{13}C_{DIC}$ values, thereby driving ΔDIC to be more negative and $\Delta\delta^{13}C$ to be more positive, are $CaCO_3$ precipitation, outgassing of CO_2, and primary production. For this study, ε_{CO_2} (calculated as per Eq. 35 and Eq. 36) ranged from -12.1‰ to -10.8‰. Consequently, α_{CO_2} (calculated as per Eq. 37) ranged from 0.988 to 0.989. Using α_{CO_2} of 0.989 in Eq. 38, a slope of -11 is obtained for the CO_2 outgassing vector.

It was determined above that the photosynthetic fractionation of stable carbon isotopes by marine primary producers in this study area was approximately -23‰. Using Eq. 37, the fractionation factor for primary production (α_{PP}) was estimated to be 0.977. By substituting α_{PP} for α_{CO2} in Eq. 38, it was estimated that the uptake of small amounts of CO_2 by primary producers gives a slope of -23 on a $\Delta\delta^{13}C$ versus ΔDIC plot.

Assuming $\delta^{13}C_{CaCO3}$ = 0‰ (Alling et al., 2012), the slope of the vector for $CaCO_3$ dissolution, calculated using Eq. 39, could range from -0.1 to -0.8, since the values of $\delta^{13}C_{mix}$ ranged from 0.12‰ to 0.83‰. The mean value of $\delta^{13}C_{mix}$ was 0.48‰, so a slope of -0.5 was used in Figure 40. It was assumed that the vector for the precipitation of $CaCO_3$ would be in opposing direction but of the same slope as the $CaCO_3$ dissolution vector. Thus, dissolution of $CaCO_3$ increases DIC and lowers $\delta^{13}C$ in these waters, while $CaCO_3$ precipitation does the opposite. Other processes that increase DIC concentrations and simultaneously decrease $\delta^{13}C_{DIC}$ values are the uptake of atmospheric CO_2 and degradation of organic carbon (OC), as described in Section 2.6.1. It was assumed that CO_2 uptake and OC degradation would give vectors of opposing direction but of the same slopes as the CO_2 outgassing and primary production vectors, respectively.

Chapter 5: Discussion

Application of physical-chemical tracer data demonstrated that multiple processes influenced the carbonate system in the Southampton Island area. Discussion below is structured into four parts. The first two sections discuss the distribution of different water masses (MW, SIM, Atlantic and Pacific waters) in the region and the seawater physical properties. The third and fourth sections describe the physical and biological controls, respectively, on the distribution of carbonate species.

5.1 Distributions of Freshwater and Brine in the Water Column

The highest fractions of SIM were observed in surface samples of Stations 15-17 on the Foxe Basin side of the Island (Figure 19), which were also characterized by distinctly lower salinities and temperatures (Figure 13). These results are unsurprising as this region experienced the most recent loss of sea ice (Figure 9). Stations with higher fractions of MW were found to the west and south of the Island. It could be surmised that Stations 6-11 in Roes Welcome Sound were showing a meteoric water signal due to inputs from Wager Bay, which receives freshwater from several small rivers, previously discussed in Section 2.2. Stations 3-5 and 22-26 were in part affected by riverine input local to Southampton Island, namely from Boas River in the Bay of Gods Mercy, and Kirchoffer and Ford Rivers in South Bay. As noted in Section 2.2, discharge data is lacking for all Southampton Island rivers except Kirchoffer River, whose August flow ranged from 12.2 to 71.8 m^3 sec^{-1} during the 5 years flow was gauged (see Table 1; ECCC, 2022). The maximum August flow observed for Kirchoffer River was about 30 times less than the mean August flow of Chesterfield Inlet in northwestern Hudson Bay, estimated to be 2387 m^3 sec^{-1} (see Table 1; Bugdell, 1976). Loewen et al. (2020) also stated that discharge from Southampton Island rivers is low year-round. Considering the low flow values expected for Southampton Island rivers in August, it is unlikely that they could produce such high fractions of MW observed throughout the water column of the southern stations, especially at Station 22 near Coats Island, which was located farthest from the major Southampton Island rivers. As such, these results suggest that the region to the south of the Island (Bay of Gods Mercy, Fisher Strait, South Bay, and Evans Strait) may be affected by freshwater input from elsewhere. Circulation model proposed by Ridenour et al. (2019) (see Section 2.2) suggests that it could be signals of freshwater from Hudson Bay's northwestern rivers, as surface currents move cyclonically from Roes Welcome Sound down to Churchill, Nelson, and Hayes River estuaries before returning to

northwest Hudson Bay to pass between Southampton and Coats Islands (see the spring and summer panel in Figure 3).

The apparent MW end-member $\delta^{18}O$ value in the study region was -11.1‰. Previously estimated MW end-member $\delta^{18}O$ values for Hudson Bay range from -15.4‰ (Ahmed et al., 2020) to -14.0‰ (Granskog et al., 2011). As such, the apparent MW end-member for the Southampton Island region is more ^{18}O-enriched than previously reported values for Hudson Bay. This provides further evidence of the predominant source of meteoric water in the study region being a mix of the Churchill, Nelson, and Hayes Rivers, which have relatively enriched $\delta^{18}O$ values of -12.71‰, -10.81‰, and -11.45‰, respectively (Burt et al., 2016). Alternative hypothesis is that mixing of MW and SIM at the regional scale produces an intermediate MW $\delta^{18}O$ value observed around Southampton Island. In order to arrive at the observed apparent MW $\delta^{18}O$ signal of -11.1‰, it would take 71% MW ($\delta^{18}O$ = -15.4‰; Ahmed et al., 2020) and 29% SIM ($\delta^{18}O$ = -0.8 ‰; Ahmed et al., 2020) mixing at the regional scale in Hudson Bay and then getting re-circulated into the Southampton Island region. In other words, it could be inferred that the dominant freshwater source around Southampton Island is a regional freshwater signal of mixed origin.

Most stations showed a brine signal within their subsurface waters. The Southampton Island region is affected by brine production within Foxe Basin Polynya north of the Island, Roes Welcome Sound Polynya west of the Island, and a region of water kept open by currents immediately to the north of the Island, as such, considering circulation patterns of the region (described in Section 2.2), widespread signals of brine around the Island are to be expected. Coldest, most saline, and most brine-rich waters were found at Station 19 (Figure 12), where the cold saline water mass spanned from the bottom up to about 50 m from the surface. That is, the cold saline waters found at Station 19 came up higher in the water column than at similarly deep stations around the Island. It is possible that these waters are the remnants of the western Foxe Basin polynyas' dense water pulse described previously in Section 2.2. Latent heat polynyas located along the western coast of Foxe Basin (at Hall Beach, along Melville Peninsula, and at Lyon Inlet) annually produce a pulse of cold, saline waters following mid-winter opening of these polynyas (Defossez et al., 2008, 2010). These new dense waters replace about two-thirds of the Foxe Basin's deep waters and they reach the sill found at 180 m depth between Southampton

and Nottingham Islands by summertime (Defossez et al., 2008, 2010). Defossez et al. (2008, 2010) stated that the cold, saline current may have enough kinetic energy to overflow the sill (Defossez et al., 2008, 2010), which is consistent with findings of Saucier et al. (2004), who also determined numerically that some dense waters might be able to overflow this sill from Foxe Basin into Hudson Bay. As such, the cold, saline waters at the easternmost station in Foxe Channel (Station 19) might be the brine-rich waters produced during the winter dense water pulse in western Foxe Basin, and since these dense waters at Station 19 come up high in the water column (~50 m from surface), they would be able to cross the sill at 180 m depth from Foxe Channel into northeastern Hudson Bay.

5.2 Sources of Seawater in the Southampton Island Region

There appear to be two distinct water masses between ~100 m and ~200 m depth in the study region. Both water masses are cold and saline, but the one found at Station 22 is ^{18}O-enriched. $\delta^{18}O$ values of samples from Station 22 approach the Hudson Bay SW end-member as defined by Granskog et al. (2011) (salinity = 32.8, $\delta^{18}O$ = -1.5‰), meanwhile deep samples from all other stations cluster around the less saline, more ^{18}O-depleted SW end-member calculated for this study (salinity = 32.3, $\delta^{18}O$ = -2.2‰), indicating two different sources of seawater between Station 22 (which likely receives its source SW from Hudson Bay) and deep stations located on the Foxe Basin/Channel side of the Island. Results from Figure 20 (nitrate plus nitrite versus phosphate plot) suggest that there is little Atlantic seawater influence in the Southampton Island region.

Using TA and DIC in addition to salinity and temperature, Jones and Anderson (1994) attempted to describe water masses and circulation in northern Hudson Bay, Hudson Strait, and Foxe Basin. They deduced using data from stations located on the western side of Foxe Basin that the Arctic Ocean Surface Mixed Layer water flows into Foxe Basin and mixes with Foxe Basin Winter Surface Water and sea-ice meltwater, and that bottom waters of Foxe Basin show signals of brine (Jones and Anderson, 1994). Following their approach, the mean and standard deviation of all ΔTA values in the study region were calculated to be -6.1±19.7 μmol kg^{-1}. ΔTA of 0 indicates pure Pacific water, as such, the proximity of the mean ΔTA to that of pure Pacific water further supports that Atlantic seawater does not have a strong influence on the Southampton Island region and that water masses found in this region are likely of Pacific origin. However, as

discussed in Section 4.4, there was a negative slope in ΔTA versus salinity plots, where ΔTA becomes more negative with increasing salinity, complicating interpretation of the data. One possible explanation of negative ΔTA values is some presence of Atlantic-influenced water. If the samples were pure Atlantic water (salinity = 34.85, TA = 2292 µmol kg^{-1}; Jones et al., 2008), ΔTA would be -158.4 µmol kg^{-1}. As such, while there is little evidence of Atlantic-influenced water near Southampton Island, its small presence (accounting for not more than one-third of subsurface waters at certain stations) cannot be fully ruled out. However, a more likely explanation for the negative ΔTA in the study region is brine rejection, which could also result in negative ΔTA values, as addition of brine can greatly increase the salinity of deep waters. The calculated ΔTA minimum in this study was -49.9 µmol kg^{-1} at 60.2 m at Station 19 near Foxe Channel. Negative values of ΔTA were mostly found at depth in South Bay, Evans Strait, and on the Foxe Basin/Channel side of the Island, as seen in Figure 22, and correspond relatively well with the distribution of brine in the water column, as shown in Figure 19. Addition of riverine runoff, and to a lesser extent sea-ice melt, to pure Pacific water would make ΔTA >0. As seen in Figure 22, ΔTA values were greatest at and near the surface on the south and west sides of the Island. The distribution of positive ΔTA values within this study area was generally consistent with distributions of positive values of f_{SIM} and f_{MW}, shown in Figure 19, calculated using salinity and $\delta^{18}O$ end-members.

5.3 Physical Controls on the Distribution of Carbonate Species

The distributions of DIC and TA (Figure 25) around Southampton Island mimicked those of salinity (Figure 12), with high DIC and TA observed in high salinity, low temperature, O_2-undersaturated regions found in the bottom waters of most stations, consistent with other studies in Hudson Bay (e.g., Azetsu-Scott et al., 2014; Burt et al., 2016). Azetsu-Scott et al. (2014) reported that within deep Foxe Basin and Hudson Strait, concentrations of DIC ranged from 2150 to 2230 µmol kg^{-1}, whereas deep waters of Hudson Bay reached DIC values over 2300 µmol kg^{-1}, attributed to respiration. Alkalinity in deep waters in western Hudson Bay also reached above 2300 µmol kg^{-1} (Azetsu-Scott et al., 2014; Burt et al., 2016). DIC and TA minima observed in the Bay were <1800 µmol kg^{-1} and <1900 µmol kg^{-1}, respectively, meaning that the ranges of DIC (1853.63 – 2253.23 µmol kg^{-1}) and TA (1976.25 – 2323.39 µmol kg^{-1}) values observed in the Southampton Island region were smaller and fell within the ranges previously reported for Hudson Bay (Azetsu-Scott et al., 2014; Burt et al., 2016). Lower DIC and TA were

generally found in low salinity, largely O_2-oversaturated, near surface waters of variable temperatures, particularly at stations in Foxe Basin/Channel where surface waters were fresher and colder. Lower surface values of DIC and TA observed in this area were possibly a consequence of a shallow lens of sea-ice meltwater near the surface (Figure 19), given sea-ice melt is characteristically lower in DIC and TA than seawater (AMAP, 2013).

As seen from surface distribution of O_2 and pCO_2 saturation values shown in Figure 31, surface waters were oversaturated in O_2 in Repulse Bay and Foxe Basin/Channel, undersaturated in Frozen Strait, Bay of Gods Mercy, and South Bay, and close to saturation elsewhere. pCO_2 oversaturation was observed in surface waters at the northern and southern ends of Roes Welcome Sound and to the south of the Island. Surface waters at Stations 23-26 were characterized by high surface temperatures and great pCO_2 oversaturation, and hence these were likely areas of CO_2 outgassing to the atmosphere. All other surface values showed undersaturation in pCO_2. Loosely following the approach described by Carrillo et al. (2004), O_2 percent saturation was plotted against pCO_2 percent saturation, as seen in Figure 36.

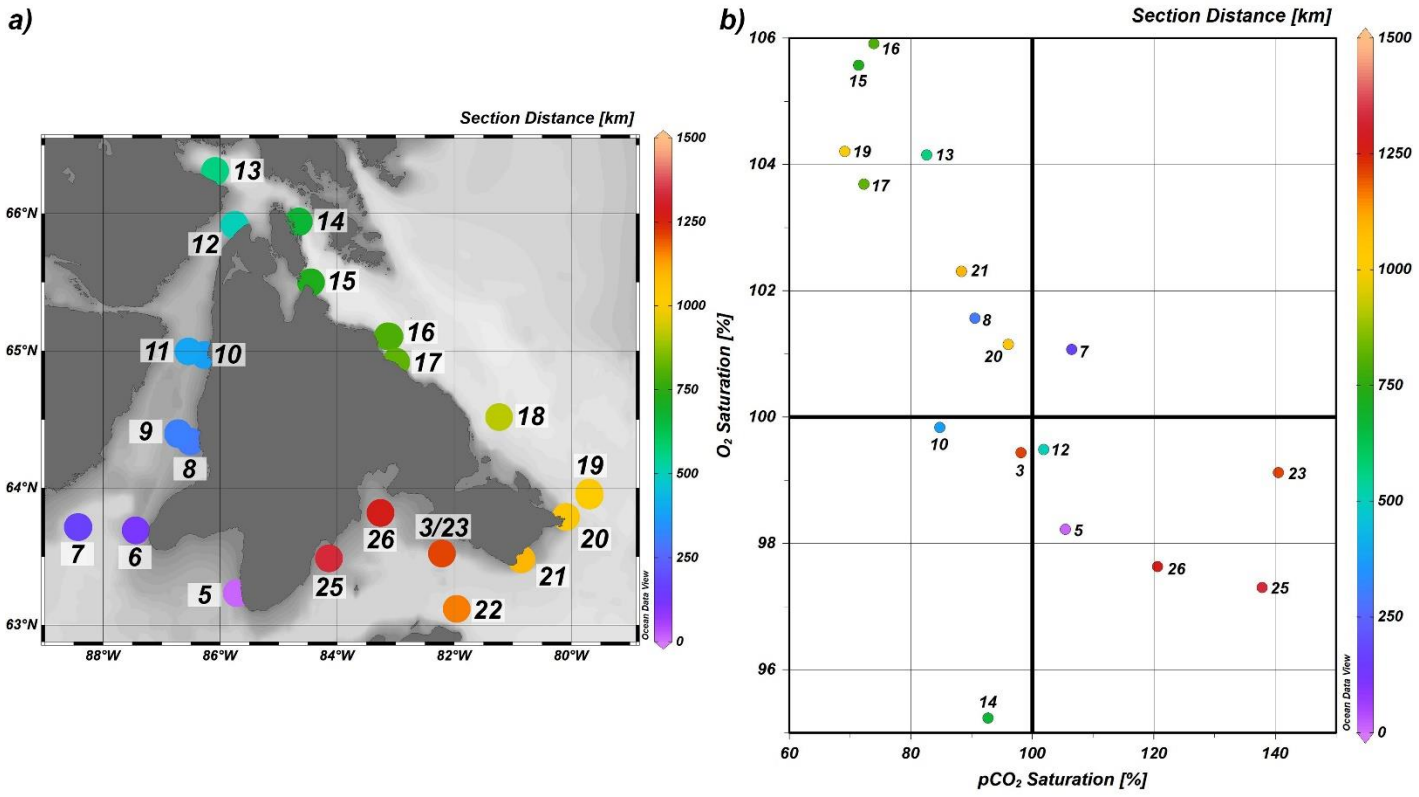

Figure 36. Dissolved oxygen (O_2) percent saturation versus percent saturation of seawater pCO_2 of surface samples (n = 17), with colour representing section distance in both the map (a) and plot (b).

Stations 3 in South Bay, 10 in Roes Welcome Sound, and 14 in Frozen Strait displayed surface undersaturation in both pCO_2 and O_2, indicating that recent water cooling might have played a role. Station 14 had a low surface temperature value (1.00°C) at the time of sampling, but surface waters at Stations 3 and 10 were relatively warm at 7.13°C and 7.65°C, respectively. The only station to show surface supersaturation of both pCO_2 and O_2, suggesting that recent water heating had occurred, was Station 7 at the southern end of Roes Welcome Sound. Indeed, surface temperatures recorded at this station were high at 8.73°C. It is important to note that these interpretations of Figure 36 are speculative as all O_2 saturation values were close to air-saturated values (surface seawater O_2 saturation values ranged from 95.2 to 105.9%). The lack of a strong correlation between pCO_2 saturation and temperature or salinity, as seen in Figure 37, suggests that the role of physical controls (heating, cooling, freshening, salting out) on pCO_2 saturation states were not straightforward. A positive correlation between salinity and pCO_2 percent

saturation is seen only when samples with salinity greater than 29.9 are considered (pCO_2 Saturation = -240 + 11·Salinity, R^2 = 0.5531, n = 8).

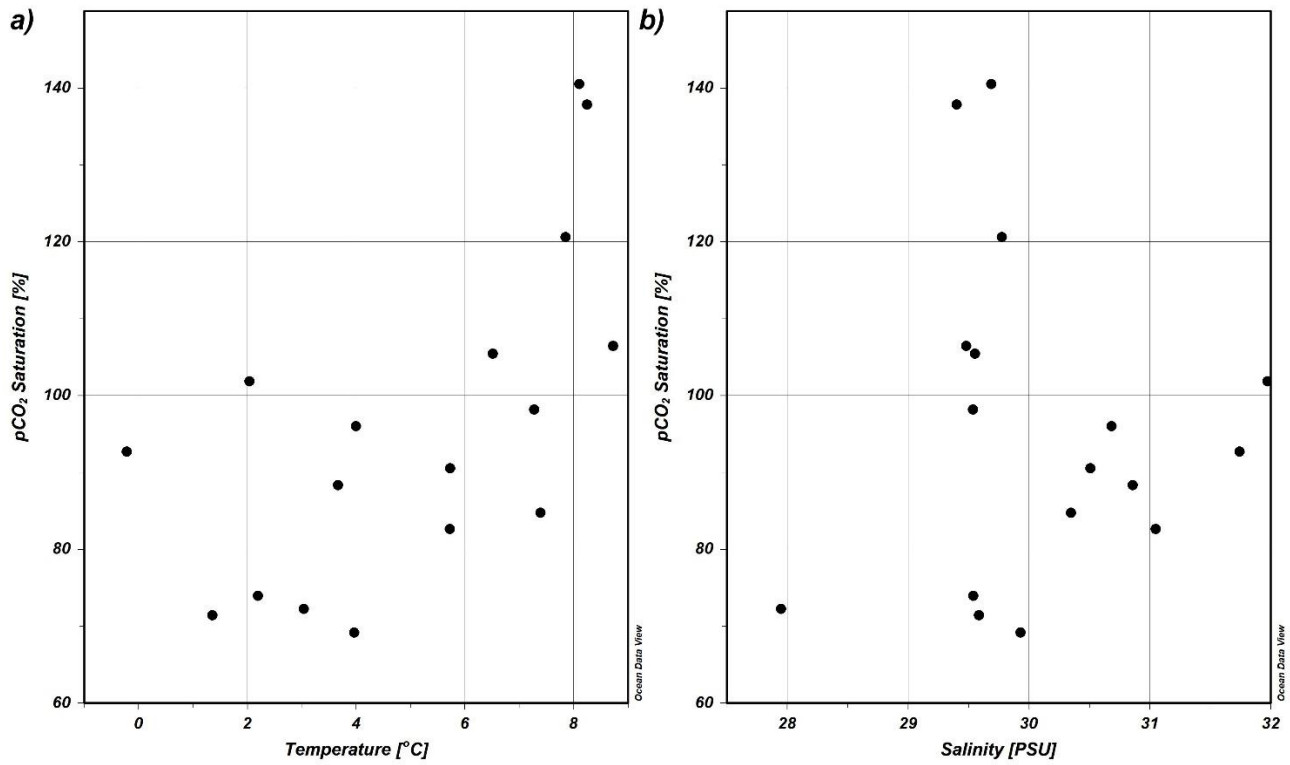

Figure 37. Percent saturation of seawater pCO_2 of surface samples (n = 17) versus a) seawater temperature (CTD temperature values from the upcast rosette bottle files) and b) bottle salinity values.

Further complicating interpretations is air-sea gas exchange which drives both O_2 and CO_2 to their air-saturated values at different rates, with O_2 equilibrating faster than CO_2 in surface waters. Additionally, temperature was previously found to be highly correlated with pCO_2 in Hudson Bay (Ahmed et al., 2021). Indeed, normalization of pCO_2 values from this study to a constant mean sea surface temperature told a slightly different story than Figure 36. With localized water warming/cooling effects removed, variations in temperature-normalized pCO_2 were controlled by biological activity, mixing, and air-sea gas exchange. Figure 38 shows values of ΔpCO_2, calculated as $pCO_{2(at\ 5°C)}$ - $pCO_{2(obs)}$, which demonstrates how temperature normalization changed values of pCO_2. Temperature normalization reduced values of pCO_2 in some areas (negative ΔpCO_2), while in other areas an increase in pCO_2 was observed following

temperature normalization (positive ΔpCO_2). In Repulse Bay, and from Wager Bay southeast to South Bay (Station 23), temperature normalization reduced values of pCO_2, suggesting that observed values of pCO_2 could be in part attributed to higher-than-average water temperatures. Only stations on the south side of the Island (Stations 5, 7, 23, 25, 26) had observed pCO_2 values oversaturated with respect to atmospheric pCO_2. Effects of localized warming appeared to be greatest at the southern end of Roes Welcome Sound (Station 7) and in South Bay, with temperature normalization reducing pCO_2 values by up to ~70 µatm. Meanwhile, lower-than-average water temperatures were in part responsible for the pCO_2 values observed at the northern entrance to Roes Welcome Sound (Station 12), and from Frozen Strait south to Evans Strait (Stations 14-17, 19-21), with temperature normalization increasing pCO_2 values by up to ~91 µatm (Station 14 in Frozen Strait). These areas were generally undersaturated with respect to atmospheric pCO_2, except Station 12.

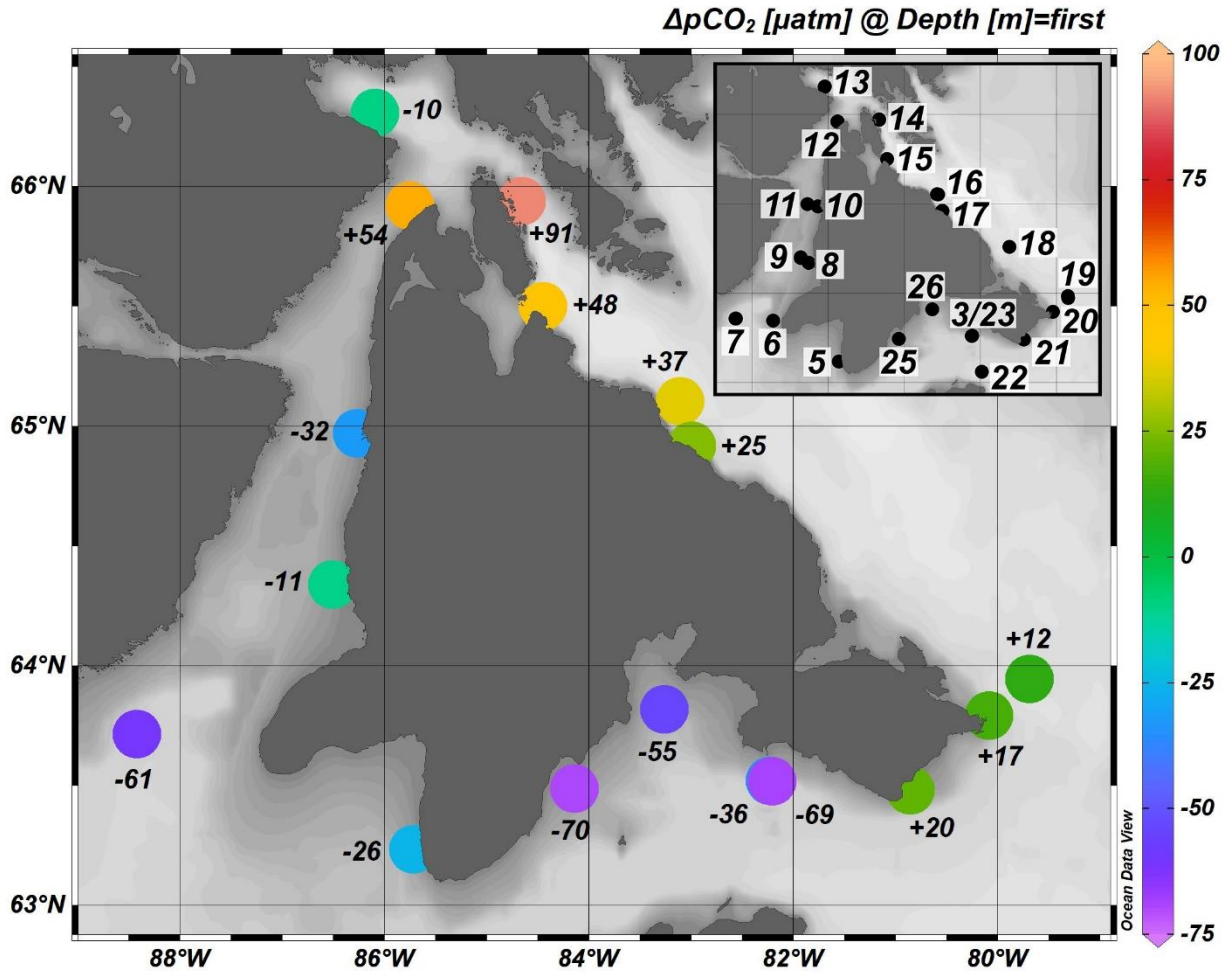

Figure 38. Differences in pCO_2 between observed and temperature-normalized values, calculated as $\Delta pCO_2 = pCO_{2(at\ 5°C)} - pCO_{2(obs)}$. Numbers next to data points show the value of ΔpCO_2 for each sample. Inset shows station IDs.

5.4 Biological Controls on the Distribution of Carbonate Species

Previously discussed plot of O_2 percent saturation versus pCO_2 percent saturation (Figure 36) also pointed to biogenic control over surface distributions of dissolved gases. Samples whose pCO_2 was undersaturated (<100%) and O_2 was supersaturated (>100%) indicate that photosynthesis is likely a locally significant process. Surface samples that fit these criteria were found in Repulse Bay (Station 13), on a near-coastal station in Roes Welcome Sound (Station 8), and the rest were found on the eastern side of the Island (Stations 15-17, 19-21). These surface waters were also characterized by enriched $\delta^{13}C_{DIC}$, an indication photosynthesis had taken place.

As discussed in Section 2.6.1, primary production increases $\delta^{13}C_{DIC}$ while respiration decreases $\delta^{13}C_{DIC}$ (Sarmiento and Gruber, 2006). Samples that show pCO_2 supersaturation and O_2 undersaturation suggest that respiration or upwelling of CO_2-enriched waters is likely a locally significant process. These samples were found at the northern end of Roes Welcome Sound (Station 12) and on the southern side of the Island in Bay of Gods Mercy (Station 5) and in South Bay (Stations 23-26). Most of these stations, namely Stations 5, 12, and 25, had relatively depleted surface values of $\delta^{13}C_{DIC}$, further suggestion respiration or upwelling had taken place. Stations 3 and 23 allow for a temporal comparison, as both were sampled in the same location but ~3 weeks apart. Interestingly, surface AOU and O_2 saturation values did not change noticeably, but surface pCO_2 saturation increased by 42.3% in the ~3 weeks between sampling at that location. Consistent slight undersaturation in O_2 and large increase in pCO_2 saturation values suggests that respiration or upwelling had occurred in this region during the cruise.

Surface waters in Foxe Basin/Channel that were characterized by lower DIC and TA and higher f_{SIM} had regionally high pH (maximum of 8.15) and pCO_2 between 276.68 µatm and 293.89 µatm, suggesting that biological uptake was moderating the carbonate system in this area. High pH was also observed in the top ~50 m of Foxe Basin/Channel and Roes Welcome Sound, near surface in Repulse Bay (Station 13), at ~20 m in Frozen Strait (Station 14), and near the bottom (~79 m) of Station 12 at the northern entrance to Roes Welcome Sound (Figure 27). These areas also had lower values of pCO_2 and were generally oversaturated in O_2. Station 12 had high kelp density and the highest kelp biomass observed around the Island (Castro de la Guardia et al., 2023), thus, it is possible that the low pCO_2 (low DIC and high pH) in this vicinity resulted from high photosynthetic uptake by kelp in shallower upslope regions (unless the carbonate system measurements near the bottom of Station 12 were simply erroneous). Foxe Basin and Roes Welcome Sound regions of Southampton Island were also reported to have high kelp biomass of greater than 5 kg m^{-2} according to diving surveys from the 2019 SIMEP expedition (Filbee-Dexter et al., 2022). Kelp forests were typically densest at 23 m depth, becoming smaller and sparser beyond ~30 m depth (Castro de la Guardia et al., 2023). Drop camera footage from the 2019 SIMEP cruise showed that north of Southampton Island outside of Repulse Bay (Stations 12, 14, 15), high canopy extended down to ~40 m and low canopy extended beyond 50 m, whereas to the west and south of the Island, high canopy extended down to ~30 m switching to low canopy down to ~50 m (J. Reimer, personal communication, February 3, 2023). It is possible

that higher pH observed at stations in Roes Welcome Sound is a result of nearshore kelp beds influencing offshore and downstream water properties within this region. One possible mechanism for the redistribution of water from near-shore, shallow regions directly affected by kelp production to offshore, deeper areas is through the recurring coastal Roes Welcome Sound polynya. Primarily kept open by wind forcing (Barber and Massom, 2007) and secondarily maintained by strong currents (Loewen et al., 2020), the Roes Welcome Sound polynya is a region of increased water column mixing and convection. Hydrodynamics that form the polynya could have aided in mixing nearshore bottom waters directly affected by kelp production through the water column of nearshore stations (Stations 8, 10; bottom depths = ~40 m) and through the top ~40 m of Stations 7, 9, and 11 in Roes Welcome Sound, which all showed increased pH and lower pCO_2. Increased water column mixing also increases nutrient availability, leading to elevated phytoplankton primary production which consequently raises the pH, as discussed in Section 2.5.4. Indeed, it has been found that mixing and high nutrient availability west and north of the Island (Stations 10-14; Roes Welcome Sound, Repulse Bay, and Frozen Strait) in August 2019 promoted a phytoplankton bloom more productive than previously observed in Hudson Bay and Foxe Basin (Kitching, 2022). High primary production observed west and north of the Island (1428 ± 707 mg C m^{-2} d^{-1}; Kitching, 2022) was only comparable to rates previously estimated for Hudson Strait (1340 ± 140 mg C m^{-2} d^{-1}; Ferland et al., 2011), a region that is also characterized by strong mixing.

As explained in Section 2.7, AOU values provide an approximate measurement of cumulative aerobic remineralization in seawater since the water parcel was last at the surface (Sarmiento and Gruber, 2006). As seen in Figure 30, greatest apparent consumption of oxygen was observed at Station 22, suggesting strong respiration within the water column at that station. Similarly, AOU data showed signals of respiration in the bottom waters of Station 7 at the southern exit from Roes Welcome Sound, near bottom at Station 14 in Frozen Strait, in bottom waters of stations located south of the Island and in Foxe Basin/Channel. These interpretations are supported by DIC and pCO_2 data, with higher values found in bottom waters of these same stations, again suggesting respiration might have taken place there.

Waters tended to be more acidic with aragonite undersaturation below ~250 m at Station 16, below ~200 m at Station 18, and below ~60 m at Station 19 on the Foxe Basin/Channel side of

the Island, and in bottom waters of South Bay and Evans Strait, suggesting these waters could potentially be corrosive to marine calcifying organisms. These areas were additionally characterized by high pCO_2 and undersaturation in O_2, signifying that net respiration is likely responsible for the observed values in these areas. Relatively low pH, high pCO_2, and O_2-undersaturation, but not aragonite undersaturation, were also found through the whole water column at Stations 25 and 26 and near surface at Stations 3 and 23 south of the Island.

As previously briefly touched upon, in addition to AOU, biological contribution to the DIC pool is also evident through $\delta^{13}C_{DIC}$ results. During primary production, organic matter prefers the lighter ^{12}C isotope over the heavier ^{13}C isotope, consequently leaving the remaining DIC pool isotopically enriched, i.e., photosynthesis increases $\delta^{13}C_{DIC}$ (Sarmiento and Gruber, 2006). Respiration of isotopically light organic matter will then lower $\delta^{13}C_{DIC}$ values. Thus, with photosynthesis usually limited to the euphotic zone and respiration occurring through the whole water column, gradients in $\delta^{13}C_{DIC}$ from greater values at the surface to lower values near the bottom can be expected. Indeed, most stations sampled around Southampton Island showed this distribution expected from biological processes, with more enriched values in the top ~30 m suggesting net production and more depleted values below ~40 m indicating net respiration. Values of AOU were negative or near 0 µmol kg^{-1} where $\delta^{13}C_{DIC}$ was enriched, and AOU was large (>50 µmol kg^{-1}) in areas where $\delta^{13}C_{DIC}$ was depleted, further confirming respiration had taken place in these bottom waters. As also seen in Figure 39, there was a strong ($R^2 = 0.7629$) inverse correlation between $\delta^{13}C_{DIC}$ and AOU, with ^{13}C-enriched shallower waters having lower AOU, and ^{13}C-depleted, typically deeper, waters showing greater AOU. Certain stations (5, 6, 12, 25) which appeared to be better mixed than others (based on temperature and salinity distributions) showed intermediate values of $\delta^{13}C_{DIC}$ through their whole water column, meaning that $\delta^{13}C_{DIC}$ values at all depths at these stations were more depleted than surface values elsewhere and more enriched than bottom values at other stations, suggesting a net balance between production and respiration at these shallower, better-mixed stations.

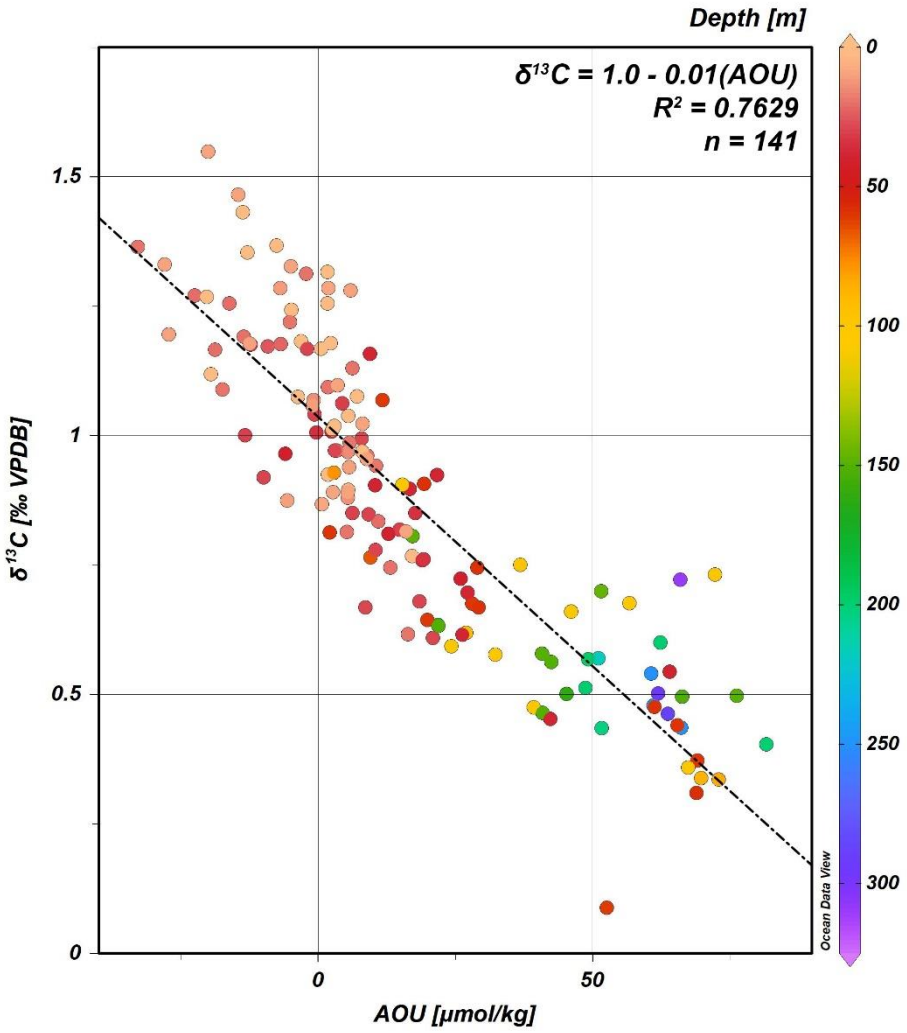

Figure 39. Stable carbon isotopic composition of dissolved inorganic carbon ($\delta^{13}C$) versus apparent oxygen utilization (AOU), with colour representing sample depth. Linear regression line, regression equation, and R^2 value are shown.

To better understand which processes could have been responsible for the DIC values observed during this study, deviations in the concentration and isotopic composition of DIC from values expected from conservative mixing between seawater, river water, and sea-ice melt were examined (Figure 40). Deviations from conservative mixing can be explained by one or more processes driving changes in concentration and isotopic composition of DIC. That is, each sample shown in Figure 40 can be explained by a unique net effect of loss of DIC by primary production, outgassing to the atmosphere, and $CaCO_3$ precipitation, and addition of DIC through $CaCO_3$ dissolution, atmospheric CO_2 uptake, and degradation of terrestrial and/or marine OC.

Since primary production and OC degradation vectors have the same slope in Figure 40, the individual effect of either cannot be quantified and it is only possible to see the net effect of the two processes. The same is true for CO_2 outgassing and uptake vectors, and $CaCO_3$ precipitation and dissolution vectors. No samples fell on the origin, indicating that no samples had the concentration and isotopic composition of DIC expected from conservative mixing alone. While most samples from the top ~50 m of the water column fell in proximity to the primary production vector and many deep water samples fell near the OC degradation vector, biological processes alone could not explain the data with the exception of a few samples that fell directly on either of the two vectors. CO_2 outgassing and/or $CaCO_3$ precipitation, which lower DIC with lesser isotopic fractionation than primary production, are required to explain samples that fell anywhere to the left of the primary production/OC degradation vectors in Figure 40. Likewise, either CO_2 uptake and/or $CaCO_3$ dissolution, which increase DIC with lesser isotopic fraction than OC degradation, are required to explain samples that fell to the right of the primary production/OC degradation vectors.

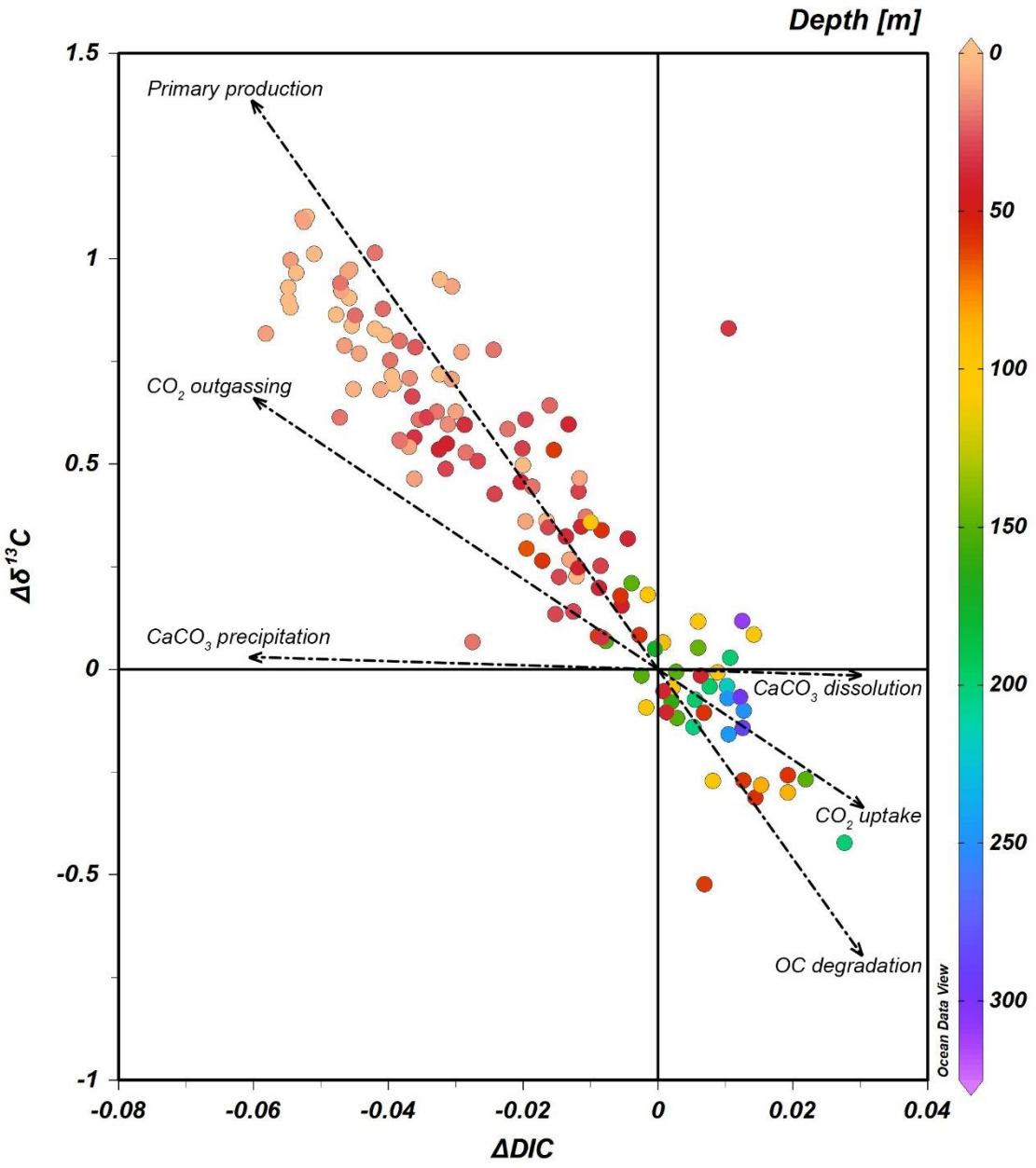

Figure 40. Deviations of stable carbon isotopic composition of dissolved inorganic carbon ($\Delta\delta^{13}C$) and dissolved inorganic carbon concentrations (ΔDIC) from values expected from conservative mixing between seawater, river water, and sea-ice meltwater. Colours represent depth of the sample. Samples with DIC and $\delta^{13}C$ expected from conservative mixing would fall on the origin (0,0). Calculated vectors demonstrate the effects of outgassing and uptake of CO_2 (slope = -11), primary production and degradation of organic carbon (OC) (slope = -23), and precipitation and dissolution of $CaCO_3$ (slope = -0.5) on the concentration and isotopic composition of DIC.

Chapter 6: Summary and Conclusion

This study used discrete samples collected during the August 2019 SIMEP cruise to characterize the inorganic carbon system in the Southampton Island region to understand the severity of ocean acidification and to identify the importance of physical and biological controls on the distribution of carbonate species. Salinity used in conjunction with $\delta^{18}O$-H_2O data allowed for a description of freshwater distribution in the water column. Highest fractions of SIM were found in surface waters in Foxe Basin/Channel that had experienced the most recent loss of sea ice, captured by satellite imagery. High fractions of MW were found in near-surface waters in Roes Welcome Sound, likely from Wager Bay outflow, and south of the Island. Considering the year-round low flows of Boas River discharging into Bay of Gods Mercy and Kirchoffer and Ford Rivers discharging into South Bay, it is unlikely that local freshwater sources could give rise to the observed high MW fractions (up to 0.10), so it was proposed that Hudson Bay's northwestern rivers contributed to the freshwater content in the region between Southampton and Coats Islands. The idea is supported by the circulation pattern proposed by Ridenour et al. (2019), who suggested that in spring and summer, surface currents move cyclonically from Roes Welcome Sound down to Churchill, Nelson, and Hayes River estuaries before returning to northwest Hudson Bay to pass between Southampton and Coats Islands. Further supporting the idea was the apparent MW end-member $\delta^{18}O$ value calculated for the study region (-11.1‰), which was within the range of $\delta^{18}O$ values previously determined for Churchill, Nelson, and Hayes Rivers (-12.71 - -10.81‰; Burt et al., 2016). Nutrients and TA data were used to demonstrate that there is little Atlantic seawater influence in the Southampton Island region.

Consistent with other studies in Hudson Bay (e.g., Azetsu-Scott et al., 2014; Burt et al., 2016), the distributions of DIC and TA in the Southampton Island waters mimicked those of salinity, with lower values observed in fresher surface waters and higher DIC and TA values found in high salinity, low temperature bottom waters across most stations. A strong role of temperature variation in influencing variation in pCO_2 was observed at stations at the northern and southern ends of Roes Welcome Sound, in South Bay, and in Frozen, Fisher, and Evans Straits, as temperature normalization greatly changed surface pCO_2 values (by up to ~91 µatm). However, the role of physical controls, such as changes in seawater temperature or salinity, on pCO_2 saturation states were not straightforward, as pCO_2 was not strongly correlated with either temperature or salinity. Regionally high pH was observed in the top ~50 m in Foxe

Basin/Channel and Roes Welcome Sound, near surface in Repulse Bay, at ~20 m in Frozen Strait, and near the bottom at the northern entrance to Roes Welcome Sound. These areas also had lower values of pCO_2, were generally oversaturated in O_2, and had enriched values of $\delta^{13}C_{DIC}$, all pointing to primary production likely being the cause of the observed values.

More acidic, aragonite-undersaturated, and thus potentially corrosive, waters were found below ~250 m at Station 16, below ~200 m at Station 18, and below ~60 m at Station 19 in Foxe Basin/Channel, and in bottom waters of South Bay and Evans Strait. These areas were also high in pCO_2 and undersaturated in O_2, signifying that net respiration had likely produced the observed values. Net respiration had also likely occurred through the whole water column at Stations 25 and 26 and near surface at Stations 3 and 23, all south of the Island, as these waters were also low in pH, high in pCO_2, and undersaturated in O_2, however these waters were not undersaturated in aragonite. Majority of stations showed the $\delta^{13}C_{DIC}$ distribution expected from biological processes, with more enriched values in the top ~30 m suggesting net production and more depleted values below ~40 m indicating net respiration. AOU was also large, in excess of 50 µmol kg^{-1}, in areas where $\delta^{13}C_{DIC}$ was depleted, further confirming respiration had taken place in these bottom waters. Examination of deviations in the concentration and isotopic composition of DIC from values expected from conservative mixing between seawater, river water, and sea-ice melt revealed that while primary production and respiration appear to be the dominant processes controlling the concentration and isotopic composition of DIC in the Southampton Island region, the data still cannot be explained by any single process alone, highlighting the importance of metabolic processes, freshwater inputs, and air-sea gas exchange in governing the DIC pool in this region.

This study was an important step toward a better understanding of the oceanography of Southampton Island waters, which have received little attention until the recent years. It will also be a valuable contribution toward the development of a management plan for the Southampton Island area, which is an ecologically and biologically significant region with large marine mammal and seabird populations (Yurkowski et al., 2018), which has also been identified as an Area of Interest and is currently in the process of being established as a Marine Protected Area by Fisheries and Oceans Canada (Loewen et al., 2020). The Hudson Bay Complex will continue to undergo climate-related changes into the future. With increasing precipitation and river runoff,

the freshwater fractions in the Southampton Island near-surface waters will increase, making these waters more susceptible to acidification. This is of particular concern in South Bay and Fisher and Evans Straits surface waters, which are characterized by high fractions of MW and which are already seeing low values of pH and Ω_{ar}. With greater volumes of runoff from land to sea, there would be increases in the fluxes of nutrients, which increase primary production, leading to increases in pH. There would also be associated increases in fluxes of organic matter and sediment, which increase turbidity and reduce light penetration into the water column, thereby reducing rates of photosynthesis and increasing respiration, in turn leading to greater acidification. It is uncertain what overall effect these climate-related changes will have in the Southampton Island region, and whether the role of biological processes on the carbonate system in this area will strengthen or weaken.

To understand how climate change is impacting the region, future studies should monitor the changes in extent of aragonite undersaturation in bottom waters in Foxe Basin/Channel, Evans Strait, and South Bay via the deployment of moorings equipped with sensors capable of monitoring temperature, salinity, dissolved oxygen, and pH at multiple depths throughout the water column. In addition to showing interannual changes, mooring data would also shed light on how the physical characteristics of the water column and the extent of aragonite undersaturation change seasonally. Community-based monitoring out of Coral Harbour (Salliq) could be used to augment mooring data to monitor pH, Ω_{ar}, and fractions of freshwater in surface waters south of the Island that appear to be particularly susceptible to acidification. This community-based monitoring could involve regular salinity and temperature profiles by CTDs, and collection of discrete samples for salinity, $\delta^{18}O$, pH, DIC, and TA in areas accessible by small boats. Considering the ecological and biological importance of the Southampton Island region, oceanographic monitoring is a necessary next step after the establishment of a reference for which to compare by the 2019 SIMEP cruise.

References

Ahmed, M.M.M., Else, B.G.T., Butterworth, B., Capelle, D.W., Guéguen, C., Miller, L.A., Meilleur, C., & Papakyriakou, T. (2021). Widespread surface water pCO_2 undersaturation during ice-melt season in an Arctic continental shelf sea (Hudson Bay, Canada). *Elementa: Science of the Anthropocene, 9*(1).

Ahmed, M.M.M., Else, B.G.T., Capelle, D., Miller, L.A., & Papakyriakou, T. (2020). Underestimation of surface pCO_2 and air-sea CO_2 fluxes due to freshwater stratification in an Arctic shelf sea, Hudson Bay. *Elementa: Science of the Anthropocene, 8*.

Alling, V., Porcelli, D., Mörth, C.-M., Anderson, L.G., Sanchez-Garcia, L., Gustafsson, Ö., Andersson, P.S., & Humborg, C. (2012). Degradation of terrestrial organic carbon, primary production and out-gassing of CO_2 in the Laptev and East Siberian Seas as inferred from $\delta^{13}C$ values of DIC. Geochimica et Cosmochimica Acta, 95, 143–159.

AMAP. (2013). AMAP Assessment 2013: Arctic Ocean Acidification. Arctic Monitoring and Assessment Programme (AMAP), Oslo, Norway, 99 pp.

AMAP. (2017). Snow, Water, Ice and Permafrost in the Arctic (SWIPA) 2017. Arctic Monitoring and Assessment Programme (AMAP), Oslo, Norway, 269 pp.

Armstrong, C.W., Foley, N.S., Slagstad, D., Chierici, M., Ellingsen, I., & Reigstad, M. (2019). Valuing blue carbon changes in the Arctic Ocean. *Frontiers in Marine Science, 6.*

Azetsu-Scott, K., Clarke, A., Falkner, K., Hamilton, J., Jones, E.P., Lee, C., … Yeats, P. (2010). Calcium carbonate saturation states in the waters of the Canadian Arctic Archipelago and the Labrador Sea. *Journal of Geophysical Research Atmospheres, 115*, C11021.

Azetsu-Scott, K., Petrie, B., Yeats, P., & Lee, C. (2012). Composition and fluxes of freshwater through Davis Strait using multiple chemical tracers. *Journal of Geophysical Research, 117*(C12011).

Azetsu-Scott, K., Starr, M., Mei, Z.P., & Granskog, M. (2014). Low calcium carbonate saturation state in an Arctic inland sea having large and varying fluvial inputs: The Hudson Bay system. *Journal of Geophysical Research: Ocean, 119,* 6210-6220.

Babb, D.G., Kirillov, S., Kuzyk, Z.Z., Netser, T., Liesch, J., Kamula, C.M., Zagon, T., Barber, D.G., & Ehn, J. K. (2022). On the intermittent formation of an ice bridge (Nunniq) across Roes Welcome Sound, Northwestern Hudson Bay, and its use to local Inuit hunters. *Arctic, 75*(2), 198-224.

Barber, D.G., & Massom, R.A. (2007). The role of sea ice in Arctic and Antarctic polynyas. In W.O. Smith and D.G. Barber (Eds.), *Polynyas: Windows to the World* (pp. 1–43). Amsterdam: Elsevier.

Barrón, C., & Duarte, C.M. (2015). Dissolved organic carbon pools and export from the coastal ocean. *Global Biogeochemical Cycles, 29,* 1725–1738.

Bird, J.B. (1953). *Southampton Island. Canada Department of Mines and Technical Surveys, Geographical Branch, Memoir 1*. Ottawa, ON: Queen's Printer. Viii + 84 p.

Broecker, W.S., & Peng, T.-H. (1982). *Tracers in the sea*. Palisades, NY: Lamont-Doherty Geological Observatory, Columbia University.

Bruneau, J., Babb, D., Chan, W., Kirillov, S., Ehn, J., Hanesiak, J., & Barbed, D.G. (2021). The ice factory of Hudson Bay: Spatiotemporal variability of the Kivalliq Polynya. *Elementa: Science of the Anthropocene, 9*(1).

Budgell, W.P. (1976). Tidal propagation in Chesterfield Inlet, N.W.T. Ocean and Aquatic Sciences Central Region. Manuscript Report Series No. 3, 99 p. Retrieved from https://waves-vagues.dfo-mpo.gc.ca/Library/79586.pdf

Burt, W.J., Thomas, H., Miller, L.A., Granskog, M.A., Papakyriakou, T.N., & Pengelly, L. (2016). Inorganic carbon cycling and biogeochemical processes in an Arctic inland sea (Hudson Bay). *Biogeosciences, 13*, 4659–4671.

Campbell, N.J. (1959). Some oceanographic features of northern Hudson Bay, Foxe Channel, and Hudson Strait. Fish. Res. Bd. Can. Manuscr. Rep. Ser. 46, 49 p.

Carmack, E., Winsor, P., & Williams, W. (2015). The contiguous panarctic Riverine Coastal Domain: A unifying concept. *Progress in Oceanography, 139,* 13–23.

Carmack, E.C., Yamamoto-Kawai, M., Haine, T.W.N., Bacon, S., Bluhm, B.A., Lique, C., …Williams, W.J. (2016). Freshwater and its role in the Arctic Marine System: Sources, disposition, storage, export, and physical and biogeochemical consequences in the Arctic and global oceans. *Journal of Geophysical Research: Biogeosciences, 121,* 675–717.

Carrillo, C.J., Smith, R.C., & Karl, D.M. (2004). Processes regulating oxygen and carbon dioxide in surface waters west of the Antarctic Peninsula. *Marine Chemistry, 84*, 161–179.

Castro de la Guardia, L., Filbee-Dexter, K., Reimer, J., MacGregor, K.A., Garrido, I., Singh, R. K., Bélanger, S., Konar, B., Iken, K., Johnson, L.E., Archambault, P., Sejr, M.K., Søreide, J.E., & Mundy, C.J. (2023). Increasing depth distribution of Arctic kelp with increasing number of open water days with light. *Elementa: Science of the Anthropocene, 11*(1).

CIS. (2016). Seasonal summary, North American Arctic waters, spring 2016. 10 p. (Accessed 29 September 2017).

CliC/AMAP/IASC. (2016). The Arctic freshwater system in a changing climate. WCRP Climate and Cryosphere (CliC) Project, Arctic Monitoring and Assessment Programme (AMAP), International Arctic Science Committee (IASC).

Dansgaard, W. (1965). Stable isotopes in precipitation. *Tellus, 16*(4), 436–468.

Defossez, M., Saucier, F.J., Myers, P.G., Caya, D., & Dumais, J.-F. (2008). Multi-year observations of deep water renewal in Foxe Basin, Canada. *Atmosphere-Ocean, 46*(3), 377–390.

Defossez, M., Saucier, F.J., Myers, P.G., Caya, D., & Dumais, J.-F. (2010). Analysis of a dense water pulse following mid-winter opening of polynyas in western Foxe Basin, Canada. *Dynamics of Atmospheres and Oceans, 49*, 54–74.

Déry, S.J., Mlynowski, T.J., Hernández-Henríquez, M.A., & Straneo, F. (2011). Interannual variability and interdecadal trends in Hudson Bay streamflow. *Journal of Marine Systems, 88*(3), 341-351.

Déry, S.J., Stadnyk, T.A., MacDonald, M.K., & Gauli-Sharma, B. (2016). Recent trends and variability in river discharge across northern Canada. *Hydrology and Earth System Sciences, 20*, 4801–4818.

Déry, S.J., Stieglitz, M., McKenna, E.C., & Wood, E.F. (2005). Characteristics and trends of river discharge into Hudson, James, and Ungava Bays, 1964–2000. *Journal of Climate, 18*, 2540–2557.

Dickson, A.G. (1990). Thermodynamics of the dissociation of boric acid in synthetic seawater from 273.15 to 318.15 K. *Deep Sea Research, 37*(5), 755–766.

Dickson, A.G., Sabine, C.L., & Christian, J.R. (Eds.). (2007). Guide to best practices for ocean CO_2 measurements. *PICES Special Publication 3*, 191 pp.

Duarte, C.M. (2017). Reviews and syntheses: Hidden forests, the role of vegetated coastal habitats in the ocean carbon budget. *Biogeosciences, 14*, 301–310.

Duarte, C.M., & Cebrian, J. (1996). The fate of marine autotrophic production. *Limnology and Oceanography, 41*, 1758–1766.

Duarte, C.M., Hendriks, I.E., Moore, T.S., Olsen, Y.S., Steckbauer, A., Ramajo, L., Carstensen, J., Trotter, J.A., & McCulloch, M. (2013). Is ocean acidification an open-ocean syndrome? Understanding anthropogenic impacts on seawater pH. *Estuaries and Coasts, 36*, 221–236.

Duarte, C.M., Middelburg, J.J., Caraco, N. (2005) Major role of marine vegetation on the oceanic carbon cycle. *Biogeosciences, 2*, 1–8.

ECCC. (2021). *CO_2 CHL surface – in situ ECCC data*. Retrieved May 6, 2022, from https://gaw.kishou.go.jp/search/file/0020-4004-1001-01-01-9999

ECCC. (2022). Archived hydrometric data (HYDAT). Water Survey of Canada. Retrieved May 15, 2022 from https://wateroffice.ec.gc.ca/

ECCC-MSC. (2022). *Hourly Data Report for August 01, 2019*. Retrieved May 5, 2022, from https://climate.weather.gc.ca/climate_data/

Eckman, J.E., Duggins, D.O., Sewell, A.T. (1989). Ecology of under story kelp environments. I. Effects of kelps on flow and particle transport near the bottom. *Journal of Experimental Marine Biology and Ecology, 129*, 173–187.

Else, B.G.T., Papakyriakou, T.N., Galley, R.J., Mucci, A., Gosselin, M., Miller, L.A., Shadwick, E.H., & Thomas, H. (2012). Annual cycles of pCO_{2sw} in the southeastern Beaufort Sea: New understandings of air-sea CO_2 exchange in arctic polynya regions. *Journal of Geophysical Research, 117*:C00G13.

Else, B.G.T., Papakyriakou, T.N., Granskog, M.A., & Yackel, J.J. (2008a). Observations of sea surface fCO_2 distributions and estimated air–sea CO_2 fluxes in the Hudson Bay region

(Canada) during the open water season. *Journal of Geophysical Research: Oceans, 113*(C8), C08026.

Else, B.G.T., Yackel, J.J., & Papakyriakou, T.N. (2008b). Application of satellite remote sensing techniques for estimating air-sea CO_2 fluxes in Hudson Bay, Canada during the ice-free season. *Remote Sensing of Environment, 112*(9), 3550–3562.

Emerson, S.R., & Hedges, J.I. (2008). *Chemical oceanography and the marine carbon cycle*. Cambridge, UK: Cambridge University Press.

Erlenkeuser, H., Cordt, H.H., Simstich, J., Bauch, D., & Spielhagen, R.F. (2003). DIC stable carbon isotope pattern in the surface waters of the southern Kara Sea, September 2000. In R. Stein, K. Fahl, D.K. Fütterer, E.M. Galimov & O.V. Stepanets (Eds.), *Siberian river run-off in the Kara Sea* (pp. 281–307). Amsterdam, Netherlands: Elsevier Science.

Ferland, J., Gosselin, M., & Starr, M. (2011). Environmental control of summer primary production in the Hudson Bay system: The role of stratification. *Journal of Marine Systems, 88*(3), 385-400.

Filbee-Dexter, K., MacGregor, K.A., Lavoie, C., Garrido, I., Goldsmit, J., Castro de la Guardia, L., Howland, K.L., Johnson, L.E., Konar, B., McKindsey, C.W., Mundy, C.J., Schlegel, R.W., & Archambault, P. (2022). Sea ice and substratum shape extensive kelp forests in the Canadian Arctic. *Frontiers in Marine Science, 9*(754074).

Firke, S. (2021). janitor: Simple Tools for Examining and Cleaning Dirty Data. R package version 2.1.0. https://CRAN.R-project.org/package=janitor

Gagnon, A.S., & Gough, W.A. (2006). East-west asymmetry in long-term trends of landfast ice thickness in the Hudson Bay region, Canada. *Climate Research, 32*, 177–186.

Garcia, H.E., & Gordon, L.I. (1992). Oxygen solubility in seawater: Better fitting equations. *Limnology and Oceanography, 37*(6), 1307–1312.

Garcia, H.E., & Gordon, L.I. (1993). Erratum: Oxygen solubility in seawater: Better fitting equations. *Limnology and Oceanography, 38*(3), 656.

Gattuso, J.-P., & Hansson, L. (2011). *Ocean acidification*. Oxford, England: Oxford University Press.

Gran, G. (1952). Determination of the equivalence point in potentiometric titration. *Analyst Part II, 77*, 661–671.

Granskog, M.A., Kuzyk, Z.Z.A., Azetsu-Scott, K., & Macdonald, R.W. (2011). Distributions of runoff, sea-ice melt and brine using $\delta^{18}O$ and salinity data – A new view on freshwater cycling in Hudson Bay. *Journal of Marine Systems, 88*, 362–374.

Granskog, M.A., Macdonald, R.W., Kuzyk, Z.Z.A., Senneville, S., Mundy, C.J., Barber, D.G., Stern, G.A., & Saucier, F. (2009). Coastal conduit in southwestern Hudson Bay (Canada) in summer: Rapid transit of freshwater and significant loss of colored dissolved organic matter. *Journal of Geophysical Research, 114*(C08012).

Graven, H., Keeling, R.F., & Rogelj, J. (2020). Changes to carbon isotopes in atmospheric CO_2 over the industrial era and into the future. *Global Biogeochemical Cycles, 34*, e2019GB006170.

Grolemund, G., & Wickham, H. (2011). Dates and Times Made Easy with lubridate. *Journal of Statistical Software, 40*(3), 1-25.

Guy, R.D., Fogel, M.L., & Berry, J.A. (1993). Photosynthetic fractionation of stable isotopes of oxygen and carbon. *Plant Physiology, 101*, 37–47.

Hester, J., & Wickham, H. (2020). fs: Cross-Platform File System Operations Based on 'libuv'. R package version 1.5.0. https://CRAN.R-project.org/package=fs

Hoefs, J. (2009). *Stable isotope geochemistry*, 6th Ed. Berlin, Germany: Springer-Verlag Berlin Heidelberg.

Holm-Hansen, O., Lorenzen, C.J., Holmes, R.W., & Strickland, J.D.H. (1965). Fluorometric determination of chlorophyll. ICES Journal of Marine Science, 30(1), 3-15.

Hullar, M., Fry, B., Peterson, B., & Wright, R. (1996). Microbial utilization of estuarine dissolved organic carbon: A stable isotope tracer approach tested by mass balance. *Applied and Environmental Microbiology, 62,* 2489–2493.

IAEA. (2001). GNIP Maps and Animations, International Atomic Energy Agency, Vienna. Accessible at https://www.iaea.org/

Ingram, R.G., & Prinsenberg, S. (1998). Coastal oceanography of Hudson Bay and surrounding eastern Canadian Arctic waters. In A.R. Robinson & K.H. Brink (Eds.), *The sea, the global coastal ocean, processes and methods* (pp. 835-861). New York, NY: Wiley.

Inoue, H., & Sugimura, Y. (1985). Carbon isotopic fractionation during the CO_2 exchange process between air and sea water under equilibrium and kinetic conditions. *Geochimica et Cosmochimica Acta, 49*, 2453–2460.

IPCC. (2011). Workshop Report of the Intergovernmental Panel on Climate Change Workshop on Impacts of Ocean Acidification on Marine Biology and Ecosystems. Field, C.B., V. Barros, T.F. Stocker, D. Qin, K.J. Mach, G.-K. Plattner, M.D. Mastrandrea, M. Tignor and K.L. Ebi (Eds.). Intergovernmental Panel on Climate Change, Working Group II Technical Support Unit, 164 pp.

Jacquemot, L., Vigneron, A., Tremblay, J.-É., & Lovejoy, C. (2022). Contrasting sea ice conditions shape microbial food webs in Hudson Bay (Canadian Arctic). *ISME Communications, 2,* 104.

Johnson, K.M., Wills, K.D., Butler, D.B., Johnson, W.K., & Wong, C.S. (1993). Coulometric total carbon dioxide analysis for marine studies: Maximizing the performance of an automated gas extraction system and coulometric detector. *Marine Chemistry, 44*, 167–187.

Jones, E.P., & Anderson, L.G. (1994). Northern Hudson Bay and Foxe Basin: Water masses, circulation and productivity. *Atmosphere-Ocean, 32*(2), 361–374.

Jones, E.P., Anderson, L.G., Jutterström, S., Mintrop, L., & Swift, J.H. (2008). Pacific freshwater, river water and sea ice meltwater across Arctic Ocean basins: Results from the 2005 Beringia Expedition. *Journal of Geophysical Research, 113*(C08012).

Kamula, M., Masiuk, B., Regular, K., Cote, D., Huyghe, S., Mercuri, J., Friscourt, N., & Van Velzen, R. (2016). F.R.V Nuliajuk Science Cruise Report: Chesterfield Inlet and Wager Bay (Ukkusiksalik National Park) Marine Baseline Study. Retrieved from http://hdl.handle.net/1993/34323

Kelley, D., & Richards, C. (2021). Oce: Analysis of Oceanographic Data. R package version 1.4-0. https://CRAN.R-project.org/package=oce

Kiddon, J., Bender, M.L., & Orchardo, J. (1993). Isotopic fractionation of oxygen by respiring marine organisms. *Global Biogeochemical Cycles, 7*(3), 679–694.

Kitching, E. (2022). *Physical processes driving phytoplankton production around Southampton Island, Nunavut in late summer 2018 and 2019* [Master's thesis, University of Manitoba]. MSpace. http://hdl.handle.net/1993/36865

Kitidis, V., Upstill-Goddard, R. C., & Anderson, L. G. (2010). Methane and nitrous oxide in surface water along the North-West Passage, Arctic Ocean. *Marine Chemistry, 121*, 80–86.

Krause-Jensen, D., & Duarte, C.M. (2016). Substantial role of macroalgae in marine carbon sequestration. *Nature Geoscience, 9,* 737–742.

Krause-Jensen, D., Lavery, P., Serrano, O., Marbà, N., Masque, P., & Duarte, C.M. (2018). Sequestration of macroalgal carbon: The elephant in the Blue Carbon room. *Biology Letters, 14,* 20180236.

Kuzyk, Z.A., & Candlish, L.M. (2019). *From Science to Policy in the Greater Hudson Bay Marine Region: An Integrated Regional Impact Study (IRIS) of Climate Change and Modernization*. ArcticNet, Québec City, 424 pp.

Kuzyk, Z.Z., Macdonald, R.W., Johannessen, S.C., Gobeil, C., & Stern, G.A. (2009). Towards a sediment and organic carbon budget for Hudson Bay. *Marine Geology, 264*(3-4), 190–208.

LaFlamme, C., McFarlane, C.R.M., Corrigan, D., & Wodicka, N. (2014). Origin and tectonometamorphic history of the Repulse Bay block, Melville Peninsula, Nunavut: exotic terrane or deeper level of the Rae craton? *Canadian Journal of Earth Sciences, 51*, 1097–1122.

Lammers, R.B., Shiklomanov, A.I., Vörösmarty, C.J., Fekete, B.M., & Peterson, B.J. (2001). Assessment of contemporary Arctic river runoff based on observational discharge records. *Journal of Geophysical Research, 106*(D4), 3321–3334.

Landy, J.C., Ehn, J.K., Babb, D.G., Thériault, N., & Barber, D.G. (2017). Sea ice thickness in the Eastern Canadian Arctic: Hudson Bay Complex & Baffin Bay. *Remote Sensing of Environment, 200*, 281–294.

Lapoussière, A., Michel, C., Gosselin, M., & Poulin, M. (2009). Spatial variability in organic material sinking export in the Hudson Bay system, Canada, during fall. *Continental Shelf Research, 29,* 1276–1288.

Lapoussière, A., Michel, C., Gosselin, M., Poulin, M., Martin, J., & Tremblay, J.-É. (2013). Primary production and sinking export during fall in the Hudson Bay system, Canada. *Continental Shelf Research, 52,* 62–72.

Lavoie, D., Pinet, N., Dietrich, J., Zhang, S., Hu, K., Asselin, E., …Roberts, B. (2013). Geological framework, basin evolution, hydrocarbon system data and conceptual hydrocarbon plays for the Hudson Bay and Foxe basins, Canadian Arctic. Geol. Surv. Can. Open File 7363: 210 p. doi:10.4095/293119

Lee, K., Kim, T.-W., Byrne, R.H., Millero, F.J., Feely, R.A., & Liu, Y.-M. (2010). The universal ratio of boron to chlorinity for the North Pacific and North Atlantic oceans. *Geochimica et Cosmochimica Acta, 74*(6), 1801–1811.

Libes, S. (2009). *Introduction to marine biogeochemistry,* 2nd Ed. Burlington, MA: Elsevier Inc.

Loewen, T. N., Hornby, C.A., Johnson, M., Chambers, C., Dawson, K., MacDonell, D., Bernhardt, W., Gnanapragasam, R., Pierrejean, M., & Choy, E. (2020). Ecological and Biophysical Overview of the Southampton proposed Area of Interest for the Southampton Island Ecologically and Biologically Significant Area. DFO Can. Sci. Advis. Sec. Res. Doc. 2020/032. vi + 96 p.

Loose, B., McGillis, W.R., Schlosser, P., Perovich, D., & Takahashi, T. (2009). Effects of freezing, growth, and ice cover on gas transport processes in laboratory seawater experiments. *Geophysical Research Letters, 36*(L05603).

Loose, B., Miller, L.A., Elliott, S., & Papakyriakou, T. (2011). Sea ice biogeochemistry and material transport across the frozen interface. *Oceanography, 24,* 202-218.

Lueker, T.J., Dickson, A.G., & Keeling, C.D. (2000). Ocean pCO_2 calculated from dissolved inorganic carbon, alkalinity, and equations for K_1 and K_2: validation based on laboratory measurements of CO_2 in gas and seawater at equilibrium. *Marine Chemistry, 70,* 105-119.

Lynch-Stieglitz, J., Stocker, T.F., Broecker, W.S., & Fairbanks, R.G. (1995). The influence of air-sea exchange on the isotopic composition of oceanic carbon: Observations and modeling. *Global Biogeochemical Cycles, 9*(4), 653–665.

Majoube, M. (1971). Fractionnement en oxygene-18 et en deuterium entre l'eau et sa vapeur. *Journal de Chimie Physique, 58,* 1423–1436.

Markham, W.E. (1981). Ice Atlas - Canadian Arctic Waterways. Ottawa, ON: Environment Canada.

McCrystall, M.R., Stroeve, J., Serreze, M., Forbes, B.C., & Screen, J.A. (2021). New climate models reveal faster and larger increases in Arctic precipitation than previously projected. *Nature Communications, 12,* 6765.

McGeehan, T., & Maslowski, W. (2012). Evaluation and control mechanisms of volume and freshwater export through the Canadian Arctic Archipelago in a high-resolution pan-Arctic ice-ocean model. *Journal of Geophysical Research: Oceans, 117*(C8).

Middelboe, A.L., & Hansen, P.J. (2007). High pH in shallow-water macroalgal habitats. *Marine Ecology Progress Series, 338,* 107–117.

Millero, F.J. (2013). *Chemical oceanography,* 4th Ed. Boca Raton, FL: Taylor & Francis Group.

Müller, K. (2020). here: A Simpler Way to Find Your Files. R package version 1.0.1. https://CRAN.R-project.org/package=here

NASA. (n.d.). *EOSDIS Worldview.* Retrieved from https://worldview.earthdata.nasa.gov/

Norrman, B., Zweifel, U.L., Hopkinson, C.S., & Fry, B. (1995). Production and utilization of dissolved organic carbon during an experimental diatom bloom. *Limnology and Oceanography, 40,* 898–907.

O'Neil, J. R. (1968). Hydrogen and oxygen isotope fractionation between ice and water. *Journal of Physical Chemistry, 72,* 3683-3684.

Orr, J.C., Fabry, V.J., Aumont, O., Bopp, L., Doney, S.C., Feely, R.A., … Yool, A. (2005). Anthropogenic ocean acidification over the twenty-first century and its impact on calcifying organisms. *Nature, 437,* 681-686.

Östlund, H. G., & Hut, G. (1984). Arctic Ocean water mass balance from isotope data. *Journal of Geophysical Research - Oceans, 89*(NC4), 6373-6381.

Pedersen, T.L. (2020). patchwork: The Composer of Plots. R package version 1.1.1. https://CRAN.R-project.org/package=patchwork

Perez F.F., & Fraga F. (1987). Association constant of fluoride and hydrogen ions in seawater. *Marine Chemistry, 21*(2), 161-168.

Pierrot, D., Epitalon, J.-M., Orr, J.C., Lewis, E., and Wallace, D.W.R. (2021). MS Excel program developed for CO_2 system calculations – version 3.0. GitHub repository, https://github.com/dpierrot/co2sys_xl

Pierrot, D., Neill, C., Sullivan, K., Castle, R., Wanninkhof, R., Lüger, H., . . . Cosca, C. E. (2009). Recommendations for autonomous underway pCO_2 measuring systems and data-reduction routines. *Deep Sea Research Part II, 56*(8-10), 512-522.

Prinsenberg, S. (1986a). On the physical oceanography of Foxe Basin. In I.P. Martini (Ed.), *Canadian Inland Seas* (pp. 217–236). Amsterdam: Elsevier.

Prinsenberg, S. (1986b). The circulation pattern and current structure of Hudson Bay. In I.P. Martini (Ed.), *Canadian inland seas* (pp. 187-204). Amsterdam: Elsevier.

Prinsenberg, S. (1988). Ice-cover and ice-ridge contributions to the freshwater contents of Hudson Bay and Foxe Basin. *Arctic, 41*(1), 6-11.

Qi, D., Ouyang, Z., Chen, L., Wu, Y., Lei, R., Chen, B.,… Cai, W.-J. (2022). Climate change drives rapid decadal acidification in the Arctic Ocean from 1994 to 2020. *Science, 377*(6614), 1544–1550.

Rau, G.H., Riebesell, U., & Wolf-Gladrow, D. (1996). A model of photosynthetic ^{13}C fractionation by marine phytoplankton based on diffusive molecular CO_2 uptake. *Marine Ecology Progress Series, 133,* 275–285.

Redfield, A.C., Ketchum, B.H., & Richards, F.A. (1963). The influence of organisms on the composition of sea-water. In M. Hill (Ed.), *The Sea* (pp. 26–77). New York: Interscience Publishers.

Ridenour, N. A., Hu, X., Sydor, K., Myers, P. G., & Barber, D. G. (2019). Revisiting the circulation of Hudson Bay: Evidence for a seasonal pattern. *Geophysical Research Letters, 46,* 3891–3899.

Rosman, J.H., Koseff, J.R., Monismith, S.G., & Grover, J. (2007). A field investigation into the effects of a kelp forest (*Macrocystis pyrifera*) on coastal hydrodynamics and transport. *Journal of Geophysical Research: Oceans, 112*, C02016.

Rysgaard, S., Bendtsen, J., Delille, B., Dieckmann, G.S., Glud, R.N., Kennedy, H., Mortensen, J., Papadimitriou, S., Thomas, D.N., & Tison, J.-L. (2011). Sea ice contribution to the air-sea CO_2 exchange in the Arctic and Southern Oceans. *Tellus, 63B,* 823-830.

Sadler, H.E. (1982). Water flow into Foxe Basin through Fury and Hecla Strait. *Le Naturaliste Canadien, 109,* 701–707.

Sanborn-Barrie, M., Chakungal, J., James, D.T., Rayner, N., & Whalen, J.B. (2014). Precambrian bedrock geology, Southampton Island, Nunavut. Geol. Surv. Can. Canadian Geoscience Map 132, scale 1:250 000. doi:10.4095/293328.

Sarmiento, J.L., & Gruber, N. (2006). *Ocean biogeochemical dynamics*. Princeton, NJ: Princeton University Press.

Saucier, F., Senneville, S., Prinsenberg, S., Roy, F., Smith, G., Gachon, P., Caya, D., & Laprise, R. (2004). Modelling the sea ice-ocean seasonal cycle in Hudson Bay, Foxe Basin and Hudson Strait, Canada. *Climate Dynamics, 23*(3-4), 303-326.

Saunders, P. (1990). The International Temperature Scale of 1990, ITS-90. *WOCE Newsletter 10*.

Schlitzer, R. (2021). Ocean Data View. https://odv.awi.de

Sea-Bird Electronics. (2016). *SBE 19plus V2 SeaCAT Profiler CTD, Manual version 013.* Washington, USA: Sea-Bird Electronics.

Sea-Bird Scientific. (2022). *SBE 43 Dissolved oxygen sensor, Datasheet.* Washington, USA: Sea-Bird Scientific.

Sibert, V., Zakardjian, B., Gosselin, M., Starr, M., Senneville, S., & LeClainche, Y. (2011). 3D bio-physical model of the sympagic and planktonic productions in the Hudson Bay system. *Journal of Marine Systems, 88*(3), 401–422.

Smith, S.V. (1981). Marine macrophytes as a global carbon sink. *Science, 211,* 838–840.

Spiker, E. (1980). The behavior of ^{14}C and ^{13}C in estuarine water: Effects of in situ CO_2 production and atmospheric change. *Radiocarbon, 22*(3), 647-654.

St-Laurent, P., Straneo, F., Dumais, J.-F., & Barber, D.G. (2011). What is the fate of the river waters of Hudson Bay? *Journal of Marine Systems, 88,* 352–361.

Steinacher, M., Joos, F., Frolicher, T.L., Plattner, G.-K., & Doney, S.C. (2009). Imminent ocean acidification in the Arctic projected with the NCAR global coupled carbon cycle-climate model. *Biogeosciences, 6,* 515-533.

Stewart, D.B., & Barber, D.G. (2010). The Ocean-Sea Ice-Atmosphere System of the Hudson Bay Complex. In S.H. Ferguson, L.L. Loseto, & M.L. Mallory (Eds.), *A little less Arctic: Top predators in the world's largest northern inland sea, Hudson Bay.* Dordrecht, the Netherlands: Springer.

Stewart, D.B., & Howland, K.L. (2009). An ecological and oceanographical assessment of the alternate ballast water exchange zone in the Hudson Strait Region. DFO Can. Sci. Advis. Sec. Res. Doc. 2009/008. vi + 92 p

Stewart, D.B., & Lockhart, W.L. (2005). An overview of the Hudson Bay marine ecosystem. Can. Tech. Rep. Fish. Aquat. Sci. 2586. vi + 487 p.

Straneo, F., & Saucier, F.J. (2008). The Arctic-subarctic exchange through Hudson Strait. In R.R. Dickson, J. Meincke & P. Rhines (Eds.), *Arctic-Subarctic Ocean fluxes: Defining the role of the Northern Seas in Climate* (pp. 249–261). Dordrecht: Springer.

Suzuoki, T., & Kimura, T. (1973). D/H and 18O/16O fractionation in ice-water system. *Journal of Mass Spectrometry, 21,* 229–233.

Takahashi, T., Olafsson, J., Goddard, J.G., Chipman, D.W., & Sutherland, S.C. (1993). Seasonal-variation of CO_2 and nutrients in the high-latitude surface oceans – a comparative study. *Global Biogeochemical Cycles, 7*(4), 843-878.

Takahashi, T., Sutherland, S.C., Sweeney, C., Poisson, A., Metzl, N., Tilbrook, B.,… Nojiri, Y. (2002). Global sea-air CO_2 flux based on climatological surface ocean pCO_2, and seasonal biological and temperature effects. *Deep-Sea Research II, 49,* 1601–1622.

Tan, F.C., & Strain, P.M. (1996). Sea ice oxygen isotopes in Foxe Basin, Hudson Bay and Hudson Strait, Canada. *Journal of Geophysical Research, 101*(C9), 20869–20876.

Volk, T., & Hoffert, M.I. (1985). Ocean carbon pumps: Analysis of relative strengths and efficiencies in ocean-driven atmospheric CO_2 changes. *Geophysical Monograph Series, 32,* 99-110.

Weiss, R.F., & Price, B.A. (1980). Nitrous oxide solubility in water and seawater. *Marine Chemistry, 8,* 347-359.

Wickham, H. (2016). *ggplot2: Elegant graphics for data analysis*. New York, NY: Springer-Verlag.

Wickham, H. (2019). stringr: Simple, Consistent Wrappers for Common String Operations. R package version 1.4.0. https://CRAN.R-project.org/package=stringr

Wickham, H., Averick, M., Bryan, J., Chang, W., D'Agostino McGowan, L., François, R., ... Yutani, H. (2019). Welcome to the tidyverse. *Journal of Open Source Software, 4*(43), 1686.

Wickham, H., & Bryan, J. (2019). readxl: Read Excel Files. R package version 1.3.1. https://CRAN.R-project.org/package=readxl

Yamamoto-Kawai, M., McLaughlin, F. A., Carmack, E. C., Nishino, S., & Shimada, K. (2008). Freshwater budget of the Canada Basin, Arctic Ocean, from salinity, δ18O, and nutrients. *Journal of Geophysical Research, 113*(C01007).

Yurkowski, D.J., Auger-Méthé, M., Mallory, M.L., Wong, S.N.P., Gilchrist, G., Derocher, A.E., … Ferguson, S.H. (2018). Abundance and species diversity hotspots of tracked marine predators across the North American Arctic. *Diversity and Distributions, 25*(3), 328-345.

Zeebe, R.E., & Wolf-Gladrow, D. (2001). *CO_2 in seawater: Equilibrium, kinetics, isotopes.* Amsterdam, Netherlands: Elsevier Science B.V.

Zhang, S. (2011). Late Ordovician conodont biostratigraphy and redefinition of the age of oil shale intervals on Southampton Island. *Canadian Journal of Earth Sciences, 48*(3), 619–643.

Zhang, X., Brown, R., Vincent, L., Skinner, W., Feng, Y., & Mekis, E. (2011). Canadian climate trends, 1950–2007. Ecosystem status and trends 2010, Technical Thematic Report No. 5. Canadian Councils of Resource Ministers. Ottawa, ON. 21 p.